UNIVERSITÀ
DEGLI STUDI
FIRENZE

DOTTORATO DI RICERCA IN
Scienze Biomediche

CICLO XXXV

COORDINATORE Prof. Fabrizio Chiti

Nano-based hyperthermia for melanoma and breast cancer treatment

Settore Scientifico Disciplinare **MED/04**

Dottorando
Dott. Scavone Francesca

Tutore
Prof. Laurenzana Anna

Coordinatore
Prof. Chiti Fabrizio

Anni 2019/2023

C'è una ragione per ogni persona incontrata.

Qualcuno si prende qualcosa, ma qualcun'altra ce la lascia:

Insegnandoci qualcosa di nuovo e tirando fuori il meglio di noi.

Grazie a chi ha incrociato il mio cammino,

ma soprattutto grazie a te

che ci sei sempre stata da quando è iniziato questo percorso

portando allegria nelle nostre vite.

Alla mia dolce nipotina Vittoria

Index

Abstract 6

1. INTRODUCTION 8

Incidence of Cancer 9

Melanoma cancer 11

Breast cancer 15

Radiotherapy 19

Hyperthermia 25

Nanoparticles (NPs) 28

Smart nanoparticles and biodistribution 31

Magnetic Nanoparticles (MNPs) 35

Gold Nanoparticles (AuNPs) 38

NPs for cancer diagnosis and treatment monitoring 42

Nanomedicine combined to cell-based therapy 45

2. AIM OF STUDY 49

Aim of the project 50

3. MATERIALS AND METHODS 52

4. RESULTS 65

Preliminary data 66

Results: Preparation of experimental systems 70

in vitro: Comparative Gold Nanords uptake in tumor cells 70

Isolation and characterization of ECFCs 74

Gold Nanorods uptake in ECFCs 75

Comparison between ECFCs loaded with AUNPs versus melanoma and breast cancer cell line. 77

Localization of ECFC in 3D co-culture by confocal microscopy 78

In vivo: tumor tropic properties of ECFCs in nude rats **80**

Dose-dependent effects of increasing doses of radiotherapy on tumor cell survival **83**

Cytostatic and cytotoxic effect of combined radiotherapy-hyperthermia treatment on MCF7 (breast cancer), M6 (melanoma) and ECFCs: **84**

Gold nanorod mediated hyperthermia effects in M6 monoculture and M6-ECFCs coculture after X-ray treatment **87**

Evaluation of Cellular Damage in coculture exposed to the combo treatment **88**

Gold nanorod mediated hyperthermia effects in MCF7 monoculture and MCF7-ECFCs coculture after X-ray treatment **90**

Evaluation of Cellular Damage in coculture exposed to the combo treatment **91**

Results- second part **93**

Cytotoxicity Investigation and Cellular Uptake in MNPs **93**

Cytotoxicity Investigation and Cellular Uptake of Au@Fe_3O_4 nanostars **98**

5. DISCUSSION **101**

Conclusion and future directions **109**

6. REFERENCES **111**

Abstract

Over the past few decades, hyperthermia therapy (HT) has evolved as one of the most promising cancer-treatment approaches. To overcome drawbacks such as non-selectivity and invasiveness, and to improve therapeutic efficacy, HT has been combined with nanotechnology. Gold nanoparticles (AuNPs) and superparamagnetic iron oxide (Fe_3O_4 MNP) are typically utilized as plasmonic or magnetic hyperthermia agents, since they are able to be rapidly heated upon exposure to bright light source with a precise wavelength or to an alternating current magnetic field (AMF). The raising of the temperature causes apoptosis of tumor cells that are more sensitive to thermal damage than healthy cells. Moreover, is well known that hyperthermia reduces radioresistance and improves the efficacy of anticancer drugs. Herein, we investigate the therapeutic applications of nano-based hyperthermia for melanoma and breast cancer treatment. In particular in the first part of the current work we propose the use of tumor tropic cells, called Endothelial Colony Forming Cells (ECFCs) as cellular carrier of chitosan-coated AuNPs. With this Trojan horse strategy, we evaluated the cooperative effect of radiotherapy and plasmonic photothermal therapy on melanoma and breast cancer cell lines. In the second part of this thesis, we reported two studies in collaboration with CNR of Sesto Fiorentino regarding the antitumoral effects of 1) a multifunctional platform consisting in supermagnetic Fe_3O_4 MNP encapsulated in a dual pH- and temperature responsive poly (N-vinylcaprolactam-co-acrylic acid) copolymer to achieve highly controlled release of doxorubicin for a multimodal cancer treatment combining hyperthermia and chemotherapy and 2) a Au@Fe_3O_4 core@shell system with a highly uniform unprecedented star-like shell morphology combining plasmonic and magnetic properties.

AuNPs uptake was evaluated in melanoma (A375 and A375-M6), breast cancer cell lines (MCF7 and MDA-MB 231) and ECFCs by conventional optical microscope, transmission electronic microscope (TEM), Inductively Coupled Plasma – Atomic Emission Spectrometry (ICP-AES) and Photoacoustic imaging (PA). The PA signal provided from ECFC loaded with AuNPs exhibited a stronger signal enhancement compared to melanoma and breast cancer cells due to the massive amount of gold nanoparticles that ECFCs are able to incorporate. We evaluated the long-term cytostatic/cytoxic effects of combined radiotherapy and nano-mediated hyperthermia on breast cancer and melanoma cell lines using clonogenic assays while the short-term effects were determined evaluating DNA damage by western blot analysis of cleaved PARP and γH2AX and comet assay. Our data show the cooperative effects of the Xray dose (2Gy) with nano-based

hyperthermia with significant reduction of colony number compared to the single treatments. In vivo we proved the tumor homing capacity of AuNP-ECFCs in tumor hypoxic areas. Regarding the Fe_3O_4 MNP loaded with doxorubicin we demonstrated the efficacy of this multi-stimuli-sensitive nanoplatform for the treatment of the melanoma and breast cancer, while the $Au@Fe_3O_4$ magnetic-photermal heterostructure loaded breast cancer cell culture suspension at 658 nm confirmed their optical response and their suitability for photothermal therapy.

Findings from this research will be of translational relevance with potential health system impact related to improved control of metastatic disease in melanoma and breast cancer. The possibility of obtaining molecular imaging of primary tumors and metastases (diagnosis) and of inhibiting tumor growth and development of metastases (therapy) through different therapeutic strategies will pave the way for new and promising approaches to combat tumor progression.

1. INTRODUCTION

Incidence of Cancer

Cancer is a leading cause of death in every country and a major impediment to extending life expectancy [1]. In 112 of 183 nations, cancer is the first or second major cause of death before the age of 70, and it ranks third or fourth in another 23 countries, according to estimates from the World Health Organization (WHO) in 2019 [2].

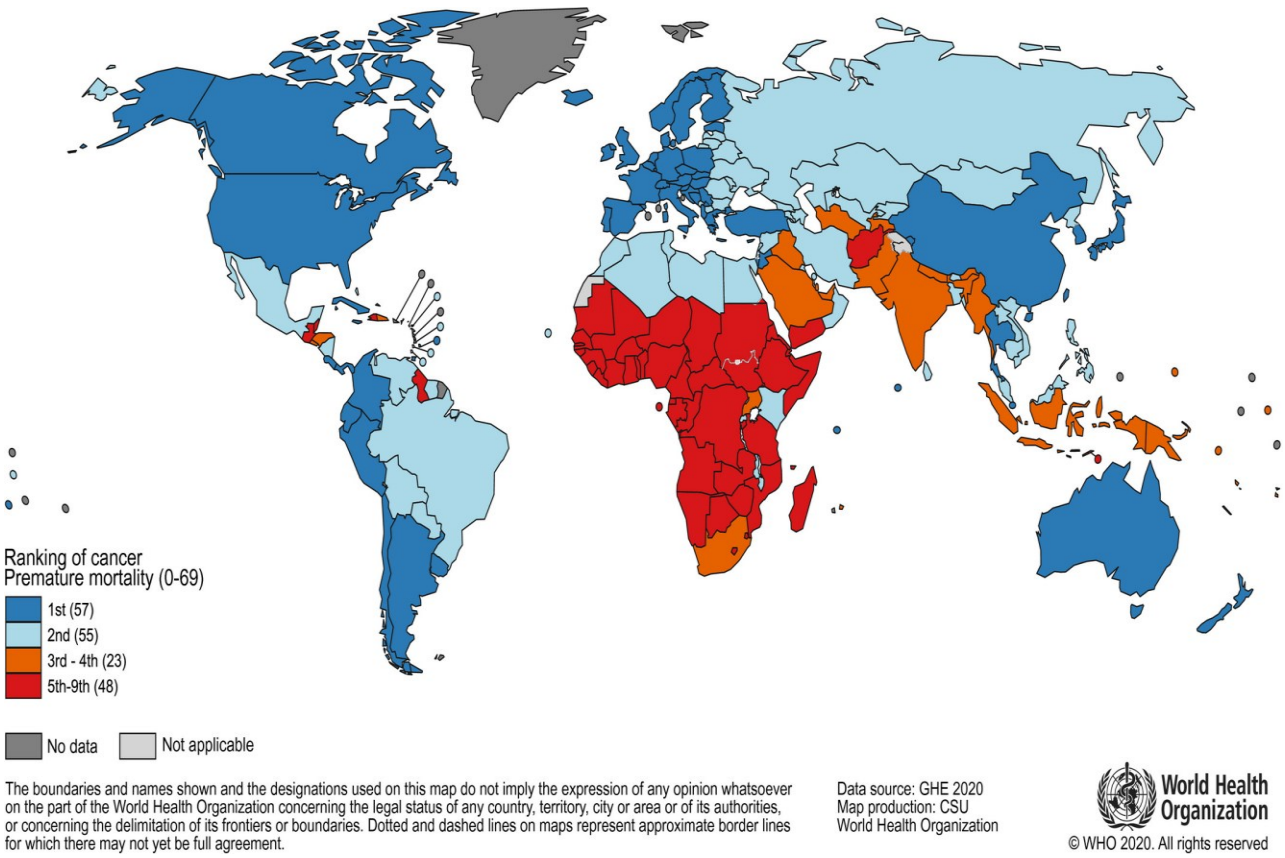

Figure 1: National Ranking of Cancer as a Cause of Death at Ages <70 Years in 2019. The numbers of countries represented in each ranking group are included in the legend. *Source: World Health Organization* [2].

Currently, 1 in 8 men and 1 in 10 women will develop cancer within their lifetimes. In 2022, among males the 3 most prevalent cancers are prostate (3,523,230), **melanoma of the skin** (760,640), and colon and rectum (726,450) while among females are **breast** (4,055,770), uterine corpus (891,560), and thyroid (823,800) (fig.2). The distribution of prevalent cancers differs from that of incident cancers because prevalent cancers reflect survival and median age at diagnosis as well as cancer occurrence [3].

Male		Female	
Prostate	3,523,230	Breast	4,055,770
Melanoma of the skin	760,640	Uterine corpus	891,560
Colon & rectum	726,450	Thyroid	823,800
Urinary bladder	597,880	Melanoma of the skin	713,790
Non-Hodgkin lymphoma	451,370	Colon & rectum	710,670
Kidney & renal pelvis	376,280	Non-Hodgkin lymphoma	394,180
Oral cavity & pharynx	311,200	Lung & bronchus	367,570
Testis	303,040	Uterine cervix	300,240
Leukemia	300,250	Ovary	246,940
Lung & bronchus	287,050	Kidney & renal pelvis	230,960
All sites	**8,321,200**	**All sites**	**9,738,900**

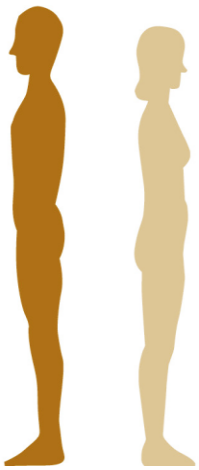

Figure 2: Estimated number of West Countries Cancer treatment and survivorship statistics, 2022. Comparison between men and women. As can be seen from the numbers presented, higher incidence in males is prostate cancer, followed by skin melanoma and colon and rectal cancer. In women, genital tumors (breast and uterine body) have a higher incidence, but melanoma of the skin is present with relatively high and comparable numbers between the two sexes [3].

Despite enormous efforts and improvements in cancer research, chemotherapy, surgery, and radiation remain the conventional treatment choices [3].

Melanoma cancer

More than 90% of melanoma cases are of the cutaneous melanoma (CM), which is by far the most prevalent subtype. Compared to other cancers, melanoma incidence is rising more significantly. The incidence rate for melanoma is around 25 new cases per 100.000 people in Europe, 30 per 100.000 in the US, and 60 cases per 100.000 in Australia, where it is quite high. The frequency of the disease has dramatically increased in recent years across all age categories, average age of diagnosis is 57 years. In lower age groups, women are more likely to be diagnosed, whereas in older age groups, males are more likely to be diagnosed. According to US estimates, women have a 1 in 56 lifetime chance of developing melanoma and males have a 1 in 37 lifetime risk. In general, men have a greater death rate than women, presumably due to the disease's later manifestation [4].

Melanoma originates from melanocytes that reside in the basal layer of the epidermis where they produce melanin, which offers protection from UV. The activity and survival of melanocytes are strictly dependent on cells such as keratinocytes and fibroblasts, but also depend on external factors such as UV radiation.

According to Clark's model, melanoma is a process which starts from a benign nevus in which melanocytes carry on a controlled proliferation; accumulation of mutations in the melanocytes results in the formation of a dysplastic nevus, then melanoma which can remain latent or propagate. The growth of melanoma can be radial, which remains confined to the epidermis or vertical, associated with dermal invasion and which can culminate in formation of metastases by malignant cells (fig.3) [5].

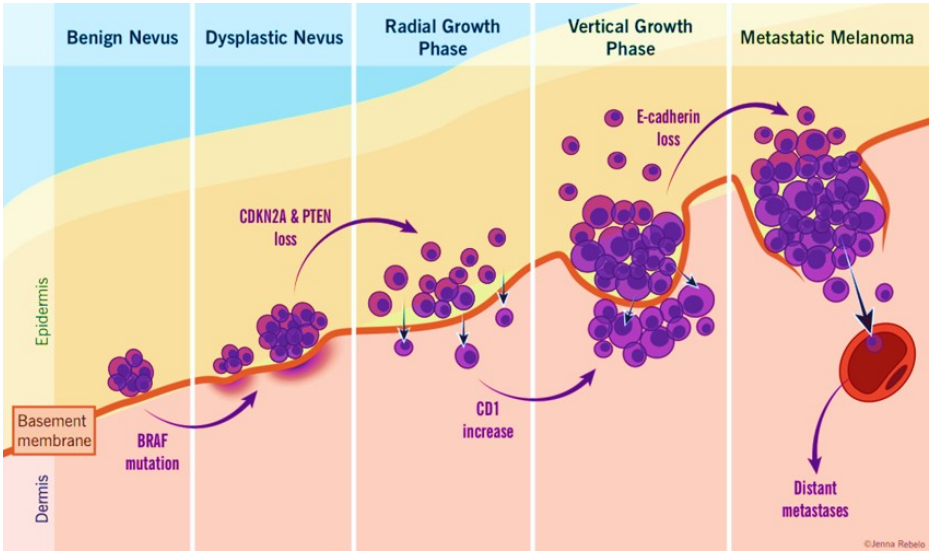

Figure 3: Melanoma formation: from mutation of BRAF in benign nevus to progression to metastasic melanoma [6].

Epidemiologic investigations have revealed several risk variables considered to be important in the development of cutaneous melanoma. These can be split into environmental and hereditary influences, although there is certainly a relationship between the two [4]. The first risk factor for the development of melanoma is given by sun exposure. The molecular profile of cancer, or the site of UV-induced mutations, varies significantly depending on the subtype of melanoma, the prognosis, and the response to therapy.

However, a high number of nevi can represent a risk factor, in fact about 25% of melanomas are formed from pre-existent benign nevi[7]

The genetic alterations in melanoma may be viewed as specific arrangements of molecular lesions that block a specific set of pathways, each of which is essential to the growth of melanoma. The MEK pathway can be activated by a mutation in either NRAS or BRAF, and an NRAS mutation can activate both the MEK and PTEN pathways. 20-30% melanoma patients have mutations in NRAS proto-oncogene while 50-70% of melanomas present BRAF mutations.

BRAF is a serine/threonine kinase that plays a critical role in the MAP-Kinase signalling pathway, responsible of cell proliferation and differentiation. The prevalent mutation on BRAF (90% of all mutations) is most commonly resulting in substitution of valine for glutamic acid at position 600 (V600E).

In cases of familial melanoma, the major gene known to be associated with the development of melanoma, identified from linkage analysis of multiple-case families, is CDKN2A, the inhibitor of cyclin dependent kinase 4, more rarely CDK4.

Several medicines have been authorised by the US Food and Drug Administration (FDA) in recent years. Surgical excision, chemotherapy, radiation, photodynamic therapy (PDT), immunotherapy, or targeted therapy may be used depending on the characteristics of the tumour (location, stage, and genetic profile). Even though most patients have localised disease at the time of diagnosis and are treated with surgical removal of the original tumour, many people develop metastases [8]. While radiation of symptomatic metastases may provide therapeutic benefit to patients, melanoma is thought to be a moderately radioresistant tumour.

Usually, radiation therapy is a form of treatment used in conjunction with systemic therapy [9].

Chemotherapy used essentially comprises two drugs which are Dacarbazine (DTIC) and Temozolomide (TMZ). DTIC was approved by the FDA for the treatment of melanoma in 1975 and, despite its modest efficacy, dacarbazine was the standard of care because other single agents or combination chemotherapies did not reveal improvements in the survival of patients. Temozolomide is an analogue of Dacarbazine and has not shown therapeutic advantages over this one; the choice between TMZ and DTIC, therefore, essentially falls on the type of administration, given that TMZ can be taken orally and DTIC cannot, and compared to dacarbazine, TMZ showed a reduced improvement in median progression-free survival, but no differences were observed in overall survival or objective response rates [10].

In 19th century, immunotherapy was proposed knowing the interaction between the tumour and the immune system. Most commonly used immuno-stimulators or monoclonal antibody for treatment of melanoma are *interleukin (IL)-2*, which acts by stimulating T-cell proliferation and function [11]; *interferon (IFN)-alpha* and *ipilimumab*, which block CTLA-4 transmembrane receptors belong to immunoglobulin superfamily and are overexpressed by T-lymphocytes and thymosin alpha 1 [12].

In addition to chemotherapy and immunotherapy, ***targeted therapy*** has been introduced to treat metastatic melanoma that selectively acts on molecular targets associated with tumour development and progression. BRAF inhibitors act on BRAF which is the most frequently mutated oncogene in melanoma and induces constitutive activation of RAS–RAF–MEK–ERK-signalling cascade; the most frequently used among BRAF inhibitors are Sorafenib, Vemurafenib, and

Dabrafenib. Sorafenib acts on various tyrosine kinase receptors such as BRAF, CRAF, PDGFR, VEGFR, p38 and c-kit; it was the first RAF inhibitor actively studied in melanoma patients, but it has not produced encouraging outcomes, either as a single agent or in combinations. Vemurafenib is an orally active BRAF inhibitor that is 30 times more specific for mutant BRAF than wildtype BRAF [13]. Vemurafenib demonstrated anti-proliferative action in melanoma cell lines with the BRAF-V600E mutation, and it was the first BRAF inhibitor to conclude phase I testing with considerable therapeutic benefit. During clinical trials, it demonstrated even better effectiveness than Dacarbazine [14] and the FDA authorised it for the treatment of melanoma in 2011. Despite the benefits of treatment, individuals treated with Vemurafenib quickly develop drug resistance, which is the main restriction of this kind of therapy. The development of resistance to BRAF inhibitors in most all cases, as well as toxicity associated with BRAF inhibition, are major limitations in their use [15]. There is good evidence that BRAF mutations are related with greater selectivity and sensitivity to MEK inhibitors, which is also a gene in the same signalling cascade such as Trametinib [13].

Nowadays, since the limited efficacy by therapy provided (such as dacarbazine and other chemotherapeutic drugs) when used alone, combination therapy is now the most often employed technique for treating melanoma, and in particular combination of target therapy and nanoparticles; moreover, recently findings reported the improved efficacy of target therapy and different kinds of nanoparticles and nanovesicles [12].

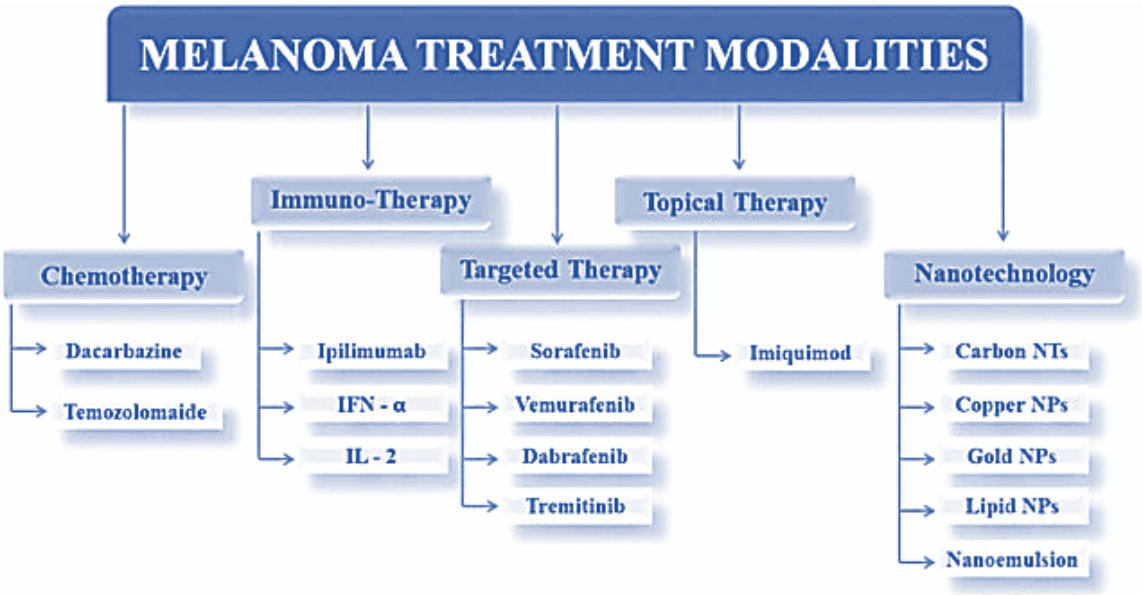

Figure 4: Schematic indicating the different therapies and specific treatments in metastatic melanoma [12]

Breast cancer

It is eximated that about 2,3 million new cases of breast cancer, representing for 11.7% of all cancer cases. It is the sixth highest cause of cancer mortality globally, accounting for 685.000 deaths. [2]

However, in the last years the reduction in mortality from breast cancer has been associated with earlier diagnosis through screening and superior adjuvant therapy [16]. Despite lower incidence and mortality, breast cancer remains the most common cause of cancer mortality in women, representing for 15% of all cancer deaths in women in the western countries [3], [16].

Breast cancer develops from an in-situ carcinoma characterised by epithelial cell proliferation with a complete myoepithelial cell layer and basement membrane, which progresses to invasion into adjacent tissues (invasive ductal carcinoma) and metastasis after myoepithelial cell layer disruption and basement membrane degradation. Breast cancer is considered metastatic when the myoepithelial cell layer and basement membrane are lost, angiogenesis occurs, and tumorigenic-epithelial cells invade to distant areas [17].

Breast cancer progression can be divided into five phases or stages (fig. 5) by considering tumor location, tumor size, lymph node involvement, and metastatic progression. Together with the status of crucial molecular markers, these stages currently define patient stratification.

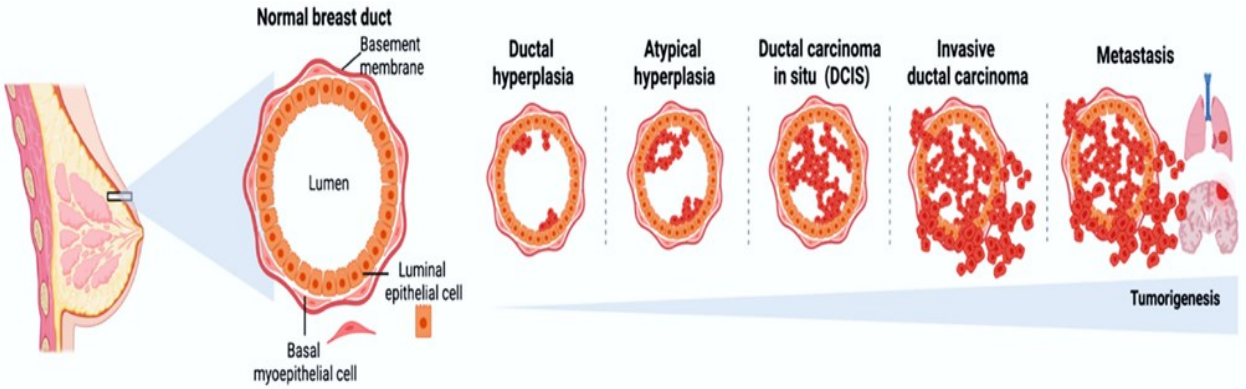

Figure 5: Breast cancer formation: from a normal tissue to progression to metastasis [18].

The specific mechanisms by which brest cancer (BC) develops are unknown. A significant percentage of BC diagnoses may be due to pregnancy-assiaciated factors, hormonal therapy, lifestyle variables (such as obesity, inactivity, alcohol use and smoking); more than a third of breast cancer cases in high-income nation appear to be curable with a change in lifestyle [19],

[20]. Nevertheless breast cancer in the family is well acknowledged as a significant risk factor for the disease. Affected first-degree (mother, doughter or sister) influence approximately 13% to 19% of women diagnised with breast cancer, compared to slightly fewer (8%-12%) of women without cancer. Breast cancer risk rises with the number of afflicted first-degree relatived compared to women without a first-degree family history, rising 1.5 to 4 fold with the number of diagnosed relatives [21], [22].

BC is associated with two types of genetic alterations: a) *germline mutations* (a mix of egg and sperm cell mutations) notably BRCA1 and BRCA2, which are connected to around 40% of hereditary malignancies [23] as well as b) *somatic mutations* that develop as a result of misalignment of DNA rearrangement in gene repair. BC germline genetic connection and locus originates from two specific genetic mutations, **BRCA1** (chromosome 17q21.31) and **BRCA2** (chromosome 13q13.1) which was discovered in 1994. BRCA1 AND BRCA2 genetic testing changed the capacity to learn about predicted risk for breast cancer, as well as the clinical approach to care for individuals with a known genetic mutation to provide more personal preventative screening and treatment options [23].

Based on the molecular and histological evidence BC can be classified into three types: BC expressing hormone receptor such as estrogen receptor (ER+) or progesterone receptor (PR+), BC expressing human epidermal receptor 2 (HER2+) and triple negative brest cancer (TNBC) ER, PR, HER2, divided into six categories: basa-like 1 (BCL-1), basal-like 2 (BCL-2), immunomodulatory (IM), mesenchymal (M), mesenchymal stem cell-like (MSL), and luminal androgen receptor (LAR) [24] (table 1). The BC expressing ER is the most prevalent type of BC, it consists of 60-70% of BC cases, in developed countries in particular in pre-menopaausal women. The treatment strategies should be based on the molecular characteristics of BC [25].

Subtype	Receptor profile	Subcategories
Hormone positive	ER+ OR PR+	Luminal A and B
HER 2 positive	HER2 +	
Triple negative breast cancer	ER-, PR-, HER2-	BCL-1, BCL-2, IM, M, MSL and LAR

Table 1

Breast cancer subtypes category

Mammography is a prevalent screening method for detecting breast cancer and has been shown to drastically reduced mortality by at least 20%. Over the past ten years, additional screening methods, which are more sensitive than mammography, have also been used and researched: for example MRI screening which is highly more sensitive in detecting cancer and showed a sensitivity of 90-93%, compared with 48-63% for mammography and ultrasound combinated [19], [26]. Some nations have limited the use of MRI screening to breast cancer patients with a very high risk to develop the disease (such as mutations). New screening methods including contrast-enhanced spectral mammography and offer a feasible alternative to traditional MRI [19], [27].

The typical method of treating BC is surgery. There are two types of surgery: conservative surgery, which involves the removal of a tumour that does not affect all of the breast, usually referred to as a partial or lumpectomy. In the "non conservative" surgery is typically a complete mastectomy, which involves more invasive surgery with the complete removal of the breast which is applied in 30% of all BC operations. The aim of these years has been to discover alternative medicines that result in surgical removal as a final and drastic strategy in order to prevent this dramatic solution. [28].

Hormone treatment and immunological treatments are examples of targeted treatments in addition to antiangiogenic therapy. Hormonotherapy is the most commonly used therapeutic approach [29]. Hormone therapy blocks estrogen receptor (ER) or reduces estrogen by inhibiting the enzyme aromatase. Aromatase transforms the adrenal testosterone to endogenous estrogen in post-menopausal women. This conversion is the only source of endogenous estrogen in women. In the case of BC patients expressing HER 2 , there are several anti HER2 monoclonal antibodies; the standart therapy for this kind of patients is a combination therapy of anti-HER2 and chemiotherapy [30]. Example of drugs are: Tamoxifen is an ER-blocking drug used as the first round of hormone treatment in postmenopausal women with metastatic tumors. Trastuzumab is a monoclonal antibody, specifically it binds to the extracellular domain of the HER-2 (human epidermal growth factor receptor 2) and prevents the development of cancers that overexpress HER-2 [31], [32].

Unfortunately, many traditional therapies have limitations that reduce their efficacy, such as limited solubility, ineffective tumour targeting, and side effects in healthy tissues and the development of drug resistance. Many of these difficulties can be solved by advanced drug delivery technologies such as nanomedicines, which can enhance breast cancer treatment.

Importantly, nanomedicine formulations of classic chemotherapeutics, such as doxorubicin (Doxil) and paclitaxel (Abraxane), are now common first-line therapies for breast cancer [33], giving impetus for this therapy strategy [17].

Liposomes, protein nanoparticles, polymeric nanoparticles, and immunoconjugates are examples of FDA-approved chemotherapy drugs nanomedicines for breast cancer therapy. All have a clinically demonstrated ability to reduce toxicity and improve efficacy when compared to the parental drug (the "free" form of the drug) due to improvements in solubility, tumour targeting, which result in beneficial pharmacokinetic and whole-body biodistribution changes [17], [34].

Radiotherapy

Since Nobel Prize winner Marie Curie discovered radioactivity, radiotherapy (RT) has been regarded as a crucial and effective method of destroying or controlling tumours [35].

Although certain apparently benign conditions, such thyroid eye disease, and arteriovenous malformations of the central nervous system (CNS), can also be treated with radiation, radiotherapy is a potent weapon in the battle against cancer. Ionizing radiation is used to treat almost all forms of solid tumours with different degrees of efficacy. Radiotherapy represents a very cost-effective single modality treatment that accounts for just approximately 5% of the overall cost of cancer care [36]. Currently, approximately half of all cancer patients now receive radiation, surgery, and/or chemotherapy [37], [38]. Numerous cancer patients get radiation, which may be used alone or in conjunction with other cancer treatments, with the aim of treat or reducing their symptoms. Radiation is a physical agent used to kill cancer cells. Ionizing radiation is applied because it produces ions (electrically charged particles) and deposits energy in the cells of the tissues it passes through. RT is often used to treat cancer cells by employing high-energy photon radiation such as X-rays, gamma (γ)-rays, and others. Radiation can be applied to the cancerous area in two different methods. The delivery of external beam radiation involves directing high-energy rays (photons, protons, or particle radiation) at the tumour's site from outside the body. The most typical method used in a clinical environment is this one. Internal radiation, also known as brachytherapy, is administered directly to the tumour location using seeds or radioactive sources sealed inside catheters from within the body. Based on its short-term effects, this is mostly employed in the usual treatment of gynaecological and prostate cancers as well as in circumstances where retreatment is necessary [36].

This deposited energy has the potential to damage cancer cells or generate genetic alterations that result in cancer cell death. High-energy radiation destroys cells' genetic material (deoxyribonucleic acid, DNA), inhibiting them from dividing and proliferating further.

Radiotherapy can eliminate cancer cells and tumour tissue through both direct and indirect methods (figure 6) [37]: by direct impact, radiation causes single-strand breaks (SSB) and double-strand breaks (DSB) in DNA therefore stops cell division and proliferation and can even cause cell necrosis and death. In the case of indirect action, radiation causes the production of ROS, which can damage biomolecules, cause cellular stress, and drastically alter signalling pathways inside cells. Clinical investigations have revealed that to precisely deliver radiation doses to a malignant

tumour or regions within the tumour, more than half (about 70%) of patients require the use of RT-controlled linear accelerators.

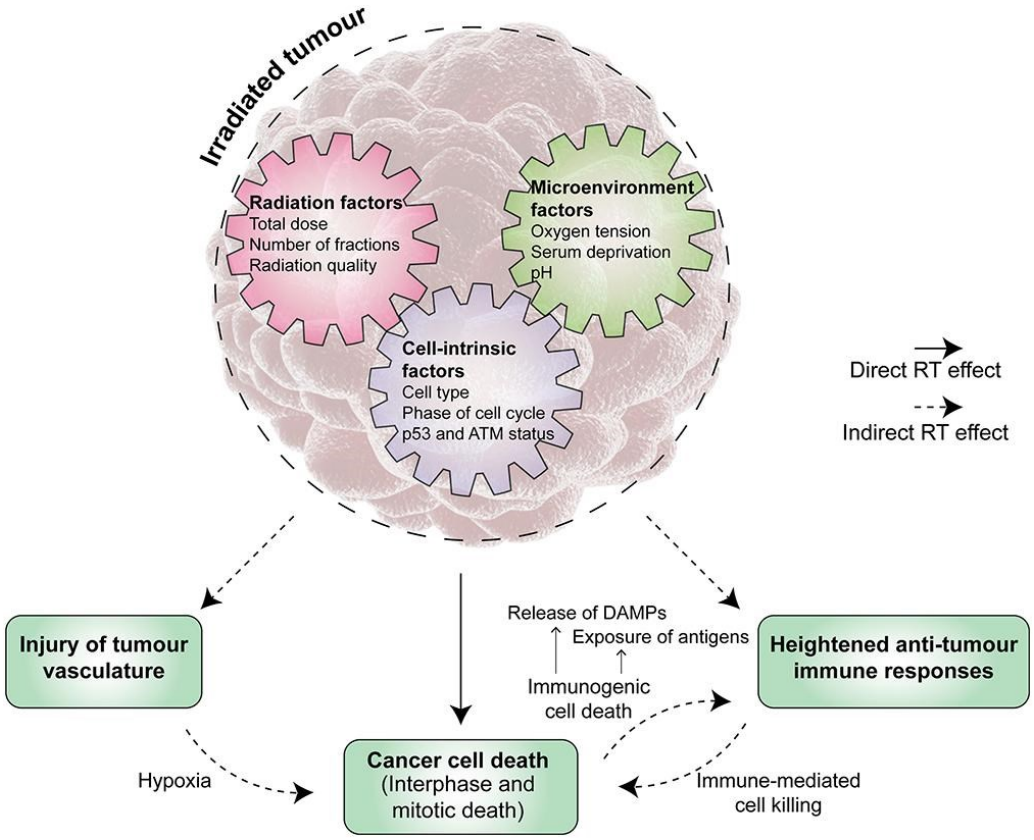

Figure 6: To suppress the tumour, tumour radiation causes both direct and indirect effects. Direct impacts can happen at various times after the first irradiation event as a result of severe radiation-induced DNA damage in cancer cells that results in their death. Indirect effects of radiation treatment (RT), including as damage to tumour vasculature and activation of innate immune responses against tumours, can also have an anti-tumor impact. Numerous variables, which may be generally categorised as cell-intrinsic, radiation, and microenvironment variables, affect both the onset and severity of these effects [39].

The different radiobiological properties of diverse normal tissues and cancer provide the foundation for radiation treatment administered in a fractionated regime. Compared to cancer cells, which multiply quickly, normal cells multiply relatively more slowly, giving them more time to repair damage before replicating. Current regimes are based on the more refined linear-quadratic formula which addresses the time-dose factors for individual tumor types and normal tissues. Today, radiation treatment typically entails daily fractions of 1.5 to 3Gy given over a period of several weeks [36].

That such, specific cancers respond extremely well to modest doses of radiation (e.g., lymphomas, seminomas), whereas other are exceedingly radioresistant and likely to develop even after large doses of radiation (e.g., melanoma, glioblastoma) [40], [41].

Radiosensitizer

There are still several difficulties in the RT, such as cancer stem cells, tumor heterogeneity, angiogenesis and vasculogenesis, metabolic alterations, and complications, making it difficult to use. One approach of overcoming these challenges is to improve the efficacy of RT by adding radiosensitizers, which are molecules/materials that can increase tumor cell radiosensitivity.

G.E. Adams, a pioneer in this field, classified radiosensitizers into five categories: suppression of intracellular thiols or other endogenous radioprotective substances, formation of cytotoxic substances by radiolysis of the radiosensitizer, inhibitors of biomolecule repair, thymine analogues that can incorporate into DNA, and oxygen mimics with electrophilic activity [42], [43]. This categorization was based on the mechanics of DNA damage and repair and indicated the direction for radiosensitizer sat the early stage.

However, as technology advances, an increasing number of materials and drugs with radiation sensitization are being classified as radiosensitizers.

According to the most recent study, radiosensitizers are divided into three types depending on their structures: small molecules (such as oxygen); macromolecules (protein and peptides), and nanomaterials [43]:

One of the main radiation difficulties is hypoxia in the tumour microenvironment. Compared to the normal oxygen microenvironment, tumour cells are substantially more radiation resistant in the hypoxic microenvironment. The term "oxygen enhancement effect" describes how the presence of oxygen enhances either the positive or negative effects of ionizing radiation. When cells receive an ionizing radiation dosage, the so-called oxygen effect becomes most apparent [44]. Irradiation induces energy transfer resulting in water radiolysis, with the creation of an ion radical that subsequently reacts with another water molecule to generate the extremely reactive hydroxyl radical. After reacting with the hydroxyl radical, oxygen produces peroxide [37]. The peroxide then causes cellular and DNA damage that is irreversible. While diverse cells adapt to the hypoxic environment effectively by activating various signalling pathways, particularly the *hypoxia inducible factor* (HIF). According to studies, HIF-1 is connected to the VEGF signalling

pathway, the glucose transport system, and the glycolysis pathway, all of which may contribute to the formation of the tumour's vasculature. The cancer cells become more aggressive and substantially more resistant to radiation when there is hypoxia [37], [45]. More and more studies have revealed in recent years that active components from Chinese herbs, including curcumin, resveratrol, and others, can improve the effectiveness of tumour radiation. Turmeric contains curcumin, a polyphenolic active ingredient. The transcription factor NF-kB, which is implicated in both cancer and radioresistance genes, is inhibited by curcumin to provide anti-inflammatory effects [46]. Resveratrol is an active substance that may be obtained from several plants, including mulberries, grapes, knotweed, and peanuts. Resveratrol increased radiosensitivity in human NSCLC NCI-H838 cells, according to Liao et al., through decreasing NF-kB activity [47].

Additionally, capable of controlling radiosensitivity, macromolecules like proteins, peptides, and oligonucleotides have been researched to create radiosensitizers. The development of methods for manipulating macromolecules, such as bioinformatics and molecular cloning, can aid in resolving the problems impact the immunogenicity and stability of macromolecules. As a result, macromolecules offered a potential opportunity for the development of radiosensitizers.

Nowadays, the advancement of nanotechnology offers motivation and expands the vision for the development of radiosensitizers. Heavy metal nanomaterials with high atomic number (Z) values have showed promise as radiosensitizers in recent years due to their ability to absorb, scatter, and emit radiation energy. High Z nanomaterials with acceptable size and components were simple to manufacture. Noble metal nanomaterials, including gold (Au, Z=79), silver (Ag, Z=47), and platinum (Pt, Z=78), can effectively absorbing X-ray energy and interacting with radiation in tumour cells. These materials subsequently release photoelectrons and other secondary electrons. In addition to their direct interactions with DNA, these secondary electrons also react with water to produce more reactive oxygen species (ROS), which raises the tumour cells' s radiation sensitivity [37].

Gold nanoparticles (AuNPs) are one of the many nanomaterials being researched for radiotherapeutic uses, and they have long been considered of as a possible tool for the detection and treatment of a variety of tumours. AuNPs settles at tumour sites as a result they lend themselves well as a contrast agent for imaging and can be used in disease diagnosis and biological imaging [48]. Nevertheless, AuNPs are being researched as potential tumour radiosensitizers due to the following advantages: when compared to conventional agents, they

are inert molecules with good biocompatibility and little biological toxicity with a high photoelectric absorption coefficient; in addition, the radiosensitizing effect of AuNP is given by the cooperation of physical, chemical, and biological effects (fig 7).

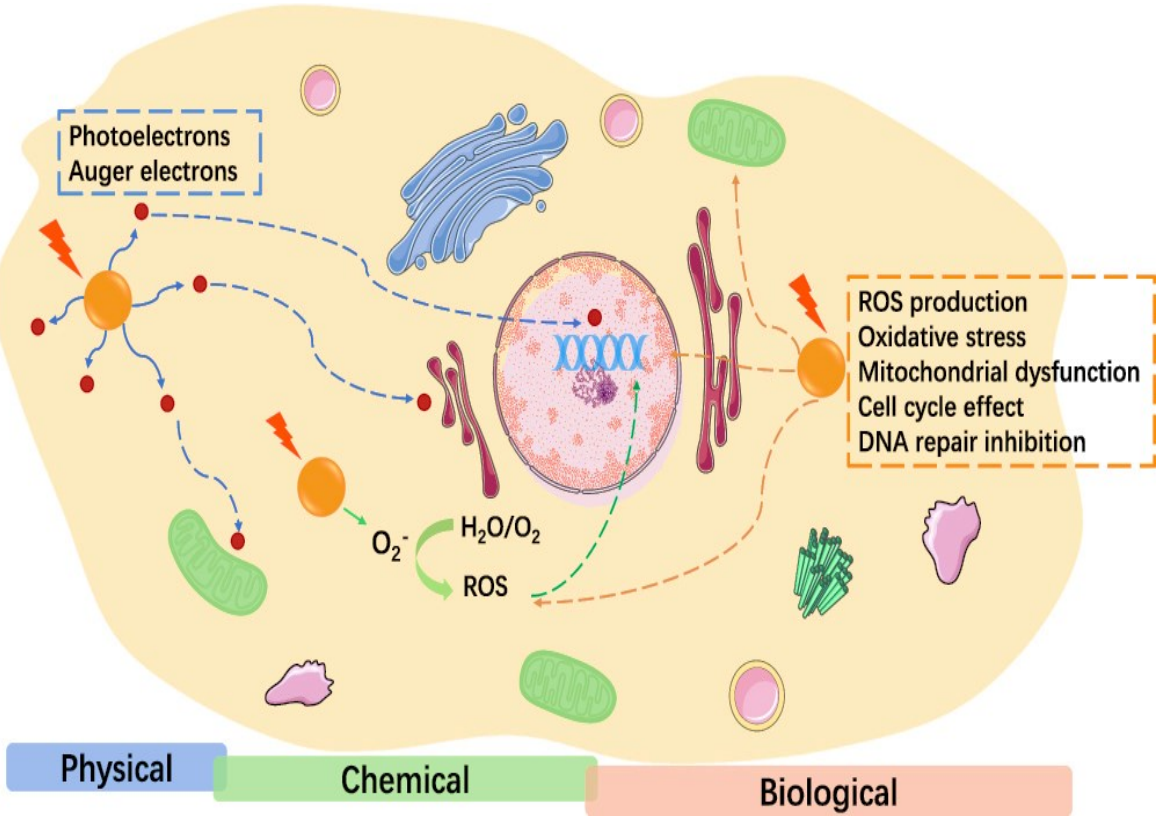

Figure 7: Sensitization was also associated to future physical, chemical, and biological alterations. These three components work in tandem to influence the interaction of AuNPs with radiation physical dose enhancement, including the photoelectric effect. Chemical contributions based on the chemical sensitivity of DNA to radiation-induced damage, as well as enhanced radical production and catalysis; ROS generation, oxidative stress, mitochondrial dysfunction, cell-cycle effect, DNA repair inhibition, and other biological mechanisms might be classified as biological phases such as autophagy [48].

The differential in mass-energy absorption coefficients between AuNPs and soft tissues is the fundamental premise underlying their use as radiosensitizers therefore, AuNPs can deliver more

unit mass energy and enhance the local radiation dosage deposited in the target volume (tumour tissues) by taking advantage of the difference in atomic number between Au (Z=79) and soft tissue (which is predominantly composed of low atomic number organic components), which causes radiosensitization [49]. Radical reactions and/or the activation of "open" chromatin structures are the main "chemical processes" of AUNP radiosensitization which increases DNA's susceptibility to radiation-induced damage. AuNPs promote and fix radiation-induced cell damage by stimulating radical reactions and increasing ROS production. Furthermore, the increased intracellular ROS levels may further impact biological processes through oxidative stress [48], [49].

Due to their considerable photothermal conversion efficiency and X-ray deposits, nanomaterials have gained substantial interest in photermal treatment (PTT), photodynamic treatment (PDT), and radiation therapy. The benefit of RT is a deeper depth penetration that is feasible, whereas PTT gives superior sensitivity and a healing effect. As a result, their collective efforts can produce deep tissue therapy [50].

Hyperthermia

The goal of hyperthermia (HT) in oncology is to raise tissue temperature and either kill or slow the proliferation of cancer cells by increasing the temperature of the tissue [51].

The temperature at a treated location is maintained during HT therapy for at least an hour, ranging from 40 to 48 °C. Temperatures >50 °C can be referred to as coagulation, 60-90 °C as thermal ablation, and above 200 °C are considered to cause charring [52] (Fig.8). High-temperature or ablation HT is described as using chemical or thermal therapy directly to a tumour to achieve tumour annihilation or considerable tumour destruction. Still, the important biological consequence of the two modalities is that mild hyperthermia causes apoptosis whereas thermal ablation causes necrosis [53].

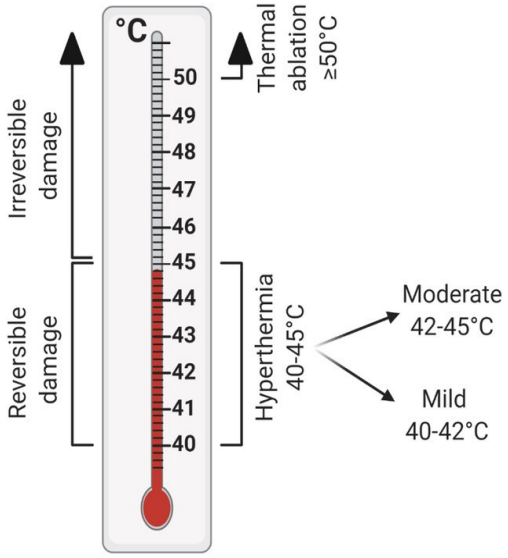

Figure 8: The temperature range used in cancer thermal therapy: temperatures of 40-45 °C are commonly used in hyperthermia therapy, which can be further subdivided into mild (40-42 °C) and moderate (42-45 °C) hyperthermia to account for their various effects. Mild hyperthermia has been shown to increase blood perfusion as the tumour attempts to thermoregulate the elevated temperatures. The irregular tumour vasculature struggles to deal with these thermal doses at moderate temperatures and vascular stasis is caused [54].

As can be seen from quote given below, the potential of hyperthermia in medicine was already known at the time of Hippocrates:

"What the medicine does not cure, the scalpel heals,

what the scalpel does not heal, the fire heals it,

what fire does not heal must be considered incurable"

Hippocrates (460–377 B.C)

While HT has been used to treat malignancies since the time of the ancient Greeks, its application has been criticised due to restrictions, for example, the difficulty in obtaining uniform heat distribution throughout the tumour, and the inherent difficulties in targeting undetectable micro metastases. Recent advancements in nanoparticle-assisted thermal treatment have the potential to solve many of these issues.

There are different clinical ways of high-temperature applications, which are determined by the organ to be targeted, the stage of malignancy, and the energy distribution technology used, such as: local HT where heat is delivered to tumours through microwaves, radio waves, or ultrasound. It is devoted in small tumours no more than 5 cm size. During regional hyperthermia procedure, a portion of the patient's blood is removed, heated, and then pumped back into the limb or organ, usually in conjunction with anticancer treatments. Finally, whole body HT; immersion in a hot water bath and radiant heat with UV radiation are the most common methods. Heat the body to 42.0 °C for 60 minutes or 39.5-41.0 °C for three to four hours [52], [55].

In vitro and in vivo studies have revealed that hyperthermia in the 40-45°C range has a variety of consequences, including [56]:

- Direct death of tumour cells and modifications in the microenvironment
- Activation of heat shock proteins and the apoptotic cascade
- Immune response activation
- Modifications to cell cycle regulatory signalling pathways
- Modifications to the distribution of blood flow, oxygen, and nutrients in the tumour location.

If the temperature does not exceed 45°, hyperthermia is almost always associated with other ways of treating cancer (radiotherapy, immunotherapy, surgery) is commonly well tolerated and seldom affects normal tissues [57].

Hyperthermia can change the microenvironment and make cells more susceptible to radiotherapy or chemotherapy (fig. 9a). In addition, hyperthermia interferes with the homologous recombination, preventing the radiation induced DNA strand breaks repair, and inducing cell cycle arrest and apoptosis (fig.9b) [58].

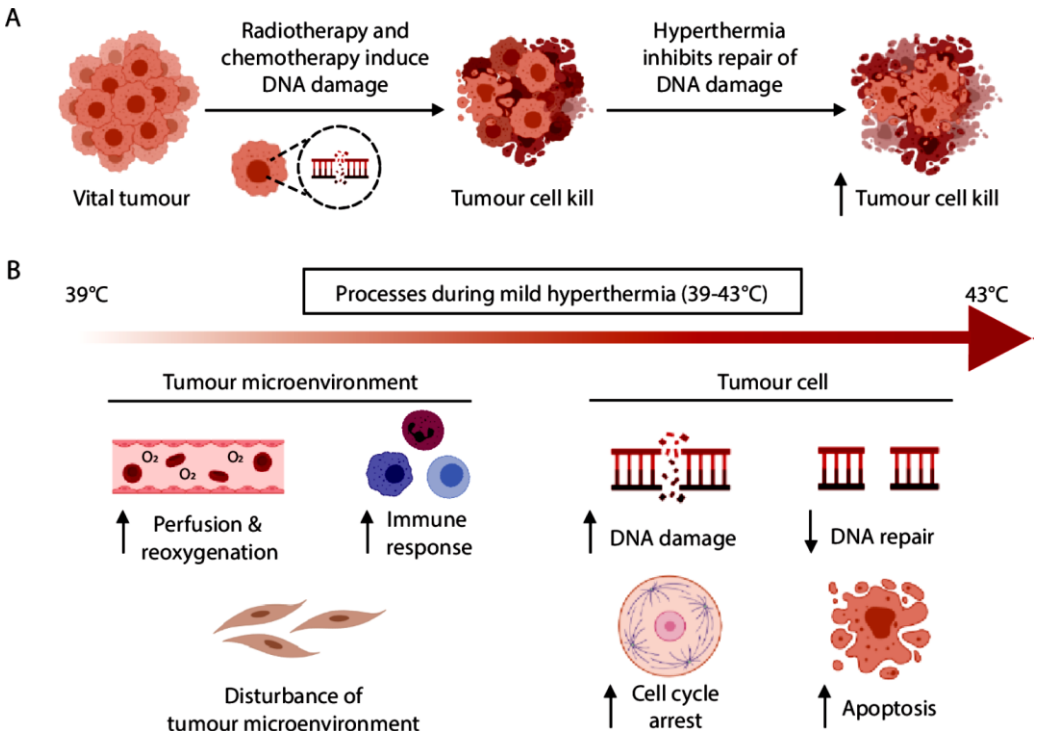

Figure 9: A) The use of hyperthermia in combination with other treatments such as radiotherapy or chemotherapy causes irreversible damage to the DNA. Already starting from an increase in temperature to 39°C, there are changes at the level of the tumour microenvironment that cause alterations in the oxygenation and perfusion of the blood and an activation of the immune response; B) but it is with the increasing of temperatures, above 41°C, hyperthermia can temporarily impair DNA repair processes, generating an increase of DNA breaks and, as a result, cell cycle arrest. Failure to repair DNA breaks results in cell death, such as apoptosis [59].

Nanoparticles (NPs)

One of the most promising 21st-century technologies is nanotechnology. Richard P. Feynman proposed the term **"nanotechnology"** in his famous lecture, in 1959: "There's Plenty of Room at the Bottom". Nanoscience is the study of structures and molecules on ranging from 1 nm to even 500 nm. By seeing, measuring, manipulating, assembling, regulating, and creating matter on a nanoscale, it is possible to translate the theory of nanoscience into practical applications [60], [61] . The combination of nanotechnology with cancer chemotherapy has recently drawn a lot of interest and research thanks to a greater knowledge of nanomaterials and the use of nanotechnology. This has opened an interesting new possibility for cancer-targeted therapy [62]. An overview of the many nanomaterials that are often employed is shown in figure 10, the size is determined in relation to biomolecules or organism, which are comparable to nanomaterials [63]. NPs are nano-scaled objects and are composed of organic and inorganic compounds to be used as such or as carrier platforms for therapeutic molecules. Organic nanocarriers include phospholipid micelles, vesicles, multilamellar liposomes, dendrimers, and carbon nanotubes, while inorganic ones include quantum dots (composed by atoms of group II and group VI of the periodic table), gold NPs, silica (mesoporous) NPs, and superparamagnetic iron-oxide-NPs (SPIONs) [64]

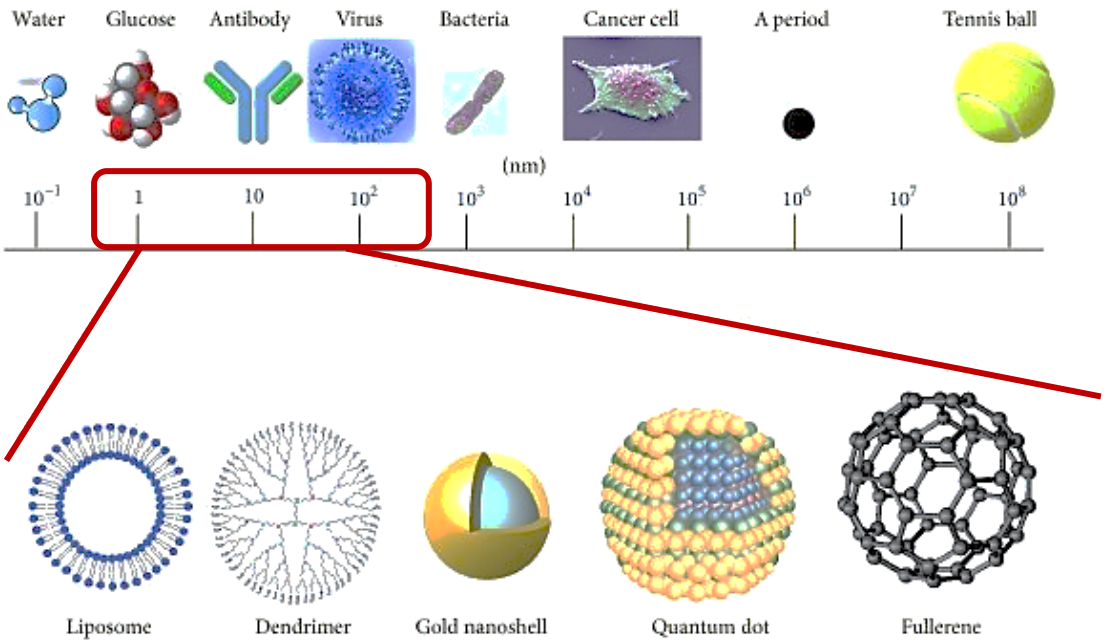

Figure 10: Representation of nanometer (nm) scale. Several nanomaterials ranging in size from 1 to 100 nm. [63].

Two methods for describing the many options to produce NPs have been proposed: ***top-down*** and ***bottom-up***. These two processes differ in terms of quality, speed, and cost.

Using a top-down method, bulk material is essentially broken down to create nanoparticles. This may be accomplished by using advanced techniques developed and improved by industry in recent decades, such as precision engineering and lithography [60].

The term “bottom-up” describes the process of creating nanostructures atom by atom or molecule by molecule combining physical and chemical techniques at nanoscales while precisely manipulating atom and molecule self-assembly. Chemical synthesis is a way of creating rough materials that may be employed directly in products in their bulk disordered form or as building blocks for more sophisticated ordered materials. In a bottom-up process called self-assembly, atoms or molecules arrange themselves into structured nanostructures through chemical-physical interactions. Positional assembly is the only technique in which single atoms, molecules or cluster can be positioned freely one-by-one [60].

The use in nanomedicine of the nanoparticles is based on their chemical and physical properties, such as for example as nanocarrier for delivering systems for anticancer drugs.

Furthermore, knowing nanoparticle *shape* has considerably contributed to the creation of nanocarriers. Studies have demonstrated that particle shape and size play a significant role in cell interaction, circulating time, targeting effect, ability to cross biological barriers, and other properties. This is because these characteristics are likely to affect the particles in blood transport, particularly in small vessels and tumor vessels, as well as how cells recognize and respond [62]. It has been proved that sphere-shaped particles travel efficiently because to their inherent symmetry, but non-spherical particles tumble with the flow. The spleen and liver are two filtering organs where this will be more evident. Worm-like micelles accumulated much more than spherical particles in the liver, spleen, and kidneys. It has been demonstrated that the particle's shape, geometry, and orientation have a major impact on cellular uptake [65] [66].

For the selection of nanocarriers, *size* is among the most crucial factors. The cellular absorption of nanoparticles can be affected by their size, and because they frequently group together in solutions, their size may also increase. The cellular absorption of bigger particles is much higher than that of smaller particles in the same concentration [67] moreover, some nanoparticles can overcome the size limit for renal clearance, in fact, it is widely known that the kidneys prevent molecules larger than 6–8 nm from escaping into the urine[68], therefore, the renal clearance increases with particle size, as demonstrated by research on inorganic nanoparticles by Yu et al.

[69] the method of cellular absorption can also be influenced by particle size. For example, according to studies, clathrin-mediated cell uptake is the primary method by which spherical particles with a size of ≤200 nm enter cell [62], [70].

Surface charges have a strong correlation with the biological behaviours of nanoparticles, including solubility, biodistribution, stability, cellular uptake, cytotoxicity, and others, as shown by studies[71], [72]. Only positively charged nanoparticles may be taken up by cells when they are disseminated in the culture media, as demonstrated by Tang et al.[73] However, if the particles are coupled to a protein, the electrostatic difference between positively and negatively charged particles can be nearly entirely removed. Because the cell membrane is negatively charged and occasionally has a small amount of positive charge on the patch, the adsorption between particles and cell membrane and membrane transport occurs by the surface charge,[62], [73] which makes positively charged particles more easily absorbable than negatively charged or neutral particles.

Many types of NPs

Because of the outer lipid bilayer, ***lipid-based nanoparticles*** have an easy cellular absorption of medicines. Liposomes and solid lipid nanoparticles are two of the most significant lipid-based nanomaterials. Liposomes are made up of a lipid bilayer that surrounds an aqueous core, whereas lipid NP is made up of a lipid monolayer that surrounds a solid lipid core. Liposomes and solid-lipid nanoparticles are particularly useful in inhalation treatment for chronic lung illnesses since they are stable during aerosolization [12].

Dendrimers are synthetic molecules with a repeated branching pattern. Dendrimers, despite their advantages as drug and gene delivery vehicles, can be cytotoxic and hemolytic, presenting substantial toxicity and safety issues. Because dendrimers are nondegradable in the physiological environment, the accumulation of nondegradable artificial macromolecules inside cells or tissues has serious consequences. Nevertheless, a variety of pharmaceuticals or therapeutic chemicals can be contained in dendrimers by simple electrostatic interaction or covalent attachment. Dendrimers have the potential to be employed in cancer therapy through nanotechnology [64] [74]

Inorganic nanoparticles generated from macromolecule such as *iron oxide, gold*, have emerged as extremely important building components. They are suitable in diagnostic in surface plasmon resonance (SPR), magnetic resonance imaging (MRI) or positron emission tomography (PET).

Also, their ability to scatter and convert the light or magnetic stimulus into heat a which they are subjected to, it's the reason they can be used in hyperthermia of solid tumours.

Smart nanoparticles and biodistribution

Nanocarriers are nanoparticles that are employed as transport modules for other substances. Conventional nanocarriers lack the capacity to transport and release drugs at the appropriate concentration at the targeted site in response to external or internal stimulus.

The FDA has approved several of these advanced class NP-based platforms, commonly known to as ***"smart nanoparticles",*** for use in the treatment of different cancers, including metastatic uveal malignant melanoma (Marqibo) and photosensitizing agents (biodegradable NPs with a controlled drug release) to specific tumours [75], [76].

Precisely, smart nanocarriers must have specific characteristics such as aggregate only at the target destination, release the load at the targeted site at predetermined concentrations, and avoid the immune system's filtration process. In addition to treatments, they can also deliver additional resources including genetic material, imaging agents, etc [77].

The nanocarriers must also overcome biological barriers that limit the accessibility of the drug or nanoparticles to the tumor. To achieve a precise distribution in the target tissue, it is vital to understand all the biological barriers that a particle meets after intravenous injection and to intervene in the design of the nanocarrier based on them. Extracellular barriers, capillary hemodynamic and marginalisation, endothelial permeability, and intratumor spread are examples of physiological barriers (fig.11) [78]. Nanocarriers may also encounter difficulties such as cleansing by the reticuloendothelial system (RES), on their way to the desired place. After the RES rapidly eliminates the anti-cancer drug-carrying nanocarriers from circulation, they are accumulated in the liver, spleen, or bone marrow. For avoiding this cleaning process NPs are also functionalized on the surface with polymers biocompatible, such as PEG (poly-ethylene-glycol) layer, which serves to minimize the aggregation of NPs and to increase their residence time in the circle blood. Unfortunately, PEGylation significantly decreases the cells' ability to absorb NPs [79].

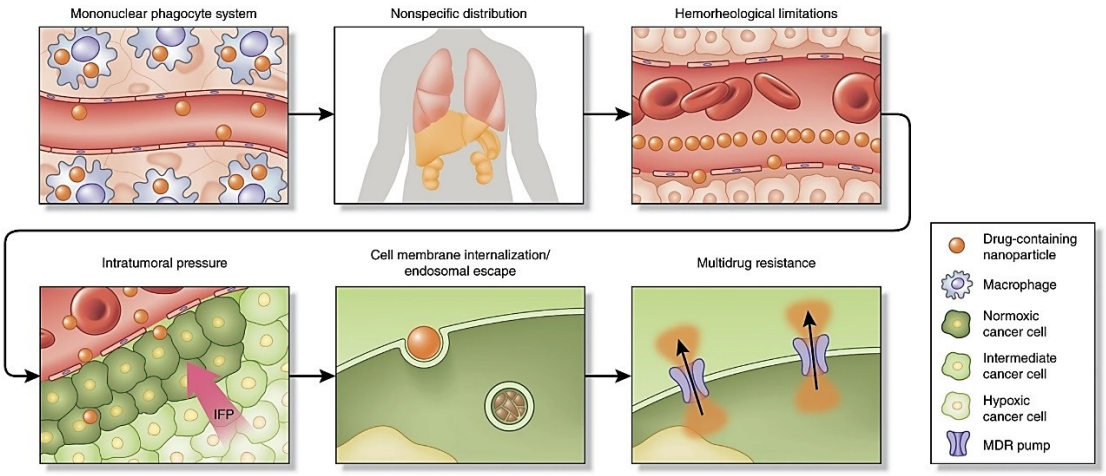

Figure 11: Framework of sequential biological barriers to NPs drug delivery.

Nanoparticles undergo opsonization by macrophages, this results in high accumulation of nanoparticles in organs, such as the spleen and the liver. Another barrier to NPs accumulation in tumors is the high intratumoral pressure, resulting from interrupted vasculature. Cellular internalization and endosomal escape prove to be formidable barriers (e.g., clathrin versus caveolin) and intracellular fate. At least, upon entry into the cell, drug efflux pumps that confer therapy resistance expel chemotherapeutics from the cell. IFP, interstitial fluid pressure [80].

The difficulty in recent years in research has been to identify an effective technique to target tumours using theranostic nanoparticles, in particular, two strategies have received a lot of attention [81], [82]: ***passive*** and ***active targeting***.

Passive targeting is based on the diffusion of the nanoparticles in the tumor tissue by using the enhanced permeability retention (EPR) effect (fig. 12.a); the *active targeting* makes use of biological ligands linked to the nanoparticles to recognize overexpressed biomarkers on tumor cells (fig.12.b). This last strategy is based on the combined effects of passive EPR and active identification of cancer molecular markers.

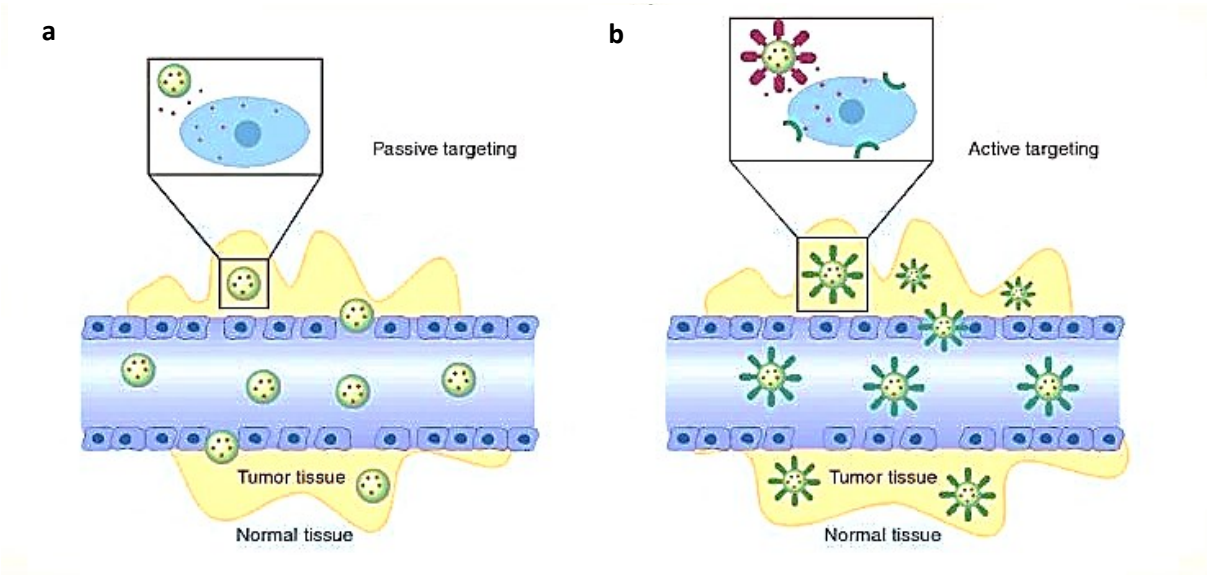

Figure 12: a) NPs can passively extravasate through leaky vascularization due to the improved EPR effect, in this situation, drugs can be released in the extracellular matrix and then permeate the tissue, b) a ligand that binds to endothelial cell surface receptors can be included into NPs. In this instance, the improved permeability and retention effect is irrelevant, and leaky vasculature is not necessary [83].

Passive targeting

For NPs to accumulate in tumour tissues, passive targeting takes use of the distinct pathophysiological features of tumor vessels. Normally, lymphatic drainage is impaired in tumor vessels because they are extremely disordered, dilated, and have a lot of pores. This leads to increased gap junctions between endothelial cells. Despite being the foundation of clinical medicine, passive targeting techniques have several limitations. It is not always possible to target tumour cells indiscriminately because certain drugs do not diffuse well and because the method is unpredictable and difficult to control. The increased permeability and retention is an effect that can be exploited for passive targeting by therapeutic and diagnostic molecules. Nanoparticles that have a smaller diameter than the pores of tumor vessels can permeate tumor tissue and remain within it for an extended period of time [84]. For the effective release of macromolecules through the EPR effect, it is necessary to study the mechanism and the factors that accelerate or slow down this phenomenon [85].

Due to abnormal vasculature and EPR effect, nanoparticles show higher accumulation in tumor tissue compared to other tissue. Furthermore, the nanoparticle system improves the half-life of the drug due to its non-clearance by the kidneys [86]. Factors such as binding to blood proteins and nanoparticle aggregation can also influence the EPR effect. The biodistribution studies

allowed to optimize the synthesis and coating of the nanoparticles to improve the specific uptake in the tumor tissue. Various factors can influence the recruitment of nanoparticles to the tumor site. The shape of the nanocarriers can affect the fluid dynamics and thus influence the absorption as described above. The surface charge of these nanoparticles can also influence their stability and distribution in the blood: it has been shown that positively charged particles are captured by the tumor vessels, while a neutral surface charge allows, after extravasation, a faster diffusion towards the tumor tissue [87]. Even the surface of nanoparticles can be modified with ligands that can prolong their stay in the bloodstream and promote different types of endocytosis and cellular uptake in tumor tissue [83] [86].

Active targeting

One method of getting over passive targeting's drawbacks is to use a variety of conjugation chemistries to attach affinity ligands—antibodies, peptides, aptamers, or small molecules [88] on the surface of the nanocarriers. The conjugation of these ligands can avoid the non-specific uptake of nanocarriers by some tissues and favour that of the tumor tissue.

In the last decade, advances in nanomaterial synthesis methods have allowed the development of nanoparticles capable of responding to specific internal and external stimuli for the release of the drug conveyed in order to reduce non-selective exposure to chemotherapy.

Changes in pH, redox, ionic strength and stress in target tissues are examples of internal stimuli. Differences in the pH of blood and intracellular organelles may allow nanocarriers to specifically release drugs when they reach tumor tissue. Tumors typically have a hypoxic microenvironment with low levels of oxygen and nutrients and therefore high levels of reducing agents, such as glutathione. Nanocarriers with disulfide bonds can be used to target these tissue types that carry out the redox reaction that oxidizes glutathione, leading to increased cell apoptosis [89]. External (physical) stimuli include temperature, light, ultrasound, magnetic force, and electric fields. Hyperthermia, a temperature change with a range of 37 to 42°C, can increase blood vessel permeability and enhance nanocarrier release. The use of near-infrared wavelengths can increase penetration into the body, compared to UV light, which is superficially absorbed by skin, blood, and tissue less than 10 cm deep. Magnetic and electric fields can allow nanoparticles to aggregate at specific sites [89], [90].

Magnetic Nanoparticles (MNPs)

In 1960, Freeman et al. first proposed the idea of using magnetic materials and magnetic fields in medicine [91]. Magnetic nanoparticles (MNPs) offer numerous advantages [92] including heat generation ability, lack of toxicity, high chemical stability, and good biocompatibility. All these properties confer to MNPs the potential to provide highly effective multimodal action for cancer diagnosis and treatment such as magnetic resonance imaging (MRI), cell tracking, drug delivery, and magnetic fluid hyperthermia (MFH) [93] (fig.12).

Most MNPs employed in biological applications are formed of: **Iron oxide nanoparticles** (IONPs) such a maghemite (Fe_2O_4) or magnetite (Fe_3O_4) and **gadolinium** (chelated organic indium), due to their ability to break down into iron and oxygen in the body, they are utilized in metabolic processes and oxygen transport and are simple to remove from the body. When nanoparticles with sizes of approximately 10 nm in diameter are fabricated, IONPs show superparamagnetic behavior (superparamagnetic iron oxide nanoparticles, SPIONs), accountable to better dispersibility without a magnetic field. They accumulate at the target site in presence of a magnetic field, which is many important for theranostic uses [94]. MNPs are now being used in a variety of medical applications, including ***hyperthermia*** cancer treatment [95], controlled drug release [96], ***magnetic resonance imaging*** (MRI) [97], and biosensing [98] (fig. 13). The ability of MNPs to be magnetically controlled by an outside magnetic field is a significant benefit. The most crucial factors in defining the biological uses of MNPs are their chemical composition, size, shape, morphology, and magnetic behaviour [98].

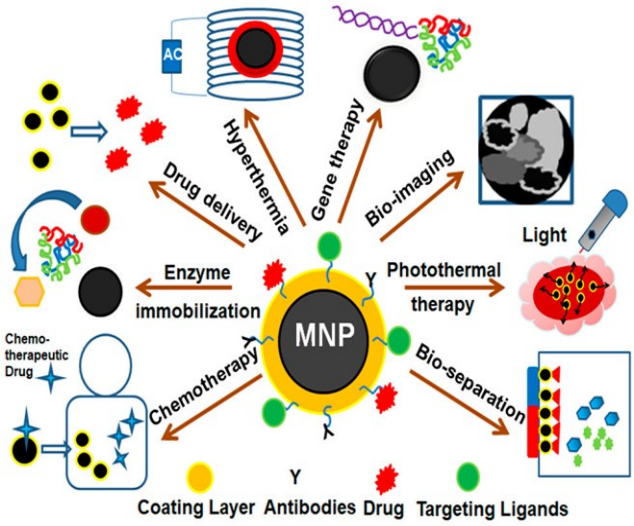

Figure 13: Representative image of the various mechanisms by which MPs act in the diagnosis and therapy of the tumour [93].

Magnetic hyperthermia

Functionalized MNPs can convert alternating magnetic field (AMF) energy into thermal energy, resulting in **local** heating of tumour cells (41-47°C) (Fig. 14)[99] and thus, apoptosis of cancer cells.

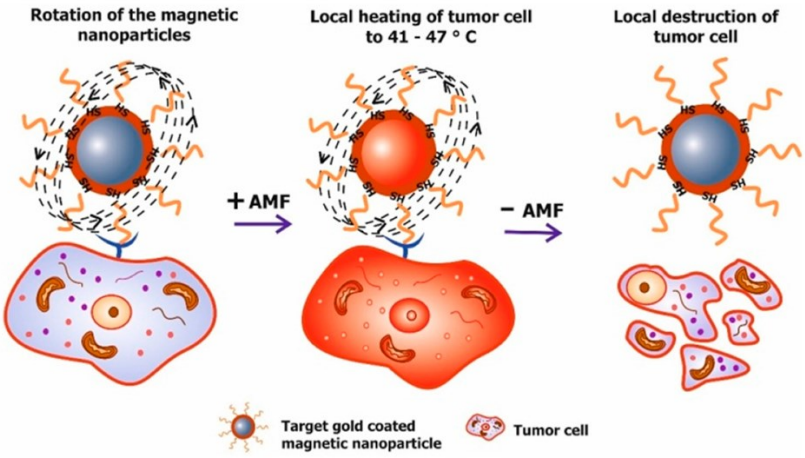

Figure 14: Hyperthermia mediated by magnetic fields: its basic theory. An alternating magnetic field is used to expose tumour cells to targeted magnetic nanoparticles (AMF). AMF energy is then transformed into heat by the magnetic nanoparticles, which causes the local heating of the tumour cells to occur between 41 and 47 °C. [99]

To increase the therapeutic effectiveness of chemotherapeutic drugs at tumour locations, magnetic field hyperthermia (MFH) has also been investigated as an adjuvant treatment in the drug delivery system [100].

Despite the advantages that combination magnetic hyperthermia and drug delivery offer, developing effective drug delivery carriers using MNPs is still difficult due to the absence of a suitable controlled release method and the risk for conjugated drug leakage during circulation. To address these difficulties, smart organic-inorganic nanohybrids have been proposed to develop multistimuli-responsive platforms that can deliver and release the drug at the proper time and concentration by activation through external or internal stimuli such as temperature and pH[101]. The application of thermo-responsive drug nanocarriers is one of the numerous strategies suggested in the literature, that consist of an MNP core and a temperature-responsive polymer shell to facilitate the efficient controlled release of the drug controlled by MFH [102].

Polymers that respond to temperature and are water soluble, such poly (N-vinylcaprolactam) (PVCL), have been studied in oncology to offer remotely controlled drug release [102]. Although of the higher biocompatibility and lower cytotoxicity of thermo-responsive PVCL compared to other smart polymers used in biological applications, it has not been commonly used to modify

the surfaces of MNPs. This is because the controlled radical polymerization of PVLC monomers is intrinsically complicated [103], [104]. For spatial and temporal control over the release of the drugs, induced by MFH, it is crucial to apply temperature-responsive polymers with the LCST in the hyperthermia temperature range (41-45°C) [105]. To do this, LCST of PVCL might be improved by the addition of hydrophilic components like polyacrylic acid (PAA). Based on the notable pH difference between healthy and malignant tissues, pH-sensitive polymers, such as polyacrylic acid (PAA), can also be used for stimuli responsive drug delivery applications [106]. The pH in the tumour extracellular matrix, which is frequently more acidic than pH in normal tissues and blood, might cause the release of the drug load [107].

Gold Nanoparticles (AuNPs)

Gold has been utilised in medicine since the fifth century to treat a variety of diseases, but it is only in recent decades that the research of AuNPs has generated particular interest in biomedical application [108]. The latter are often associated with standardized methods of synthesis, allowing to produce gold nanoparticles (AuNPs) with specific shapes and sizes (fig.15).

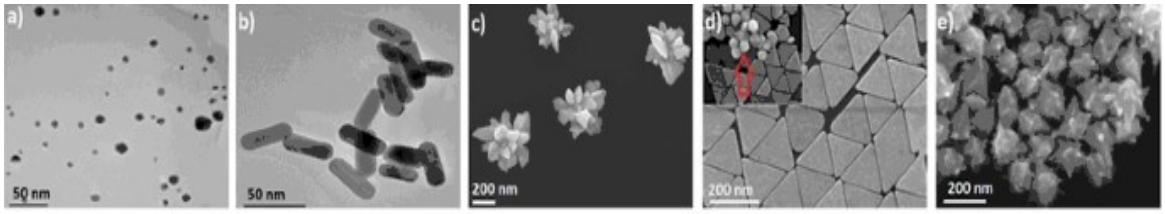

Figure 15: a) spherical; b) nanorods, c) nanoflowers, d) nanoprism and e) nanostars[109].

AuNPs have a variety of biological uses, but tumour detection and therapy take main stage. The natural characteristics of AuNPs should be thoroughly and deeply researched in order to improve their applicability for tumour detection and therapy.

Two components, physical and chemical, were used to examine the fundamental characteristics of AuNPs. These two enhance the use of AUNPs in clinical chemistry, targeting, nano enzyme, phototherapy, radiation, imaging agents and drugs transport (figure 16).

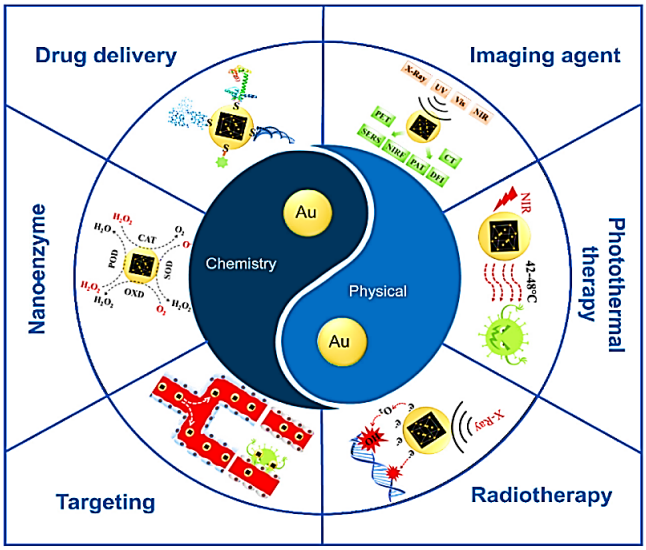

Figure 16: Applications for tumor diagnosis and treatment based on the basic physical and chemical properties of gold nanoparticles (AuNPs) [110].

Surface plasmon resonance (SPR) is a key physical characteristic of AuNPs. In the treatment and diagnosis of tumor, localized surface plasmon resonance (LSPR), radioactivity, and high X-ray absorption coefficient are frequently used [110]. This occurrence happens when the frequency of free electron oscillation at a nanoparticle's surface resonates with the frequency of incoming light radiation producing a plasmon band. As a result, an electromagnetic field manifests at the AUNP surface, providing surface-enhanced optical properties [108]. The proportions of the absorption and scattering effects produced by AuNPs depend on their size and shape as well as other factors such as the type of solvent, surface ligand, core charge, temperature, and the presence of additional nanoparticles adjacent, that all influence the electron charge density on the particle surface [108]. The surface plasmon is strongly affected by the shape of nanoparticle since the restoring force of the accumulated electrons depends mainly on the particle geometry. Figure 16 shows the results of an investigation into the nanorods absorption characteristics using UV-Visible spectroscopy. These nanorods demonstrate independent electron vibration along the diameter and long axis directions (fig.17) the electrons accumulated along the rod axis generate different plasmons: the peak in the visible to near-infrared range is caused by the longitudinal localised surface plasmon resonance (longitudinal plasmon) while the peak in the diameter axis direction is due to the transverse surface plasmon resonance (transversal plasmons) [111]. Respectively, for the nanorods, these two characteristic peaks have been identified at 525 nm and 760 nm wavelengths.

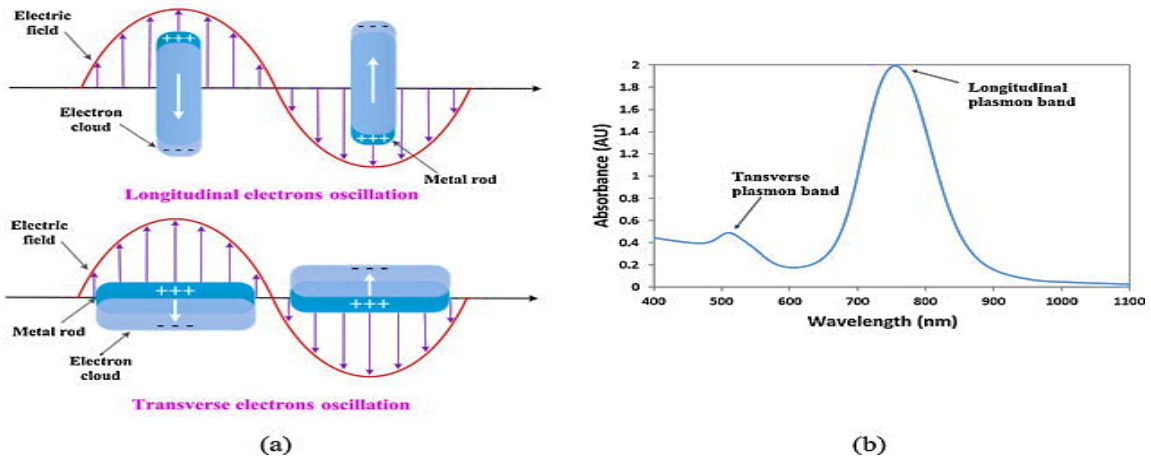

Figure 17: a) Schematic illustration of LSPR excitation for nanorods and b) LSPR absorption bands of nanorods: longitudinal and transverse plasmon bands corresponding to the electron oscillation along the long axis [112]

Gold nanoparticles are thus excellent tool for bioimaging and theranostic applications due to their unique optical characteristics that span the broad visible to near-infrared (NIR) spectrum.

Thanks to the LPSR, AuNPs can efficiently absorb energy of NIR and transfer it to a photosensitizer or O_2, which resolves some drawbacks of common organic photosensitizer, such as poor photo-stabilities, being easily degraded by enzymes and a low efficiency of light energy of conversion [110], [113].

The conjugated organic photosensitizer may be stimulated to produce O_2 by the AuNPs, which act as a photosensitive enhancer, by transferring absorbed light energy to it [114]. Using AuNPs as a photosensitizer, one may directly convert absorbed light energy into O_2 to destroy cancer cells Vankayala and colleagues in 2011 [115] were the first to indicate that this sensitization could be carried out under NIR (915 nm) light excitation and may have substantial PDT effects on the eradication of solid tumours in mice. Currently, people are actively investigating to improve the role of AuNPs in photodynamic therapy (PDT).

Due to its ability to penetrate deeper into tissue and lessen photodamage to cells, near-infrared (NIR) light in the "therapeutic window" is more suitable for these purposes than UV light (Figure 18a). In figure 17b is shown the optical window: the wavelength ranges of 650–950 nm consists in the first window while the second window has a range between 1000–1350 nm.

Numerous reasonably designed NIR-I fluorescent probes have recently been developed to accurately identify and examine significant biomolecules and molecular events in real time. These probes have also been used to support surgical imaging treatments like the removal of tumour tissue and photothermal therapy [116].

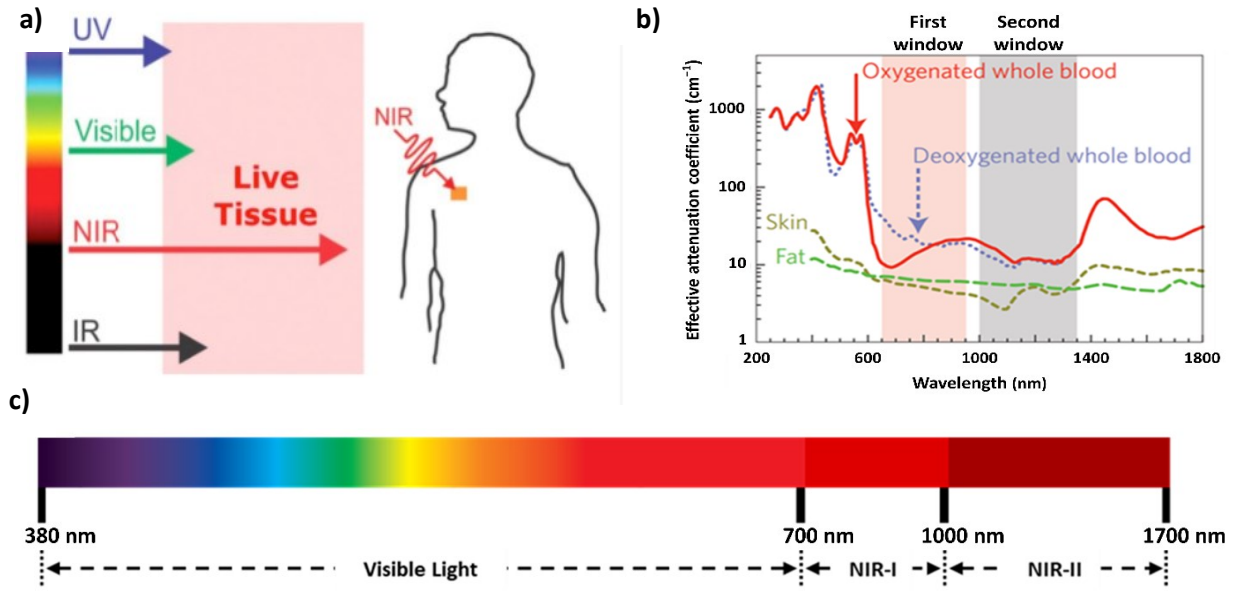

Figure 18: a) Various wavelengths of light's depth of tissue penetration. Compared to UV and visible light, NIR light penetrates tissue more deeply. Near-infrared (NIR) light penetrates tissue and causes photoreactions at the surfaces of nano-carriers in the body[117]; b) there are focused the two optical windows in various biological tissues and fluids. c) Spectral ranges for visible light, NIR-I and NIR-II showing the corresponding wavelengths [116].

To reduce absorption by the biological medium, photothermal cancer treatment employing gold nanostructures depends on a surface plasmon resonance red-shifted (650–900 nm). By modifying the size, shape, and morphology, surface plasmon resonance bands' location and intensity may be easily controlled. Therefore, altering the shape of gold nanostructures is a potent instrument to alter the position of the peak absorption wavelength for the formation of photo-induced heat. [118]. Several studies have reported on efficient photothermal therapy using NIR responsive gold nanostructures such as nanorods [119], [120].

Plasmonic photothermal therapy is an approach quite promising for the treatment of cancer. By using photothermal agents, such as AuNPs, which have the ability to turn light into heat, the localised heat is produced. Depending on the intensity of the heat and the duration of exposure, this results in irreversible cell damage. Reactive oxygen species are produced during hyperthermia consequentially, proteins and nucleic acid are progressively destroyed as a result of this oxidative stress. Long-term (>60 min) exposures to these temperatures are necessary for direct cell necrosis. On the other hand, even for short exposure durations (4–6 min), temperatures exceeding 48°C directly produce permanent protein coagulation and DNA damage

that culminate in cell death [121] Photothermal therapy has the benefits of spatiotemporal controllability, minimal invasiveness, and tumour type independence [122].

NPs for cancer diagnosis and treatment monitoring

Biological events, anomalies, and the progression of diseases are often examined, detected, and tracked using medical imaging. Current imaging techniques are constantly being developed to increase the resolution of medical images. These methods include magnetic resonance imaging (MRI), photoacoustic imaging (PAI), optical fluorescence imaging, ultrasonic (US), computed tomography (CT), single-photon emission computed tomography (SPECT), and positron emission tomography (PET)[98].

Magnetic resonance imaging

Using magnetic resonance imaging (MRI), biomedical imaging contrasts a signal created by a tissue's reaction to the external magnetic field, which is controlled by the proton density of a proton and magnetic relaxation time. The use of exogenous contrast chemicals, which increase the resolution of the method and allows a better interpretation of the acquired images, can further increase the diagnostic utility of MRI. By reducing the longitudinal (T1) and transverse (T2) relaxation times of nearby water protons, these agents improve image contrast. T1 contrast agents are made of paramagnetic metal ions, which have a persistent magnetic moment as a result of unpaired electrons that encourage the energy transfer from nuclear spins to environment, lowering T1 relaxation. The so-called T2 contrast agents' preferred T2/T2* shortening mechanism is derived from local magnetic field distortions and bulk susceptibility effects [97], [123], [124] fig. 19.

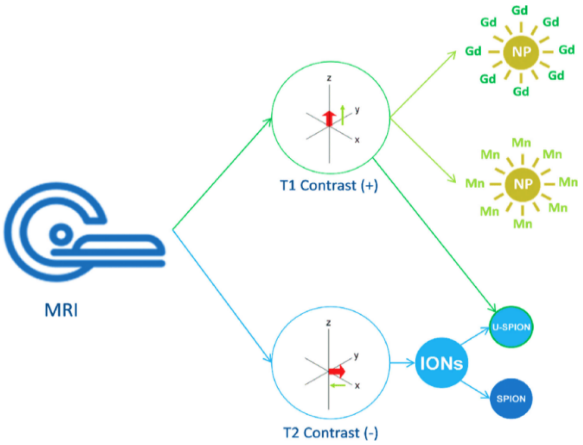

Figure 19: MRI uses type T1 and T2 contrast. As an imaging agent for positive contrast, Gd (III) is often preferred. By attaching functionalized contrast agents to nanoparticles, prolonged positive contrast imaging is possible. T2 contrast agents are iron oxide particles, while T1/T2 dual contrast agents are ultrasmall nanoparticles [125].

Imaging Photoacoustic (PAI)

With the benefits of both optical and acoustic imaging methods, PAI has received a lot of interest [126]. PAI gives three-dimensional information on the spatial distribution of light-absorbing objects deep within a live body.

In the PAI approach, a non-ionizing short-pulsed laser beam (often visible and near-infrared lasers) diffusely penetrates the tissue/phantom, portion of the laser beam's energy is absorbed and converted to heat, causing a temporary temperature rise and transient thermo-elastic expansion of the tissue, and causing wideband ultrasonic wave emission that may be collected by ultrasonic transducers [127] in the near-infrared range (900-1800 nm), water and lipids exhibit distinctive absorption peaks (fig.20)[128].

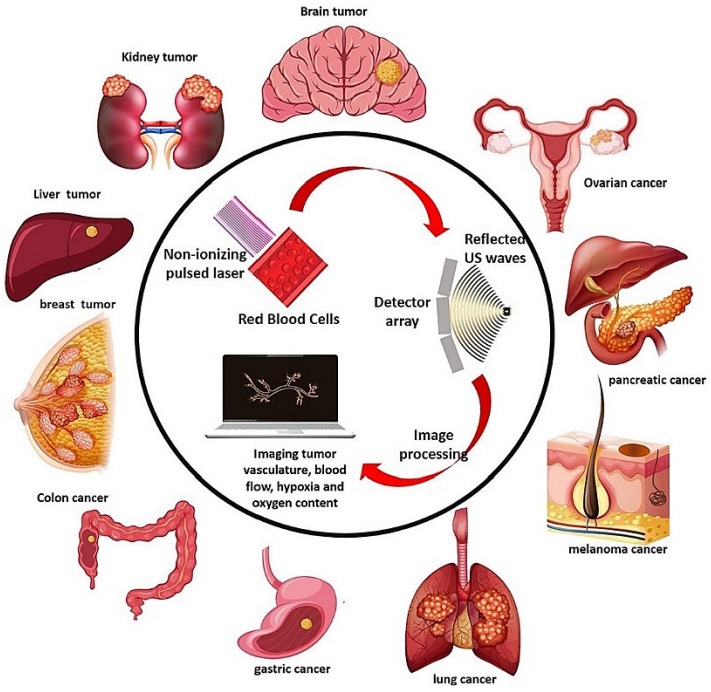

Figure 20: The basis of PAI and its clinical application for cancer imaging [128]

Numerous endogenous and exogenous contrast agents have been developed for PAI. Among endogenous contrast agents PAI can be used to image numerous endogenous biological molecules comprising haemoglobin, melanin, lipids, nucleic acids, and water by modifying the laser characteristics, while exogenous agents are chromophore small molecules, organic dyes and nanoparticles[126]. Nanoparticles for PAI comprise: **Plasmonic nanoparticles** such as gold nanoparticles, polymeric nanoparticles, and magnetic nanoparticles. When compared to small molecule dyes, the potential benefits of using plasmonic nanoparticles for PAI include (1) a high extinction coefficient and (2) tunable peak absorption wavelengths based on surface-to-volume, polarisation modes, edge/vertex number, and morphology (3) enhanced conversion effectiveness; (4) increased photostability. AuNPs have been used as a promising platform for both therapeutics and diagnostics due to their unique physical and chemical properties for PAI as plasmonic nanoparticles, such as inherent biocompatibility, ease of synthesis, and excellent light-to-heat conversion[128].

Nanomedicine combined to cell-based therapy

Although multifunctional nanoparticles have been employed as photothermal agents in cancer treatment, at this level of development, even with improved compositions of AuNPs, tumour targeting continues to be an issue. EPR and EPR/AuNPs-mediated tumour targeting exhibits significant intra- and inter-individual variation, which explains the varied results of various clinical trials. Such disadvantages have prompted efforts to find potential ways to improve patient response through therapeutic improvement of EPR, as continually discussed[129]. Cell-mediated delivery has been extensively employed in the last ten years to treat a variety of tumors, including gliomas, head and neck cancers, and breast cancers[130], [131]. Although this approach seems to be appropriate for all tumour types, not all cells can be employed to carry therapeutic payloads selectively. The cells most frequently employed as NP delivery systems in cancer therapy include platelets, polymorphonuclear neutrophils, macrophages, and a variety of stem cells, including neural stem cells (NSCs), induced pluripotent stem cells (iPSCs), mesenchymal stem cells (MSCs), and a specific subset of endothelial progenitors known as ECFC) [132], [133]. To perform this function, these cells express molecules that allow them to migrate and halt at the tumour endothelium in response to chemotactic chemicals made by the cancer cells: specialised receptors for cancer-produced chemo-attractants, intracellular contractile structures that allow them to activate the typical contraction-relaxation cycles of the cell body necessary for the "grip-and-go" cell movement process. To create a pathway through the tumor's extracellular matrix, all these cells must also generate the proteolytic enzymes required. Based on these characteristics, the following cells have been employed to release their NPs payloads or to exploit their thermo-transductive or molecular imaging potential once within tumors [134].

The CXCL12 chemokine (***SDF-1***, stromal derived growth factor) recruits cells expressing the ***CXCR4*** receptor: all the stem cells, such as neural stem cells, iPSCs, mesenchymal stem cells (MSCs), T lymphocytes, and endothelial colony-forming cells (ECFCs). The CCL2 chemokine such as monocyte chemoattractant protein-1 (MCP-1) recruit monocytes/Mϕ that express the CCR2 receptor while the CXCL1-3 and CXCL5-8 chemokines recruit neutrophils that express the CXCR2 receptor[135] (fig.21).

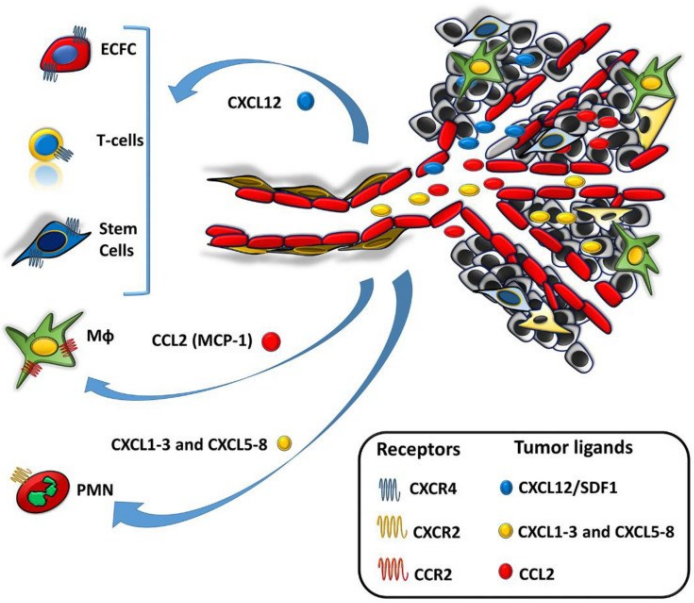

Figure 21: The main chemokine/chemokine-receptor axes involved in cell recruitment at the tumor site [135].

Endothelial colony forming cells (ECFCs)

The first description of circulating EPCs by Ashara in 1997 [136], followed by the discovery of a notable tropism of EPCs to ischemia and tumoral tissues, has inaugurated a new era of EPC-based cell-therapies, which, in the case of cancer therapy, may contribute to resolving the limitations associated with traditional chemotherapeutics [137]. The term "EPC" refers to a variety of cell types that, environmental circumstances, can move, multiply, and acquire markers of mature endothelial cells. Since Asahara's first discovery of bone marrow (BM)-derived EPCs [136], there has been debate about what defines a true endothelial progenitor, and the absence of specific markers has been combined with functional factors such as cell morphology, clonal proliferation, the ability to replicate, and the capacity to produce arteries in vivo and in vitro with tubular-like structures. Based on their phenotype in humans, Medina et al. identified two distinct populations of EPCs [138]: the early EPCs, known as myeloid angiogenic cells, which have an hematopoietic origin, and the late EPCs, known as endothelial colony-forming cells (ECFCs) [139], which have an endothelial phenotype [140] (fig.22). Numerous studies have focused on the role of postnatal endothelial progenitor cells (EPCs) in tumour vascularization and metastasis.

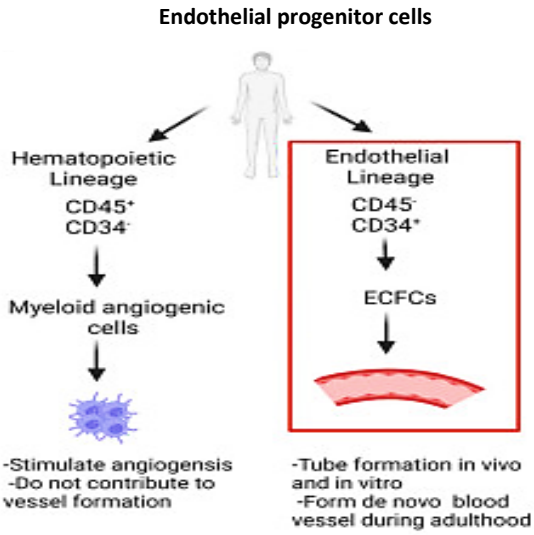

Figure 22: shows the human endovascular progenitor cells. (A) Two separate populations of EPCs, myeloid angiogenic cells and ECFCs, may be distinguished based on phenotypic lineage. Myeloid angiogenic cells induce angiogenesis but do not contribute to the formation of blood vessels, whereas ECFCs do not have hematopoietic origins but can form de novo blood vessels and colonies [140].

EPCs are present in the stem cell niche of bone marrow (BM), where they interact with bone marrow stromal cells (BMSCs). EPCs present high concentrations of the chemokine SDF1, certain integrins like 41 and 3, and low concentrations of cKit-ligand. The microenvironment is disturbed in response to tumour development, allowing EPCs to leave the BM, enter the peripheral circulation, and migrate into the tumour to establish new capillaries. Laurenzana et al. provide complete analysis of all stages of this process [137], [141].

Studies have shown that EPCs with a specific gene expression profile that are attracted into the tumour microenvironment help establish vascular pathways [140].

It was demonstrated that the formation of new blood vessels through vasculogenesis, with endothelial progenitor cells selectively recruited to injured or ischemic tissue depend to an upregulation of SDF-1 and CXCR4 in hypoxia after activation of the transcription factor hypoxia-inducible factor (HIF-1α). The expression of SDF-1 in the tumor indicates the presence of tissue ischemia, and that its expression is directly regulated by HIF-1α [142].

This suggests that EPC recruitment is dependent on chemokines in the tumour microenvironment, immune cells, and substances released by tumors cells.

Previous work in my laboratory, demonstrated the good thermo-transductive characteristics of AUNP-enriched ECFCs both in vitro and in vivo experiments, and the excellent capability to kill melanoma cancer cells at moderate NIR light intensities [120].

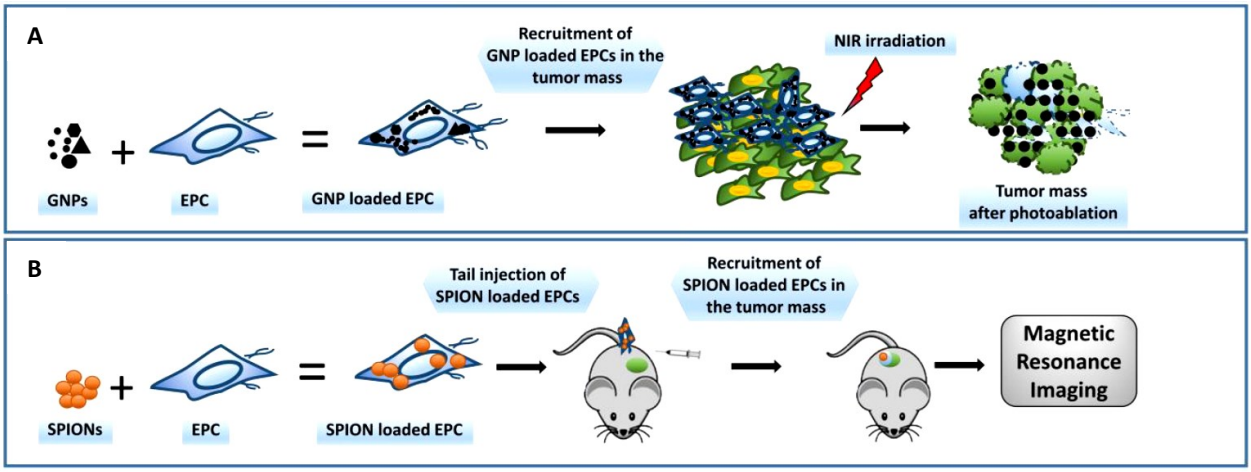

Figure 23: a) In the photothermal therapy of tumours, EPCs can be loaded with gold nanoparticles (AuNPs). AUNP-doped EPCs have the ability to warm up the tumour environment after they have entered the tumour mass at moderate near-infrared light intensities (NIR), leading to the thermos-necrosis of cancer cells. b) EPCs can be utilised as probes in nuclear medicine or optical imaging and loaded with iron oxides for MRI [137].

EPCs have also been suggested for use in diagnostics conditions. In fact, the ability to label tumor-tropic cells may allow for the parallel follow-up of the same lesions following treatment as well as the identification of primary and metastatic tumours. EPCs have been effectively employed in MRI of human breast cancer animal models [143] or in a rat model of human glioma when they were tagged with superparamagnetic iron oxide nanoparticles (SPIONs) or gadolinium. Future "theranostic" approaches for individualised tumour treatment will be made possible by the potential use of ECFCs or other tumor-tropic stem cells carrying nanoparticle payloads with therapeutic and diagnostic properties [137].

2. AIM OF STUDY

Aim of the project

Over the last years, new therapeutic strategies have been developed in cancer treatment to reduce and overcome the toxic side effects of the "classic conventional" chemotherapy and radiotherapy. Encouraging perspectives have arisen with the advent of targeted and immune modulating therapies, which, individually or in combination, have led to more prolonged clinical response. However, the majority of patients are either intrinsically resistant or rapidly acquire resistance to these anti-cancer treatments, therefore **alternative therapies** should be taken into consideration. The use of gold nanoparticles (AuNPs) has been suggested in cancer treatment, because of their ability to absorb light in the Near Infrared (NIR) window, thus conveying localized heating and subsequent "thermoablation" of target tissues upon irradiation with common lasers. Moreover, AuNPs are not toxic for cells and tissues. Unfortunately, there still remain many obstacles, mainly associated to their biodistribution. Here, we propose to overcome this barrier by using as vehicle of AuNPs a sub-type of endothelial progenitor cells (EPCs) termed "Endothelial Colony Forming Cells" (ECFCs). ECFCs display a natural tumor-homing ability, thus increasing the delivery and accumulation of NPs into tumors. Such approach establishes a new concept of cell-based therapy combined with nanomedicine. Moreover, it has been demonstrated that AuNP-dependent hyperthermia sensitizes cancer cells to radiotherapy both due to an intrinsically synergistic combination of hyperthermia and radiotherapy and thanks to the high X-ray absorbance of AuNPs, thus concurring to reduce the therapeutic radiation dose and decrease the side effects and toxicity of radiotherapy alone.

The purpose of this project is to develop a **theranostic strategy** to improve cancer therapy by combination of gold nanoparticles-dependent hyperthermia and radiotherapy in melanoma and breast cancer cells.

This project is based on the following data: ECFCs uptake AuNPs (AuNP-ECFC) and privilege homing within tumors. In contrast to what happens by injecting bare NPs, viable Au-ECFCs remain within tumors for several weeks. AuNP-ECFCs display excellent thermotransductive properties that kill cancer cells *in vitro* upon laser irradiation at moderate NIR light intensities and induce necrotization of experimental tumors in mice inoculated with AuNP-ECFCs**.**

The accumulation and biodistribution of AuNP-ECFCs can be followed *in vivo* by photoacoustic imaging (PAI), which allows to achieve maximum sensitivity and specificity for the detection of tumor mass and of macro/micro-metatases in experimental animal models.

Moreover, the presence of AuNPs within tumors results in increase of radio sensibility, thus reducing side effects and improving therapeutic result of radiotherapy.

By relying on using ECFCs as vehicle of AuNPs and on combining hyperthermia and radiotherapy, this project represents a major progress with respect to the stage of development reached thus far in cancer therapy. Nevertheless, the choice to assess different **therapeutic approaches** will allow us to overcome any potential pitfall of a single therapeutic treatment.

In the second part of the current work, we investigate the antitumoral effects in melanoma and breast cancer cells of two types of nanoparticles: 1) **Fe_3O_4 MNP** magnetic nanoparticles for drug delivery and 2)**Au@Fe_3O_4**, an hybrid metallic nanocomposite as multifunctional platform for magnetic-plasmonic applications. The study was in carried on in collaboration with Dr. Claudio Sangregorio, at the Institute of Chemistry of Organometallic Compounds, Italian National Research Council (CNR).

We demonstrated the anticancer efficacy of the above smart magnetic nanocomposites, MNCs, comprising a superparamagnetic Fe_3O_4 MNP core and a dual pH- and temperature-sensitive PVCL-co-PAA shell conjugated with an anticancer drug (doxorubicin, DOX) for multimodal cancer therapy, by combining magnetic hyperthermia and controlled drug release [144].

Subsequently, we investigated Au@Fe3O4 core@shell system with a highly uniform unprecedented star-like shell morphology with combined plasmonic and magnetic properties. Before assessing the biomedical application of this multifunctional platform, we demonstrated the Au@Fe3O4 nanostar biocompatibility on ECFCs. We then proved the photothermal effects after 658 nm light exposure and the nanoshell induction of magneto-mechanical stress by an external AMF on cell viability of MCF7 [145].

3. MATERIALS AND METHODS

Melanoma cell line: A375 (MITF wild type, BRAF V600E, NRAS wild type) was obtained from American Type Culture Collection (ATCC, Manassas,VA, USA). A375-M6 melanoma cells (**M6**) were isolated in the laboratory from lung metastasis of SCID bg/bg mice i.v. injected with A375 melanoma cells.

Melanoma cells grown in Dulbecco's modified Eagle's medium (DMEM) High Glucose with 10% FBS (Euroclone, Milano, Italy) 100 U/ml penicillin–streptomycin and 1% L-glutamine 200 mM (Euroclone) in a humidified 5% CO_2 atmosphere at 37 °C. Cells were harvested from subconfluent cultures by incubation with a trypsin–EDTA solution (Euroclone) and propagated every 3 days at a ratio between 1:5 and 1:10.

Breast cancer cell line: Human hormone-sensitive breast adenocarcinoma cell line **MCF-7** was obtained from American Type Culture Collection (ATCC, Manassas,VA, USA). Human MDA-MB-231 (**MDA**) is an aggressive and invasive hormone-independent breast cancer cell line, which lacks ER, PR and HER2. Cells were obtained from the American Tissue Culture Collection (Manassas, VA, USA).

Breast cancer cells were cultured in Dulbecco's modified Eagle's medium (DMEM, supplemented with 10% foetal bovine serum (Euroclone), 100 U/ml penicillin–streptomycin and 1% L-glutamine 200 mM (Euroclone) in a humidified 5% CO_2 atmosphere at 37 °C. Cells were harvested from subconfluent cultures by incubation with a trypsin–EDTA solution and propagated every 3 days at a ratio between 1:3 and 1:6.

Endothelial colony forming cells (ECFCs): Human umbilical cord blood (UCB) samples (volume > 50 mL) were collected in citrate phosphate dextrose solution from health newborns. We used cord blood units with a number of total nucleated cells < $1.3x10^9$ (threshold of suitability for the banking established by the Umbilical Cord Bank of Careggi, Florence, Italy) after maternal informed consent in accordance with the Declaration of Helsinki and in compliance with Italian legislation. EPCs have been isolated from UCB as described[146]. Blood was diluted 1:1 with Hanks balanced salt solution (EuroClone) and was overlaid on an appropriate volume of density gradient separation medium (Lympholyte; Cedarlane). Cells were centrifuged for 30 minutes at room temperature at 740*g*. Mononuclear cells were recovered, washed 3 times with Hanks balanced salt solution and resuspended in complete EGM-2 medium (Lonza) supplemented with

10% FBS (Euclone), 50 ng/mL VEGF (PeproTech) and 5 U/mL heparin. Cells were seeded on gelatin-coated 6-well tissue culture plates at a density of $5x10^5$ cells/cm^2 in a 5% CO_2 humidified incubator at 37°C. On days 4 and 7, half of the medium was exchanged with fresh medium. Then the medium was changed completely with EGM2–10% FBS every 3 days. EPC colonies appeared in cell cultures after 2-3 weeks and were identified as circumvented monolayers of cobblestone-like cells. The colonies were mechanically picked from the original plate and seeded on another gelatin-coated well with EGM2–10% FBS for expansion. These cells can be maintained in culture for 8-10 passages.

Flow cytometric analysis: ECFCs were CD31+, KDR+, CD105+, ULEX+, vWF+, CD45-, CD34-. The characterization was based on flow cytometric analysis. ECFCs were analyzed for the expression of typical surface staminal, endothelial or monocyte-macrophage antigens by flow cytometry. To recognize surface antigens, it was necessary to use fluorochrome-labeled monoclonal antibodies. The fluorochrome that we used was phycoerythrin (PE-red) and fluorescein (FITC-green). Both are exited at wavelength of 488 nm (blue), so they can be used together for an extremely sensitive detection system in the double labeling. To characterize the cells obtained by the technique described above, first, washed cells were resuspended in flow cytometry buffer (CellWASH 0.1% sodium azide in PBS, BD Biosciences). Aliquots ($0.1x10^6$ cells/100 µL) were incubated with the following conjugated monoclonal antibodies: CD45-FITC, CD34-FITC, CD31-FITC (all from BD Biosciences PharMingen); CD105/R-phycoerythrin (Ancell); ULEXFITC (Vector Laboratories); phycoerythrin-labeled by Tetra-Tag phycoerythrin- labeling kit (StemCell Technologies) KDR (RELIATech), uPAR/R3 (BioPorto Diagnostic A/S), and vWF (BD Biosciences PharMingen). Nonspecific fluorescence and morphologic parameters of the cells were determined with isotype-matched mouse monoclonal antibodies (BD Biosciences PharMingen). All incubations were done for 20 minutes; and, after washing, cells were resuspended in 100 µL of CellWASH. 7-Aminoactinomycin (BD Biosciences PharMingen) was added to exclude dead cells from the analysis. Flow cytometric acquisition was performed on a FACSCalibur (BD Biosciences) instrument.

Morphogenesis capillary assay: The capillary morphogenesis assay on Geltrex was used to determine the potentialof ECFCs to differentiate into capillary-like structures. 50 µl of a Geltrex solution were placed (Geltrex™ LDEV-Free, hESC-Qualified, Reduced Growth Factor Basement Membrane Matrix, Thermofisher) into each well of a 96-well plate. Geltrex polymerize after being placed for 30 minutes at 37°C in 5% CO_2. $18x10^3$ cells are resuspended in 200 µl of EBM-2

with 2% and then plated in each well. Each experiment was perfomed three times, and images acquired at 6 and 24 hours with EVOS xl core microscope (AMG, Advanced Microscopy Group).

Treatment with gold nanoparticles: *Gold nanorods* were synthesized using standard techniques at the CNR IFAC Unit. According to the overall approach, a set of procedures based on the separation of the particle's nucleation and growth stages in two subsequent reactions will be used. The first reaction produces Au nuclei by rapid reduction of precursor chloroauric acid with sodium borohydride and cetrimonium bromide as a surfactant. The usual result is an ochre suspension with a weakly defined plasmon band. In the following reaction, gold nanorods are synthesized using slow cloroauric acid reduction and, as precursors, a small amount of silver nitrate in the presence of a mixture of reducing agents such as ascorbic acid, hydroquinone. Gold nanorods are stabilized with thiosulfate and coated with chitosan through a process of passive adsorption and crosslinking of the cationic polysaccharide on the anionic particles. To reproduce this concept, an anionic polymer commonly used in the case of gold nanorods such as polystyrene sulphonate (PSS) was used. Finally, the synthetic protocol involves an overnight incubation of the cetrimonium-stabilized particles with 0.15% Na+-PSS and 0.5 mM cetrimonium, at the nominal concentration of 1.6 mM Au, followed by 3 centrifugation cycles at 11,000 rcf for 25 min and resuspension in 0.15% Na+-PSS. Subsequently, the particles are incubated with a solution of 0.15% chitosan in 1.5% citric acid for 24 hours and, finally, washed with ultrapure water and reconstituted at the nominal concentration of **4 mM** Au. Before the biological tests, all samples were sterilized with standard autoclave treatment. The concentration used for the treatment of the cells is 100 µM AuNPs overnight.

Cells viability was determined with trypan blue staining: 20 µL of cell suspensions was resuspended with an equal volume of 0.4% (w/v) trypan blue solution prepared in 0.81% NaCl and 0.06% (w/v) dibasic potassium phosphate. Viable and non-viable cells (trypan blue positive) were counted separately using a dual chamber hemacytometer and a light microscope.

Transmission Electronic microscope (TEM) analysis: tumor cell lines and ECFCs were seeded in 6-well plates at a density of 1.5×10^5 cells well and allowed to reach 70% confluency. Subsequently, cells were incubated with culture medium (2 mL per well) containing suspensions of AuNPs at a concentration of 100 mM Au for 3h, overnight and overnight + 3 h (double dose), then harvested by trypsin treatment after 24 h of incubation and centrifuged at 1000 rpm for 5 minutes in a 1.5 mL Eppendorf tube.

The cell pellet was then fixed in 4% isotonic glutaraldehyde and 1% OsO_4, dehydrated and embedded in epoxy resin for electron microscopy. Ultrathin sections were stained with aqueous uranyl acetate and alkaline bismuth subnitrate and viewed and photographed under a JEM 1010 transmission electron microscope (Jeol, Tokyo, Japan) equipped with a MegaView III high-resolution digital camera and imaging software (Jeol).

Photoacoustic imaging (PAI): ECFCs and tumor cells were seeded in 6-well plates at a density of 1.5×10^5 cells per well. Once 70% confluency was reached, they were treated with AuNPs for 3 hours, overnight, and with a double administration overnight and 3 hours. Cells were incubated with culture medium (2 mL per well) containing suspensions of AuNPs at a concentration of $100x10^{-6}$M Au for the indicated time points, then harvested by trypsin treatment and centrifuged at 1000 rpm for 5 minutes in a 1.5 mL Eppendorf tube. Cells were fixed in PFA 4% and kept at +4°C until imaging.

Inductively Coupled Plasma – Atomic Emission Spectrometry (ICP-AES): Tumor cell lines and ECFCs cells (3.0×10^5) were seeded 6-well plates and allowed to attach overnight. On the next day, cells were incubated with culture medium containing AuNPs for 3 h, overnight and overnight + 3h. Cells were then washed two times with PBS (Invitrogen), detached with a trypsin treatment, and counted using a hemocytometer. Cell pellets were collected by centrifugation, lyophilized, and placed in centrifuge tubes (one pellet per tube). Then, 400 µL of aqua regia was added to each tube to completely dissolve the cells and their gold content. The amount of Au was measured by Elan DRC II ICP-MS (Perkin Elmer, Waltham, MA).

Transfection in M6: A lot of strain VB ultrastrable bacteria was purchased. This bacteria contain the plasmid of our design VB900088-2285gqt (GFP2) with the VectorBuilder online program and ordered via the VectorBuilder service (Cyagen Biosciences Inc.,Santa Clara, CA). The bacteria were grown in Luria-Bertani (LB) with Ampicillin 100 µg/ml, when they are amplified, the plasmid was isolated according to the protocol of Qiagen® plasmid midi kit, using the kit according to the instructions. Subsequently the plasmide was transfected (1µg/ml) into M6 cell using Lipofectamine® 3000 according to the instructions.

Tumor Spheroid Formation and co-colture with ECFC: M6 transfected with GFP2 monolayers were washed with PBS and then harvested using Trypsin, collected, and centrifuged at 500 x g for 5 min. Supernatant was removed and the pellet resuspended in 1mL complete growth medium. 5000 cells/well were seeded dispensing 200 µL per well into a 96-well flat-bottomed

plate precoated with 1.5% Agar. The plate was centrifuged at 500 x g for 5 min and then transferred to an incubator (37°C, 5% CO2, 95% humidity).

Ten days after tumor spheroid formation, we proceeded with stratification of 1000 ECFCs un/loaded with AuNps and labelled with the membrane probe, PKH26 (Sigma-Aldrich). Confocal microscopy was used to determine ECFCs tumor spheroid migration.

in vivo **Tumor cell inoculation and ECFC injections:** Nude female rats (NIH-Foxn1 rnu in heterozygous) athymic (immunosuppressed) were purchased from Charles Rivers Laboratories International (Wilmington, Massachusetts, United States) and manipulated to evaluate the tumor tropic action of AuNPs-loaded ECFCs. 15 rats (20 weeks old and weighing about 200 grams) following isoflurane anaesthesia were inoculated subcutaneously at the level of the right and left flank with $2.5x10^6$ A375-M6 melanoma cells. It was determined that all rats had palpable tumour masses one week after the tumour cells were inoculated, using ultrasound and photoacoustic imaging. At this time, the control ECFCs and those previously loaded with AuNPs were injected into the rats' tail veins while they were still under isoflurane anaesthesia. Two inoculations of control ECFCs and two inoculations of AuNPs-loaded ECFCs were carried out. The presence of gold in the serum was determined by photoacoustic imaging the day after inoculation. The day following injection, photoacoustic imaging was done using an optical microscope and a digital camera to assess if gold was present in the tumour mass. Palpable tumour was present one week after the tumour cells were inoculated. The tumour masses were removed from each animal after sacrifice, along with other organs such the kidneys, spleen, lungs, and liver, in order to conduct immunohistochemistry analyses and assess the presence of nanoparticles. The organs were extracted and then preserved in 10% formalin (65-30001F – Bio-Optica Milano Spa, Milano, Italia) for one week. Histological analyses were performed on paraffin embedded section.

Immuno-histochemistry: 5 µm thick paraffin-embedded tumor sections were collected on glass slides. After deparaffinization, through a series of solutions (100% xylene through 100% ethanol to 100 water), slides were staining with haematoxylin -eosin (haematoxylin Gill 3, 05- 06015L – Bio-Optica Milano Spa, Eosin Y alcoholic solution, 05- 10003/L – Bio-Optica Milano Spa).

Immunoistochemistry: After deparaffinization, slides were boiled for antigen retrieval in buffer citrate and treated with 3% H_2O_2. The slides were subsequently blocked with 1,5% BSA and incubated with: *CD31* (1:000 Rabbit mAb #SAB560006, Sigma Aldrich), *PCNA* (1:1000 Mouse mAb

#PC10, Cell Signaling Technology) and *HIF1α* (1:100 Mouse mAb #D5F3M, Cell Signaling Technology) overnight at 4°C. Probed slides were then subjected to secondary antibody specific for the primary serotype. The antibody binding activity was detected using avidin-biotin-peroxidase complex method and diaminobenzidine tetrahydrochloride chromogen kit (Dako LSAB2; Dako Corporation, Carpinteria, CA).

Co-colture: $8x10^5$ A375-M6, or MCF7 were seeded in T-25 flask with $2x10^5$ ECFCs loaded or unloaded with AuNPs (1:5). The cells were cultured in Dulbecco's modified Eagle's medium (DMEM), supplemented with 10% fetal bovine serum (Euroclone), 100 U/ml penicillin–streptomycin and 1% L-glutamine 200 mM (Euroclone) and complete EGM-2 medium (Lonza) in a humidified 5% CO_2 atmosphere at 37 °C. The day after untreated flasks (M6-ECFCs and M6-ECFCs AUNPs) remain at 37° while the others will undergo Xray radiation (IR) 2 GY, laser-induced hyphertermia (HT) or combo treatment (IR+ HT). Evaluation of the long- and medium-term biological effects were investigated according to the experimental procedure in fig. 25.

Cell Irradiation: Two metastatic melanoma cell lines (A375 and M6) and breast cancer cell lines (MDA and MCF-7), were exposed to increasing doses of X-rays in order to assess which radiotherapy dose could be chosen for the combined effect with hyperthermia (0Gy, 2Gy, 4Gy, 6Gy). The cell cultures were irradiated using a linear accelerator (LINAC) at AOUC- UO Radiotherapy. To mimic the physiological conditions, the flasks were filled entirely with cell culture medium, removed 2 hours after exposure and proceeded with the experiments.

AuNP-dependent hyperthermia therapy: The hyperthermia tests were carried out using a setup developed by the CNR IFAC Unit (figure 24a). This consists of a chiller and a custom multiwell to thermostating the samples in the well (see below and figure 24b). The angle of view of the thermowell from the thermal camera was considered by a collimator which allows the line-up of the laser source with the objective of the thermal camera, so that the irradiation and thermography occur in a quasi-confocal manner. Finally, an ad-hoc support used to fix the relative position between the multiwell and the thermal imaging camera, resulted in thermal images of better quality than those previously obtained.

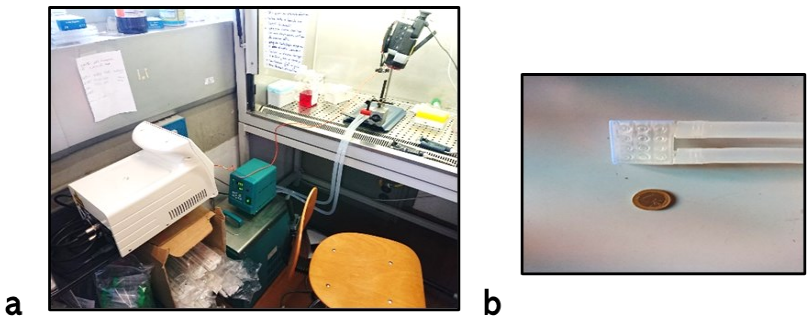

Figure 24: a) View of the setup optimized for in vitro hyperthermia testing. In the image it is visible, from left to right: the laser (white), with the fiber (orange) for the transmission of light up to the collimator; the chiller (green), with the relative connection pipes for the delivery and return of the heating fluid; the assembly of the collimator support and the IR thermal camera, facing a thermostated multiwell chip. b) Top view of a custom multiwell chip developed to allow sample thermostatation.

The laser source consists of an AlGaAs diode laser (El.En., mod. WELD 800) with optical emission at 810 nm, maximum output power of 10 W, pulsed or continuous emission mode and optical fiber coupling for use under a biological hood and an IR camera (FLIR System, mod Thermovision A20). To realize the custom multiwell we took advantage of the availability of latest generation additive technologies, namely two FDM (Fused Deposition Modeling) type printers and one SLA (StereoLithography Apparatus) type, the kit necessary for the finishing of the pieces; a library of polymers and resins and two design workstations in a CAD environment, which allowed to create multiwell chips of optimized dimensions to host cell suspensions with representative densities of the tumor microenvironment and immersed in a thermostatic bath coupled to a chiller. It was investigated the possibility of integrating the multiwell chips into a stand suitable for standardizing the configuration of the optical fiber and the IR camera.

To perform hyperthermia tumor cells lines, ECFCs and relative co-cultures were harvested by trypsin, centrifuged and the pellet resuspended in a volume of 100 µl, in order to obtain a cell-dense cell suspension. The suspension was then introduced into the well hit by the laser beam at a power of 1.0 w CW for the time necessary to reach the temperature of 43° (about 2 minutes). The cells were then counted using a dual chamber hemacytometer and subjected to the additional evaluation such as clonogenic assay, western blot analysis and comet assay).

Clonogenic Assay: For colony formation assay, 1000 cells were seeded in six-well plates in triplicate, immediately after the cells have been exposed to treatment (radiotherapy, hyperthermia). Colonies were counted following may grunwald-giemsa staining after 10 days. The colonies formed were counted and then the **plating efficiency** was calculated[147].

$$PE = \left(\frac{n° \, of \, colonies \, formed}{n° \, of \, cells \, seeded}\right) \times 100$$

The number of colonies that arise after treatment of cells, expressed in terms of PE, is called the **surviving fraction** (SF) [147]:

$$SF = \left(\frac{n° of \, colonies \, formed}{n° of \, cells \, seeded}\right) \times PE$$

All data obtained were normalized respect to control (untreated).

Western blot: Cell pellets obtained by centrifugation were incubated with RIPA lysis buffer (50 mM Tris (pH 7.4), 150 mM NaCl, 1% Triton X-100, 1% sodium deoxycholate, 0.1% SDS, 5 mMEDTA) and proteinase inhibitor cocktail (Roche, Mannheim, Germany) for 30 minutes on ice and treated by sonication (Microson XL-2000, Minisonix, Farmingdale,NY, USA) for 20 min. Lysates were then centrifuged at 14,000 r.p.m. for 10 minutes. Aliquots of lysates (40 µg) of M6, MCF7, ECFCs and co-culture M6-ECFC and MCF7-ECFCs cells, loaded and unloaded with AuNPs, in Laemmli buffer were separated on Bolt Bis-Tris Plus 4–12% precast polyacrylamide gels (Life Technologies, Monza, Italy). Fractionated proteins were transferred from the gel to a PVDF nitrocellulose membrane using an iBlot 2 system (Life Technologies, Monza, Italy). Blots were stained with Ponceau red to ensure equal loading and complete transfer of proteins, and then blocked for 1 h at room temperature with 5% milk in PBS containing 0.1% Tween. Subsequently, membranes were probed at 4 °C overnight with rabbit anti PARP (46D11) antibody (1:1000, Cell Signaling), rabbit anti Phospho-Histone H2AX (Ser 139) antibody (1:1000, Cell Signaling), rabbit anti GAPDH (1:000, Cell Signaling), mouse anti α-tubulin antibody (1:1000 Cell Signaling) used to assess equal amounts of protein loaded in each lane. Antirabbit IgG (whole molecule)–Peroxidase antibody (Sigma, Cat#A0545) or antimouse IgG (whole molecule)–Peroxidase antibody (Sigma, Cat#A9044) were used as secondary antibodies; the enhanced chemiluminescence ECL (Bio-Rad) procedure was employed for development.

Quantification of western blot protein bands was performed with ImageJ software (java-based freeware http://rsb.info.nih.gov/ij/) comparing the density (i.e., intensity) of the bands. The density is expressing of the selected bands against a standard band selected during this process (loading control such as GAPDH or α-tubulin). Finally, statistical analysis was applied (Mean SE and T-test).

Comet assay: DNA damage was measured as described [148]. The standard alkaline procedure was used to measure the level of DNA strand breaks (SBs). Tumor and ECFCs co-culture were frozen at −80 °C in aliquots containing $1x10^5$ cells/100 µL freezing medium (medium with 40% FBS and 10% DMSO); each aliquot was mixed with 280 µL 1% low melting-point agarose (LMP) in PBS in order to achieve 0.75% LMP agarose final concentration and used to prepare duplicate gels for each sample (20,000 cells/gel) on Gelbond Films (Lonza, Basel, Switzerland). Gels were covered with a 13 x 13 mm coverslip and allowed to solidify for 10 min on an ice-cold metal surface. After gel solidification, the slides were placed in lysis solution (2.5 M NaCl, 0.1 M Na_2EDTA, 10 mM Tris and 1% Triton® X-100, pH 10) for 1 h at 4 °C. All slides were submerged in unwinding solution (300 mM NaOH and 1 mM EDTA) for 40 min at 4 °C, and electrophoresis took place in this solution for 30 min at 0.8 V/cm, 300 mA, 4 °C. The slides were finally neutralized with PBS, washed in dH_2O and let dry at room temperature.

Image analysis Slides were stained with SYBR Gold® (Invitrogen, diluted 1:10.000 in 10 mM Tris-HCl/1 mM EDTA, pH 8.0); scoring was performed with the Comet Assay IV® software (Perceptive Instruments, UK). For each gel, 50 cells were scored making a total of 100 per sample. Data were expressed as % tail DNA (mean ± SE of 3 experiments).

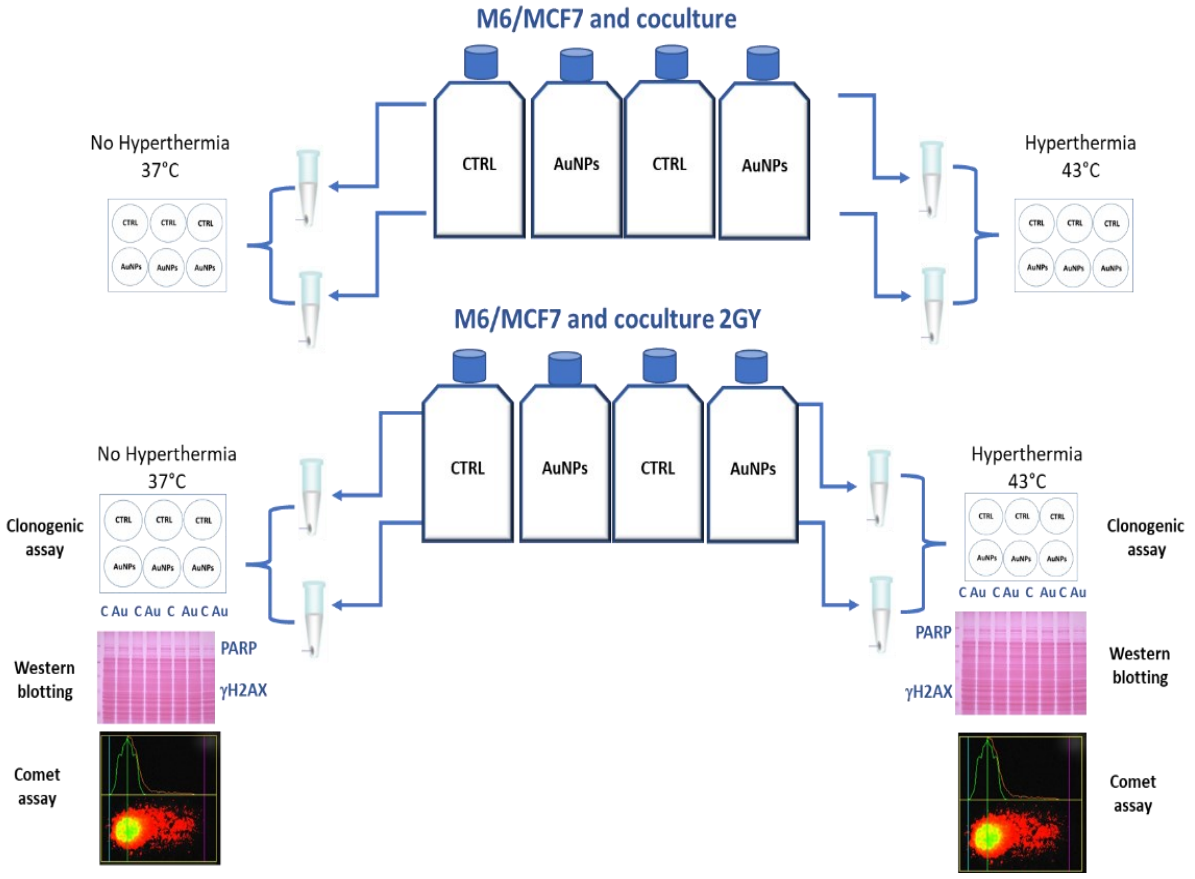

Figure 25: Schematic representation of the experiment design: cell lines MCF7, M6, MCF7-ECFCs, M6-ECFCs respectively loaded or not with AuNPs were seeded in T-25 and then subjected to irradiation (IR) and to Hyperthermia (HT) until they reached temperature is 43°. After single or double treatment , cells were processed to evaluate short and long term cytotoxic/cytostatic effects by carrying out: clonogenic assay, western blot analysis of DNA damage and comet assay.

In the second part of the current work, for the investigation of the use of *Fe_3O_4 MNP* magnetic nanoparticles for drug delivery and *Au@Fe_3O_4* for photothermal therapy; we applied the following methods:

Cytotoxicity Assay and Cellular Uptake Study in Fe_3O_4 MNP: Since DOX is one of the most effective anticancer drugs used for the treatment of solid tumors of diverse origins and in particular for breast cancer, MCF7 (breast cancer cell line) and A375 (melanoma cell line) were selected for the cytotoxicity tests and cellular uptake evaluation of drug nanocarriers.

A375 and MCF-7 cell lines were grown in culture dishes as a monolayer in DMEM supplemented with 10% FBS, in a humidified atmosphere with 5% CO_2.

WST-1 assay: Cell viability of A375 cells against MNCs, free DOX, and DOX-MNCs was assessed by wst-1. Cells were seeded on a 96-well plate at a density of 5.0×10^3 cell/well and incubated at 37 °C under 5.0% of CO_2 for 24 h. Then, cell culture medium was substituted with 100 µL of a fresh medium containing testing samples with different concentrations and incubated for 6 h. After incubation, the samples were removed, and 10.0 µL of cell proliferation reagent WST-1 was added to each well and incubated for 1 h. Then, the absorbance of samples was measured in a microplate reader at λ= 450 nm to calculate the viability of cells.

In parallel, wells containing just cells with the culture medium were used as control, whereas wells with culture medium, MNCs, free DOX, or DOX-MNCs without cells were used as blank.

Viability of tumor cells was determined by trypan blue staining. Cells ($1.^5 \times 10^5$) were seeded in 6-well plates and allowed to attach overnight. On the next day, MNC colloidal suspensions were added at the indicated concentrations. Six hours later, cells were aseptically transferred to a 1.5 mL clear Eppendorf tube and incubated at room temperature or stimulated with AMF for 20 min. Then, 20 µL of cell suspensions were resuspended with an equal volume of 0.4% (w/v) trypan blue solution prepared in 0.81% NaCl and 0.06% (w/v) dibasic potassium phosphate. Viable and non-viable cells (trypan blue positive) were counted separately using a dual-chamber hemocytometer and a light microscope. The means of three independent cell counts were pooled for analysis.

Confocal fluorescence microscopy was used to observe the intracellular uptake and distribution of DOX-MNCs. In total, 20.0 µL aqueous solution of DOX (0.58 mg mL^{-1}, 1.0 mmol L^{-1}) was added to 485.0 µL of sample A 7.4 and the volume of the mixture was adjusted to 2.0 mL by addition of buffer phosphate 10 mM, pH = 7.4. Afterward, the mixture was incubated at 25 °C for 24 h, and then DOX-MNC suspension was dialyzed against buffer phosphate 10 mM, at pH = 7.4 by dialysis membrane bag (MWCO ~1 kDa) for 2 h. The final suspension contains 0.34 mg mL^{-1} Fe_3O_4 MNPs and 10 µmol L^{-1} DOX as evaluated by ICP and UV-Vis spectroscopy at λ = 480 nm, respectively.

Cellular uptake evaluation: A375 and MCF7 cells were grown overnight in 18 mm glass coverslips with 10% DMEM for 24 h. The culture medium was replaced with DOX-MNCs (0.0058 mg mL^{-1} ~10.0 µmol L^{-1} DOX and 0.34 mg mL^{-1} Fe_3O_4) and then incubated 6 h. Finally, cells were fixed with 4% paraformaldehyde, and mounted with Prolong Antifade Mounting Medium on a clean glass slide. Slides were observed under a fluorescence confocal microscope FACSCAN LSRII (Becton–Dickinson, laser irradiation 530 nm).

Cytotoxicity Assay and Cellular Uptake Study in $Au@Fe_3O_4$: ECFCs (EGM-2 culture medium; Lonza) were seeded in six-well plates at a density of 1.5×10^5 cells per well in a humidified atmosphere with 5% CO_2 and then incubated with a culture medium (2 mL per well) containing $Au@Fe_3O_4$ nanostars at increasing concentrations 10, 20, and 50 µg/mL for 24 h. Cell cytotoxicity was determined with trypan blue staining. Magneto-mechanical stress and optical properties were assessed on the breast cancer cell line (MCF7). MCF7 cells were grown in culture dishes 35 mm diameter as a monolayer in DMEM supplemented with 10% FBS. Cells were incubated with $Au@Fe_3O_4$ nanostars (50 µg/mL) for 24 h. Then, cells treated either with $Au@Fe_3O_4$ nanostars or vehicle (H_2O_2) were exposed for 30 min to external AMF oscillating at low frequencies (10 Hz with 160 mT amplitude). After that, the exposure cell suspensions were re-seeded, placed again in a humidified atmosphere with 5% CO_2 for additionally 24 h, and counted the next day with trypan blue staining. To test the photothermal effect after light exposure, vehicle- and $Au@Fe_3O_4$ nanostar-treated MCF7 were washed two times with phosphate buffered saline (Invitrogen) and detached with trypsin. After centrifugation, the pellets were resuspended in 15 µL of DMEM and placed with a capillary tip in a quartz capillary which was then subjected to 658 nm laser for 30 min. Cell suspensions were re-seeded and counted the next day with trypan blue staining. Optical microscopy was used to assess qualitative intracellular uptake of $Au@Fe_3O_4$ nanostars. Cellular images were acquired through the EVOS xl core microscope (AMG, Advanced Microscopy Group).

Statistical analysis Data were analyzed using GraphPad Prism6 and expressed as a mean value ± SD. Statistical analysis was performed using one-way ANOVA.

4. RESULTS

Preliminary data

In our laboratory we have shown that ECFCs: 1) incorporate great amount of AuNPs with different shape and size (Aumix); 2) have excellent thermotransductive properties in vitro and in vivo; 3) preferentially home into human melanoma via the CXCR4/SDF1 axis [149] .

Aumix were synthesized by Dr. Giancarlo Margheri, CNR Sesto Fiorentino [150]. Figure 25a shows a typical TEM image of as-produced Aumix. A typical UV-Vis extinction spectrum of the colloidal solution is reported in 26b, with two absorption peaks due to the surface plasmon resonance. In Figure 26 we have shown an image of the photothermal profile of our colloidal gold solution, capable of reaching temperatures of up to 60°, if exposed to a modest intensity NIR source.

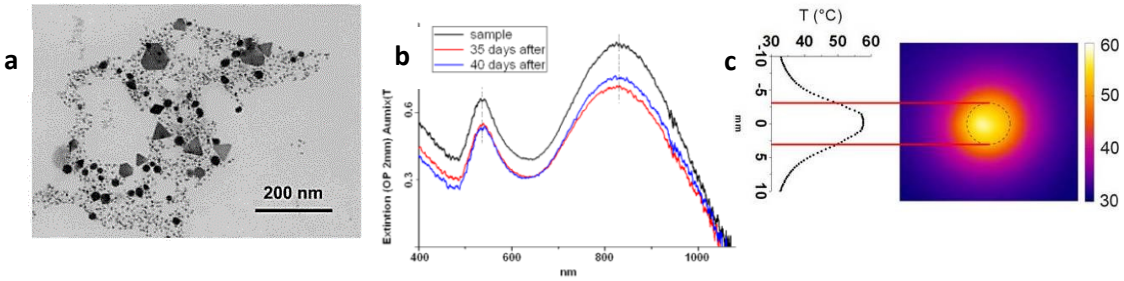

Figure 26: NP characterization a) TEM image of Aumix, b) spectrum of as-synthesized chitosan-capped Aumix (black) and after 35 days (red) and 40 days (blue), which demonstrates the stability of our NIR-AuNPs c) thermography of the NIR-sensitive colloids during irradiation; the dashed circle in the thermograph corresponds to the well containing the irradiated sample[120].

Cellular uptake as observed with a conventional optical microscope under white light illumination and TEM that permit to identify Aumix. Figure 27a shows the internalized metal loads into ECFCs, identifiable as the black areas inside the cells. As it be shown in the NIR-irradiation tests performed on liquid PBS (Phosphate Buffered Saline) suspensions of Au-doped on ECFCs (Figure 27b, upper). The thermal kinetics of the suspension (not reported) allowed us to calculate his MHR, that resulted (1400°C s^{-1} M^{-1}). However, MHR does not consider the effects of strong packing, as in ECFCs. It is well known [151] those strong nanoparticles packing reduces the interparticles distances producing a shift of the absorbance spectrum with a consequent loss of infrared light absorption per each particle and a reduction of the MHR. Luckily, the reduced MHR of ECFCs is widely balanced by the huge uptake of gold nanoparticles by the cells so that the heat power produced by enriched ECFCs is much higher, and, therefore, much higher temperatures can be reached in tumors. Through to may-grunwald-giemsa staining that permit to shown necrotic of cells culture (fig. 27b). Taking advantage on *in vitro* tests, we performed preliminary

measurements to evaluate the *in vivo* photothermal potentials of Au-laden ECFCs. A mixture of 1.5×10^6 viable A375 cells were injected into 8 weeks old CD-1 nude together with 3×10^5 Au-rich ECFCs (100 pg/cell) or vehicle treated ECFCs. After the tumors reached a volume of 100 mm^3, they were exposed to an 808 nm laser at a power density of 1 Wcm^{-2}. The surface temperature was monitored during irradiation via a FLIR thermocamera, while the temperature monitoring at a depth of ~6 mm is performed with a thermocouple gauge. Figure 27b (below) shows the thermographic images of tumor mass and the hyperthermic temperatures are obtained. According to haematoxylin and eosin (H&E) staining results, common features of thermal necrosis such as loss of nucleus, cell shrinkages, and coagulation were found in tumor tissues from mice with Au-doped ECFCs and exposed to NIR.

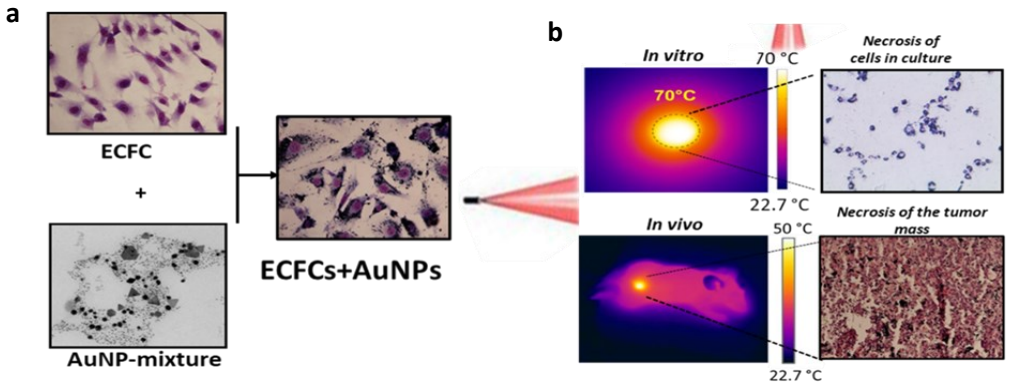

Figure 27: *in vitro* and *in vivo* NIR irradiation**.** AuNP-enriched ECFCs exhibit excellent photothermal conversion properties as well as the ability to kill cancer cells *in vitro* upon laser irradiation at moderate NIR light intensities and to induce a considerable necrotization of tumor in melanoma bearing mice inoculated with AuNP-loaded ECFCs.

Production of gold nanoparticles absorbing light in the Near Infrared window (NIR-AuNPs)

To optimize the photothermal application, in the current work, were synthesized cylindrical-shaped gold nanoparticles, called nanorods (AuNPs) which present singular plasmonic properties particularly attractive for hyperthermia. Indeed, nanorods are used for their ability to absorb near-infrared energy and release it in the form of heat to the surrounding environment, causing a localized increase in tissue temperature, a phenomenon called thermoablation. Figure 28 shows their rod structure. The composition of the crescent solution determines the length to average diameter ratio of the prolate particles in a typical range of 3 to 6, which corresponds to a longitudinal band of plasmonic oscillations between 600 and 1200 nm and a color that ranges from blue to red. The transverse diameter of these particles is typically 10 nm. This type of gold nanoparticles also stands out because it has a peculiar deafening spectrum composed of two peaks, one between 500 and 550 nm and one between approximately 700 and 900 nm. In order to investigate photothermal and photoacoustic applications, was used an 810 nm laser source. In view of in vivo applications, although normal tissues can absorb visible light, the use of a NIR laser allows to have a minimal risk of damage to healthy tissues.

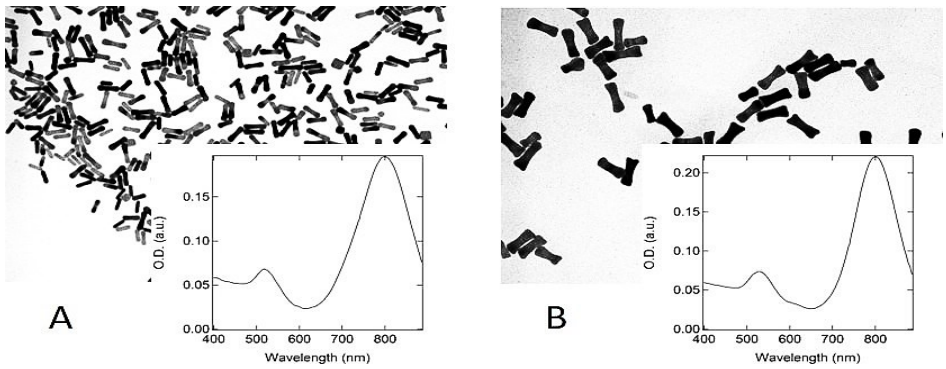

Figure 28: TEM images of gold nanorods taken by solution. Optical absorption spectra with various average diameters. a) Particle size is around 10 nm 40 nm, in b) it is approximately 5 nm 20 nm (diameter length).

Comparative study of AuNP Uptake

We previously demonstrated that ECFCs robustly internalize AuNPs mix without eliciting cell toxicity [120]. In order to prove that ECFCs are capable to internalize massive amount of AuNPs, we investigated whether multiple treatments of ECFCs with AuNPs increase intracellular load (100 µM and 150 µM), and we compared this to other two cell lines that showed tropism to tumor: mesenchymal stem cells (MSC) and macrophages (RAW 264.7)[122], [130]. We investigated and estimated the quantity of internalized AuNPs in MSCs and RAW.264 using optical microscopy (Figure 29 b, c). The cellular uptake of AuNPs was quantitatively evaluated using inductively coupled plasma-atomic emission spectroscopy (ICP-AES) after incubation of the cells with AuNPs overnight (Figure 24 d). We compared the results to those seen in ECFCs respect these two cell lines RAW 264.7 and MSCs ingested considerably less AuNPs than ECFCs following an overnight treatment, as seen in images in Figure 29a. Massive AuNPs aggregates, were present in the culture media of MSCs and were made more evident by May-Grunwald staining (lower row of Figure 29a) [152]

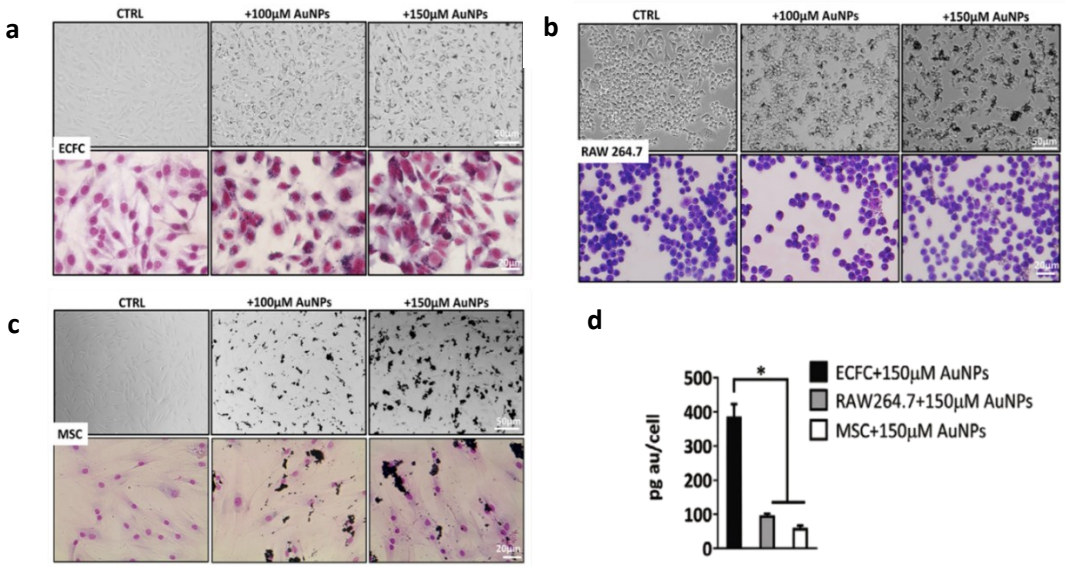

Figure 29: a) Optical microscopy images of the comparative AuNP uptake in three different tumor tropic cells line. In upper panel images of no stained and in the lower panel may grunwald-giemsa stained; untreated (CTRL) and cells treated with increasing concentrations of AuNPs (100 µM or 150 µM); the inner gold content appears as black spot in the cells. Experiments were performed in triplicate. b) dose of AuNPs, inner the cells, was quantified by ICP analyses [152].

Results: Preparation of experimental systems

in vitro: Comparative Gold Nanords uptake in tumor cells

Considering that a critical parameter for the efficacy of nano-cell-mediated hyperthermia is the load capacity of the cells and therefore the quantity of carried gold, the research activity has focused on the development of experimental protocols for the optimization of the intracellular incorporation of AuNPs. For this purpose, the cells were treated with two different doses of gold nanoparticles for increasing times and the effects on cell viability were determined.

MDA, MCF7, A375, and M6 AuNPs uptake was examined in a comparative study in parallel with ECFCs. The tumour lines were treated for 3 hours, overnight (o/n) and with a double dose, overnight and for an additional 3 hours (100+100 µM), to evaluate the kinetics and incorporation ability. The NPs appear as aggregates of black spots. Exposure of melanoma cells line (M6 and A375) and breast cancer (MCF7 and MDA-MB 231) resulted in a dose and time-dependent cellular uptake as observed even with a conventional optical microscope under white light illumination. Figure 30 clearly shows the internalized metal loads identifiable as the black areas inside the cells. In figure 30, it is shown that after 3 hours all tumor cell lines have an extremely reduced ability to incorporate AuNPs while no difference was observed between the overnight and double dose (o/n + 3 h) treatment.

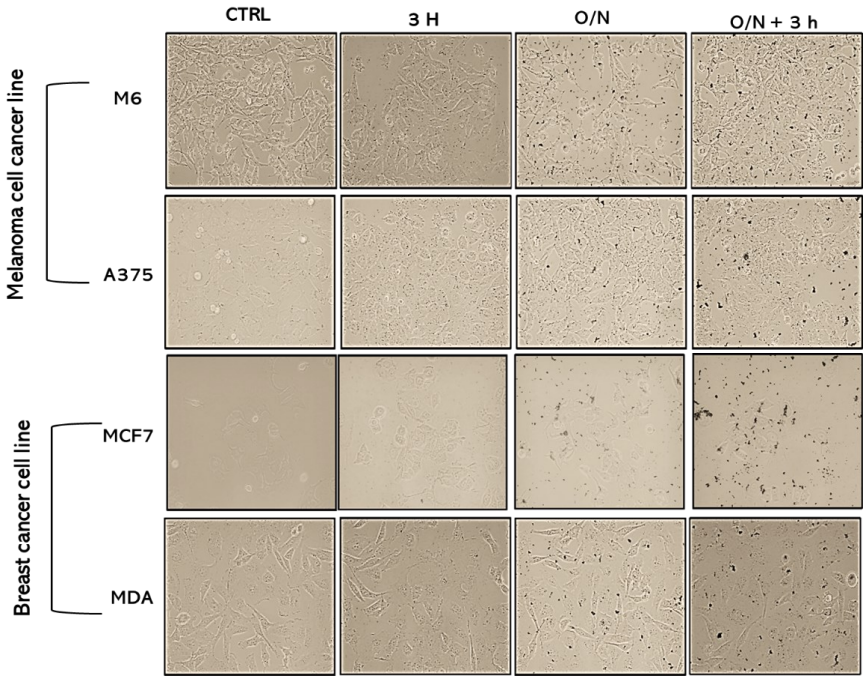

Figure 30: optical images of tumor cell AuNP (100 µM) uptake in tumor cancer cells after 3 hours, overnight, and double dose treatment(3h+o/n).

In parallel, we also conducted an analysis by Electronic Trasmission Microscope (TEM) to analyze the uptake of the AuNPs and their distribution inside the cells (fig. 31a). We also performed cell viability tests with trypan blue assay in order to evaluate the potential toxic effects (fig. 31b). Our results demonstrated no significant difference in cell viability between untreated cells (CTRL) AuNPs enriched cells at all the time points.

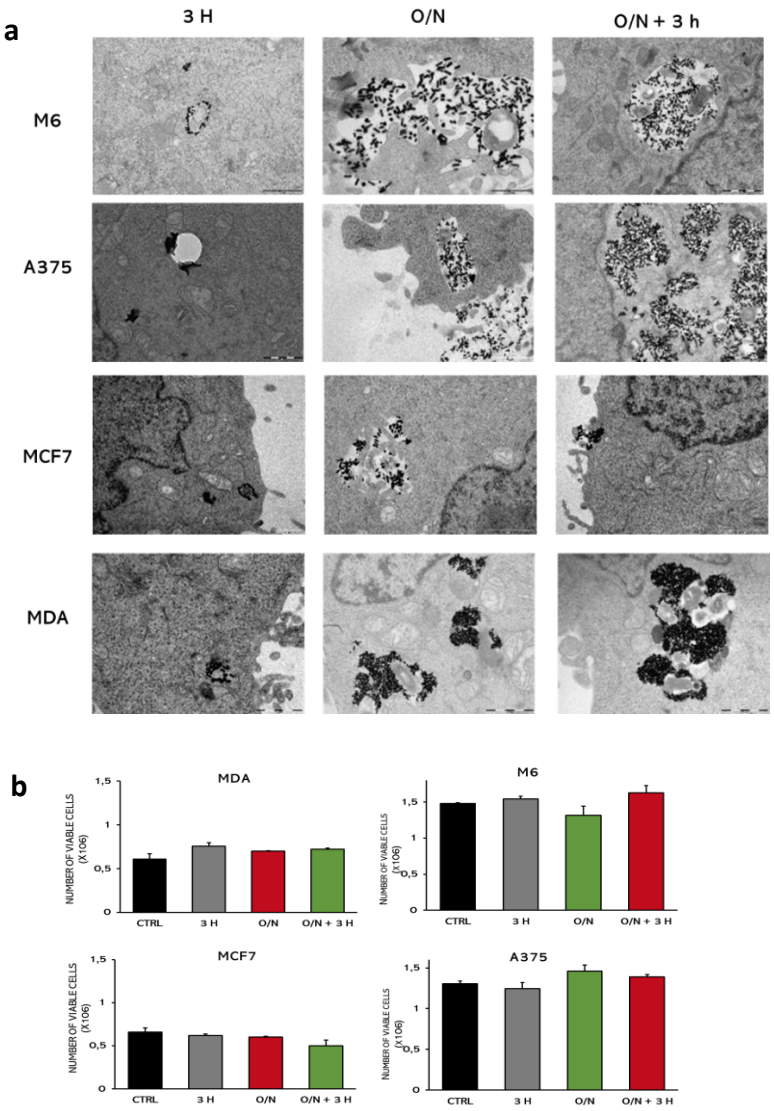

Figure 31: a) Trasmission elettron images of AuNP cellular uptake at all time points. The nanoparticles form rod-shaped aggregates within the cells. B) viability of the cells by trypan blu assay.

The optical properties of AuNPs in melanoma cells (A375 and M6) and breast cancer cells (MDA-MB 231 and MCF7) were determined by photoacoustic imaging. The absorption spectra of untreated and AuNPs loaded tumor cells were shown in figure 32:

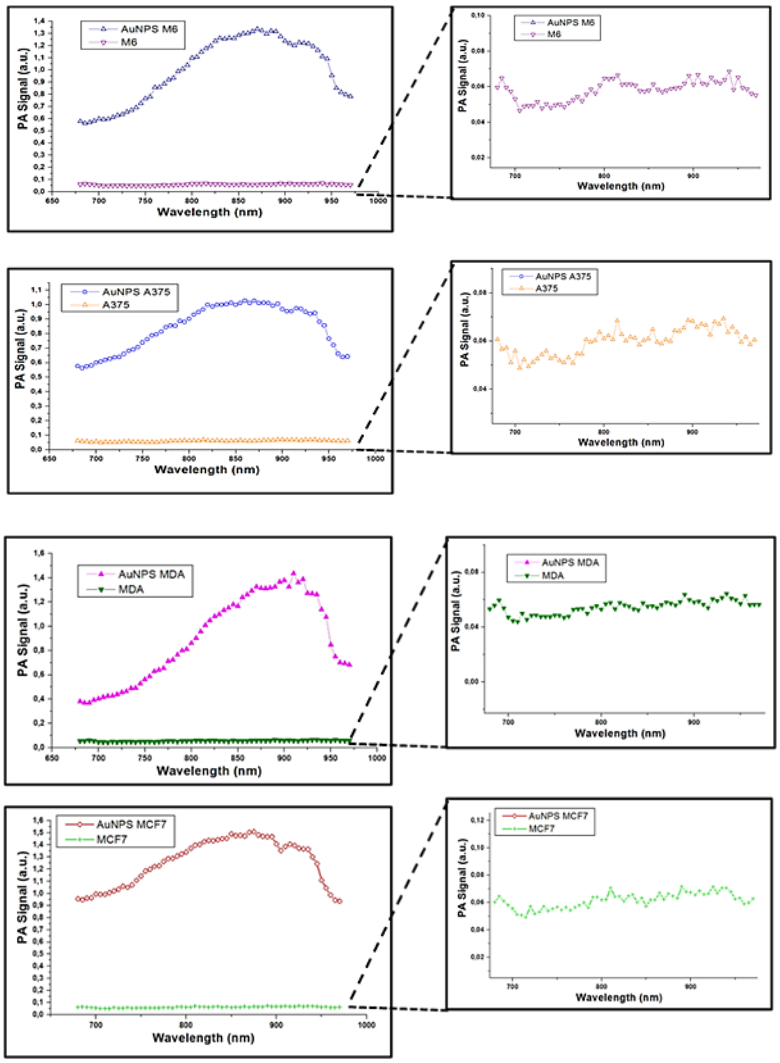

Figure 32: Multispectral photoacoustic signal acquired in MDA, MCF7, A375, M6 cell lines enriched with AuNPs. On the left the imaging signal given by the tumor cells treated with AuNPs and normalized with respect to their control on the right is shown the imaging signal given by the unloaded tumor cells.

Based on the comparable cellular amount of gold, that was quantified by ICP analysis (Figure 36a), between the two types of melanoma and breast cancer cell lines (fig.33), we performed the phototermic experiments with M6 for melanoma cell line, and MCF7 for breast cancer. Phothermal images of the two cell types loaded with AuNPs (overnight) and exposed to Near Infrared light (NIR) at 2.0 W CW intensity are reported in figure 28. The goal is to reach a temperature of 43°C, which is critical to cancer cells but still safe for healthy cells. The top panel shows the thermal images in false colour of the well containing the M6/MCF7 +AuNPs irradiated respectively at a) t=0''; b) t=01' and c)t=2'. The graph below shows the trend of the maximum temperature detected on the surface of the well as a function of the irradiation time. The data obtained demonstrate that both MCF7 and M6 loaded with AuNPs are able to reach moderate hyperthermia within 2:30 min

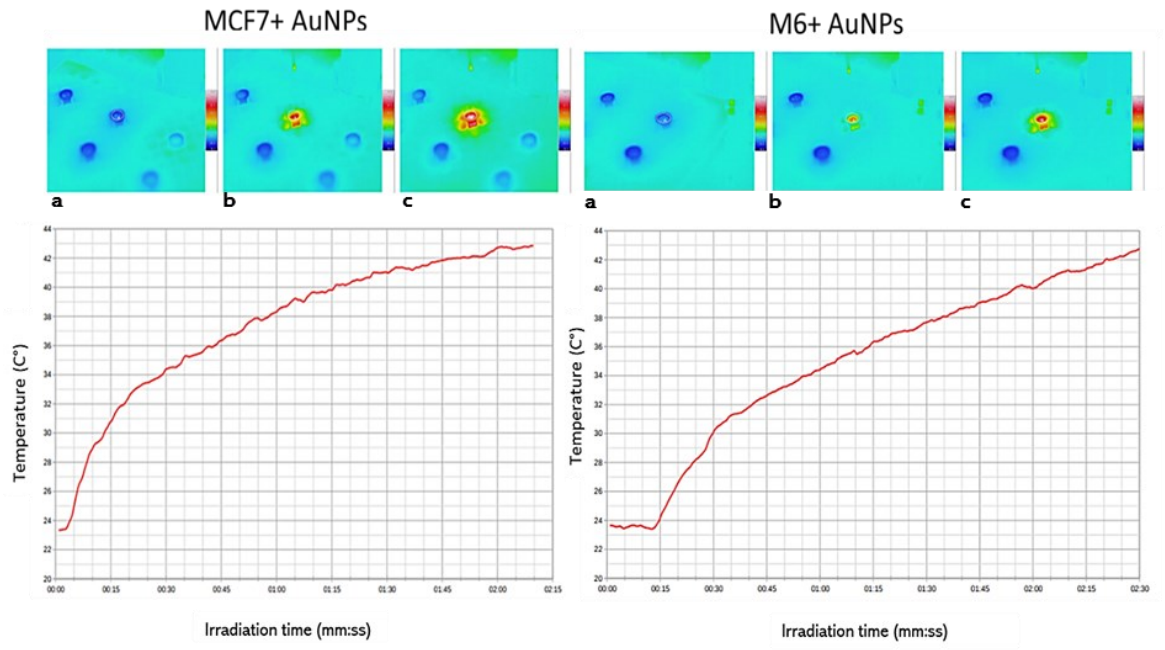

Figure 33: Thermal image in false colour of the irradiated well respectively at a) t = 00 ': 00 " b) t = 01': 02" and c) t= 02 ':00". In the graph, trend of the maximum temperature detected on the surface of the irradiated well as a function of the irradiation time.

Isolation and characterization of ECFCs

ECFCs have been isolated from the blood of 5 umbilical cords from 5 donors after obtaining informed consent. ECFCs were considered as EPC-derived colonies with a distinctive "cobblestone" look start to develop from adherent cell population after 14-21 days of culture (89). Human umbilical cord blood (UCB) ECFCs used showed a high proliferative potential and could be expanded to at least P8-12 without signs of senescence. The figure 34a shows the typical “cobblestone” endothelial appearance of the 5 isolated clones compared to mature endothelial cells Microvascular Endothelial Cells (MVEC) and figure 34b shows the results of flow cytometric analysis of a representative clone compared to flow cytometric analysis of MVEC. The analysis shows that ECFCs express, even though at a lower level, the endothelial markers(CD31 and Ulex), widely present on the cell membrane of mature endothelial cells while the characteristic markers of the endothelium lineage (CD31 and Ulex) while they lose the hallmarks of stemness (CD34 and CD133). Since there was no prior cell permeabilization in this flow cytometric analysis, vWF is unquestionably underestimated.

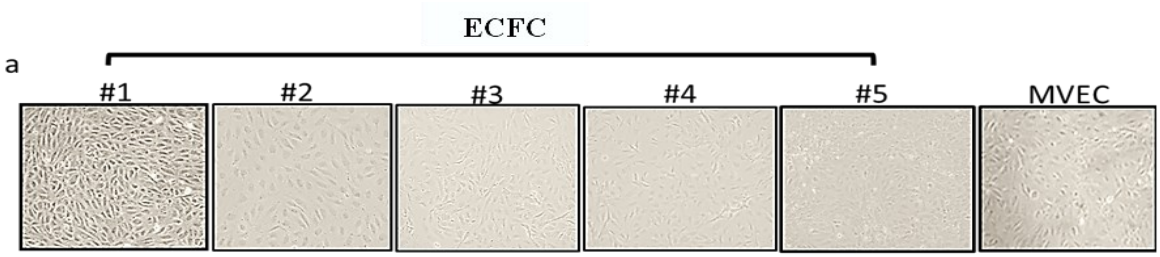

Table 2:

	CD34	CD133	CD14	CD31	KDR	vWF	CD87 R3	ULEX
ECFC	0,5	0	4	94,2	3,5	2,2	0,3	90
MVEC	0	0	0	100	7,1	6,7	18	100

Figure 34: a) Optical images of morphologic profile of ECFC colonies appeared after 2-3 weeks of culture. 1-5 morphology of 5 different clones isolated from umbilical cordon blood of 5 different donors, the last image represents the MVEC compared to ECFCs. Table 2: cell surface antigen expression.

Gold Nanorods uptake in ECFCs

To prove the translational value of ECFCs as cellular vehicle of AuNPs, we carried on uptake study on these cells. ECFCs were treated for 3h, overnight and with two sequentially dose of AuNPs (3h+overnight). Optical, TEM and ICP analysis were performed. Cell viability assays carried out in tandem with the uptake studies at different time points showed a moderate reduction of viable cells only after the double treatment (figure 35b). Optical images of AuNPs uptake by ECFCs is shown in the top row of figure 35a, while the TEM images are shown in bottom row. Based on the qualitative images of light and electronic microscope and on the quantification of gold by ICP analysis, we can determine that the incorporation of AuNPs after o/n treatment is greater than after 3 hours. The ECFCs treated overnight with 100 µM AuNPs also retain their biological characteristics, such as their capacity to form capillary-like structures and subsequently move (figure 35c).

Then we tested the thermal behaviour of AuNPs loaded ECFCs and untreated cells (CTRL). The figure 35d shows the thermal images in false colour of the well containing the ECFCs +AuNPs irradiated respectively at a) t=0''; b) t=01' and c) t=02' (Figure 35d). The graph below shows the trend of the maximum temperature detected on the surface of the well as a function of the irradiation time. The data obtained demonstrate that ECFCs loaded with AuNPs can achieve moderate hyperthermia within a few minutes. Obviously, laser exposure of unloaded ECFCs (ECFCs w/o AuNPs) was not able to induce an increase of cell temperature. Based on these promising results, we proceeded with the study of the photothermal properties of ECFCs in co-culture with tumor cells. To this aim, after overnight treatment AuNP loaded ECFCs were added to melanoma untreated cell culture (as reported in material method) and then exposed to the nominal optical power of 1.0 W.

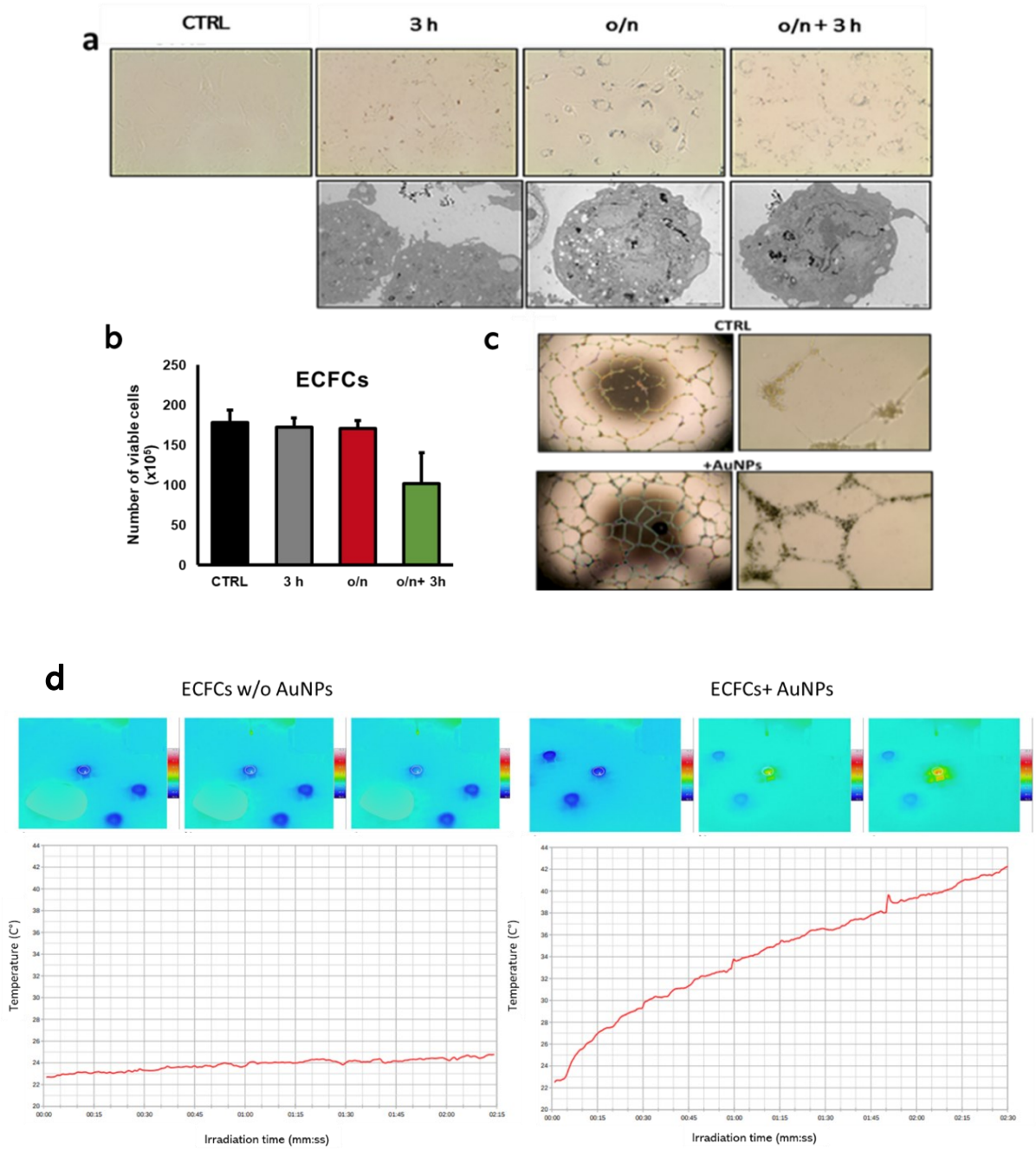

Figure 35: a) Optical microscopy images of ECFCs loaded with AuNPs at different time and doses (upper panel) or electron microscope images (lower panel) as the control did not contain AuNPs we did not analyse them by the electron microscope. b) Viability of the cells by trypan blu assay. c) optical microscope images of ECFCs after capillary morphogenesis assay which determines the vessel-forming capabilities of endothelial cells before and after treatment with nanoparticles. On the right, magnification of the optical images shows tubular like structures of ECFCs before (CTRL) and after treatment. d) Thermal image in false colour of the well irradiated respectively at a) t = 00 ': 00 " b) t = 01': 02" and c) t= 02 ':00". The graphs represent the trends of the maximum temperature detected on the surface of the irradiated well contaning control and AuNP loaded cells as a function of the irradiation time.

Comparison between ECFCs loaded with AUNPs versus melanoma and breast cancer cell line.

The quantification of the gold captured by the cells treated at different time points with AuNPs, by analysis with ICP-AES and reported in the graph below (fig.36a), demonstrated that the ECFCs are able to incorporate large quantities of gold compared to tumor lines already after 3 hours of treatment. The results of the ICP analysis also demonstrated that for ECFCs two consecutive treatments increase the amount of gold by almost two times compared to a single overnight (o/n) or 3h treatment, while for tumor lines the double treatment does not determine any significant increase. Based on these results, we chose the overnight treatment for the next experiments. Then we carried a comparative study on photoacoustic behavior of ECFCs and the tumor cell lines. Typical PA patterns are reported in Figure 36b, c, showing the spectral response in ECFCs loaded with AuNPs, and the multispectral response between ECFCs and tumor cells. In figure 36b the PA signal intensity shows the maximum intensity around 950 nm, in agreement with the plasmon absorption band position. (fig.36b). The PA signal provided by ECFCs-AuNPs exhibited a strong enhancement with respect to that associated to loaded tumor cells, without detectable spectra shift.

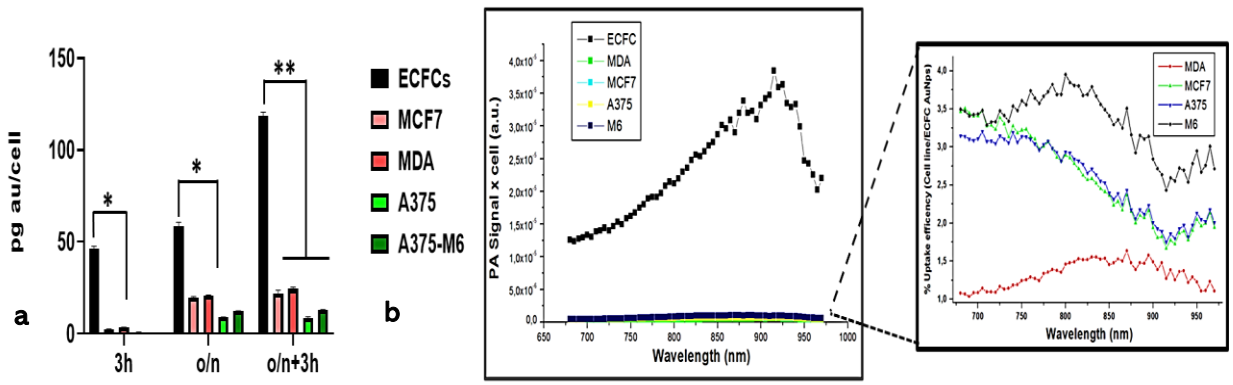

Figure 36: a) Time dependent uptake between tumor cells line and ECFCs was evaluated by inductively coupled plasma-atomic emission spectroscopy (ICP-AES). ECFCs incorporate at each time point a higher amount of gold compared to the tumor cell lines already in 3 hours treatment. b) PA spectral response of ECFCs loaded with AuNPs (black) and unloaded ECFCs (red). b) Plot of the PA spectral trend of ECFCs-AuNPs as compared to ECFCs unloaded AuNPs and tumor cells line treated with AuNPs. These graphs were obtained by normalizing and multiplying by 100 (%) the photoacoustic spectra of the MDA, MCF7, A375, M6 cell lines, with that of the ECFCs. The ECFCs' signal is 100fold higher than melanoma and breast cancer cells treated with AuNPs without detectable spectral shift. Significance was assessed by one-way ANOVA test followed by Newman– Keuls post-test. Error bars indicate mean ± SD; asterisk (*$p < 0.05$) indicates significant differences between ECFCs loaded with AuNPs and tumor cells line with single dose (3h or o/n), (**$p < 0.01$) indicates significant difference between ECFCs loaded with AuNPs and tumor cells line double of AuNPs.

Localization of ECFC in 3D co-culture by confocal microscopy

Consolidated that endothelial cell, thanks to their excellent tumor tropism and their ability to incorporate AuNPs, prove to be valid carriers for nanoparticles in the tumor site. To evaluate dose and time for optimal ECFC incorporation, before starting to conduct the in vivo experiments we developed a 3d model to evaluate the capability of ECFCs enriched AuNPs to reach and enter in M6 spheroids. For this purpose, $5x10^3$ A375-M6 (M6) cells were treated with 10^3 ECFCs unloaded or loaded with AuNPs (o/n). The M6-ECFCs spheroid co-culture optical images reported in figure 37a show the ratio between the two populations. Melanoma cells due to their melanocytic origin, as they grow as a compact mass at the centre with friable aggregate cells all around like a sort of crown. ECFCs penetrate the spheroide. Notably, ECFCs loaded with AuNPs, exert their antitumor activity by reducing the volume of the sphere, compared to control spheroids plated with unloaded ECFCs (Fig. 37a graphs). To facilitate the distinction of the two cell populations within the sphere, GFP stably transfected M6 cells were constructed by bacteria strain VB Ultrastable equipped with the plasmid GFP. ECFCs were stained with PHK26 (red; see materials and methods), consequently M6–ECFCs (loaded and unloaded) cells were observed under the confocal microscope one day and 5 days after ECFCs stratification on M6 spheroids. The images in figure 37b, show that AuNPs-loaded ECFCs are able to reach the spheroid core in 5 days, while the untreated ECFCs are able to migrate on the spheroid volume with lesser efficiency that AuNP enriched ECFCs (upper fig.37b). Besides, the PA signal provided from M6-ECFCs AuNPs inside spheroids exhibited a strong enhancement (Fig.37b).

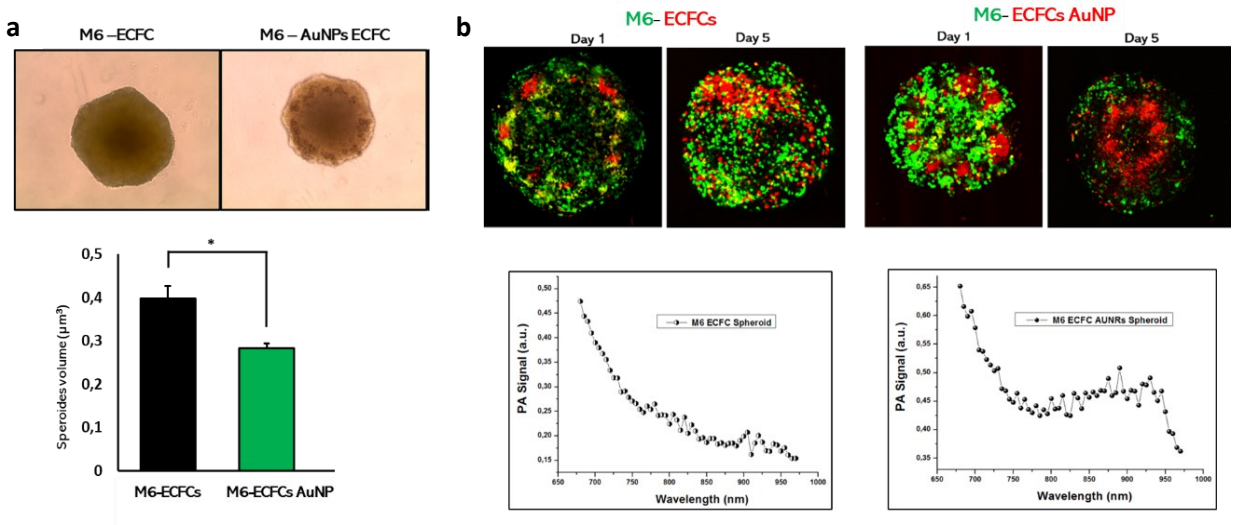

Figure 37: a) co-culture of M6 spheroids images with unloaded or AuNPs loaded ECFCs loaded or unloaded by optical microscope in upper row, in the bottom, volume calculation of the spheroids . b) In the upper panel confocal images, at 1 day and 5, of M6 spheroids (green) with ECFCs (red) loaded or not with AuNPs. In bottom panel, PAI signal of AuNPs loaded and unloaded ECFCs in spheroids and the relative spectrum. AuNPs loaded ECFCs' spectrum show a peak around 900 nm, which is not visible in un-loaded one. Significance was assessed by one-way ANOVA test followed by Newman– Keuls post-test. Error bars indicate mean ± SD; asterisk (*$p < 0.05$) indicates significant differences.

In vivo: tumor tropic properties of ECFCs in nude rats

To evaluate the ability of ECFCs to carry the AuNPs to the target site (the tumor mass), we performed a subcutaneous injection of $5x10^6$ M6 melanoma cells on both flanks of athymic female rats (NIH-Foxn1 rnu in heterozygosity). Following the development of a visible and palpable tumor mass, two sequential inoculations of $1x10^6$ ECFCs unloaded (CTRL) and $1x10^6$ ECFCs loaded with AuNPs (+AuNPs) were performed in the tail vein, 4 days apart (Fig. 38a). The presence of the loaded ECFCs was assessed by 3D- PA-ultrasound (US) visualizations and reconstruction and used to highlight AuNP distribution in tumor mass the day after the injection (fig.38a on right). The chemical/physical properties of the AuNPs translate in a molecular imaging signal (green) that is detected within the tumor mass, as shown in figure 38b, the ECFCs loaded with the AuNPs that are localized within the tumor mass, the ECFCs loaded with gold nanorods show a peak around 900nm (figure 38c).

Then, the rats were sacrificed and nanoparticle AuNPs biodistribution analysis were performed.

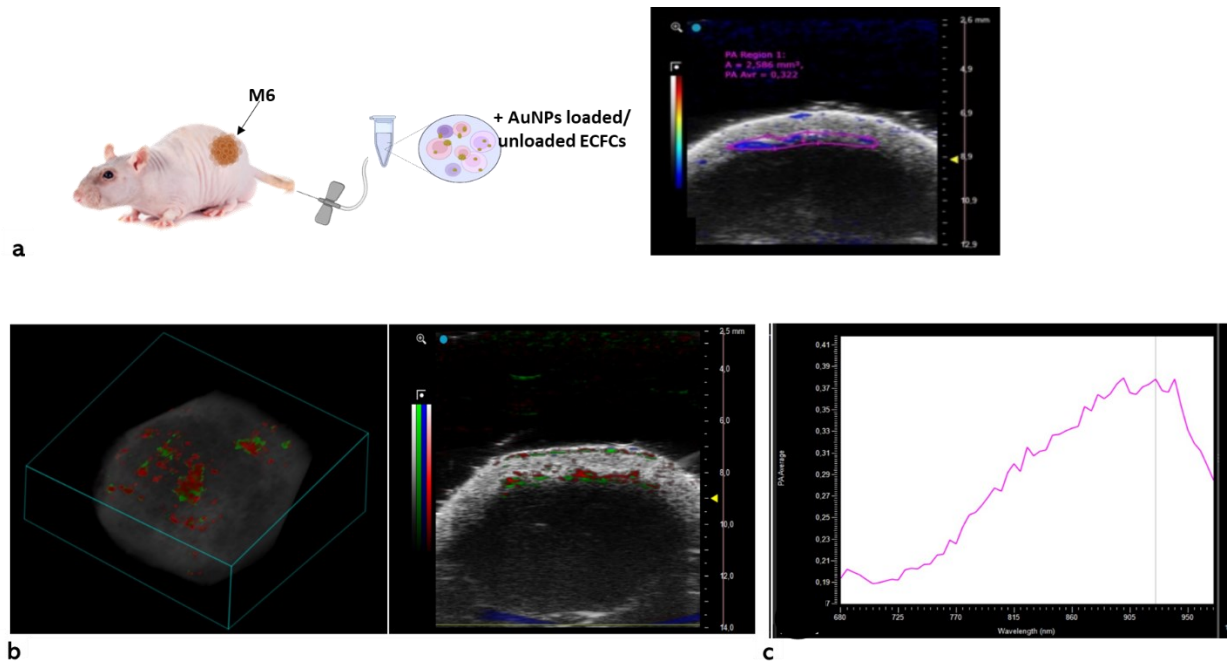

Figure 38: a) shows the experimental in vivo design: after one week of the induction of melanoma in nude rats (using $5x10^6$ M6 cells), ECFCs ($1x10^6$ cells) were injected in the caudal vein. Control rats received un-loaded ECFC whereas treated rat received AuNPs loaded ECFC, on the right 3D PA/US reconstruction of AuNPs in the tumor mass. b) The PAI signal (in green ECFCs AuNPs) is visible in the core of the spere. c) ECFCs-gold nanorods' PA signal spectrum: peak at 925nm.

The explanted masses and organs were then processed, and the presence of nanoparticles was evaluated by immuno-histochemical analysis with hematoxylin-eosin. The staining was performed both on control rats (inoculation of unloaded ECFCs) and on those treated with ECFC-AuNPs. From the results obtained and shown in Figure 39, it can be observed by optical images that ECFCs loaded with AuNPs massively reach the tumor site where they accumulate forming aggregates. Moreover, the histological analysis of all organs including the liver, spleen, and lung did not show any morphological alteration after administration of ECFCs-AuNP compared to organs of control rat treated with unloaded ECFCs (Figure 39). No evidence of atrophy, hyperplasia, necrosis, and fibrosis was observed with haematoxylin–eosin staining. These results confirmed that two injections of 100 µM AuNPs carried by $1x10^6$ ECFCs efficiently reached tumors and did not accumulate in the other organs. Therefore, ECFCs loaded with the gold nanorods effectively reach the tumor site managing to bypass the main reticuloendothelial system organs such as the liver and the spleen, where nanoparticles are reported to preferentially accumulate.

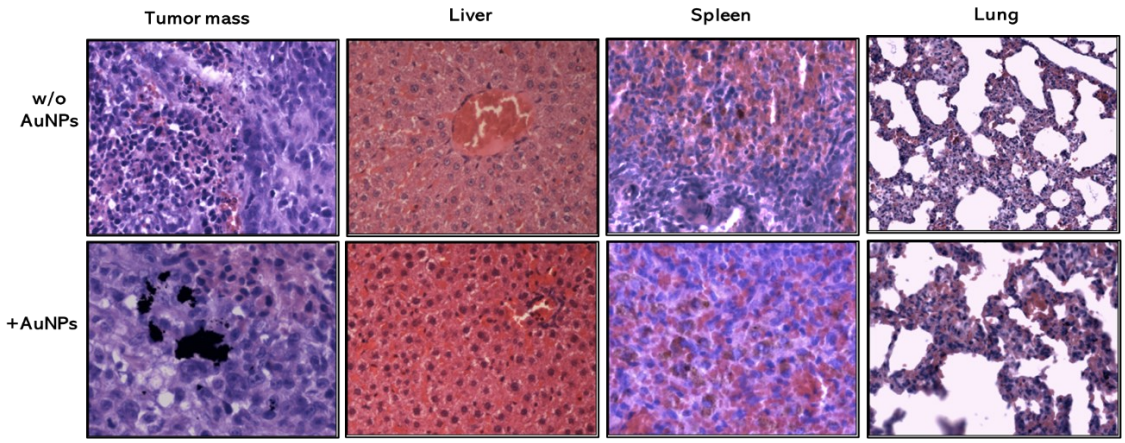

Figure 39: immunohistochemical analysis of tumor masses and organs from rats inoculated with unloaded and loaded ECFCs and then stained with hematoxylin and eosin. IHC. Moreover, Immunohistochemical analysis of the lungs show the presence of melanoma metastasis both in treated and untreated rats. No evidence of AuNPs accumulation were visible in the liver and the spleen of treated rats.

It is known, that ECFCs are able to reach the hypoxic areas of tumor masses, [120], [137]. In order to determine whether ECFCs loaded with AuNPs preserve this ability we evaluated by immunohistochemical analysis the simultaneous expression of HIF-1a (red) nuclear marker of hypoxia and CD31 (brown) specific marker of endothelial cells. As shown in figure 40a, a co-

localization of the expression of the two proteins is observed, demonstrating the ability of the ECFCs loaded with AuNPs to reach the hypoxic zones characteristic of the tumor mass.

Finally, by immunohistochemistry we evaluated the presence of proliferating nuclear antigen (PCNA), shown in red, which is expressed by cells in an active proliferative phase, the co-presence of endothelial cells is highlighted by the CD31 in brown (DAB reaction). Figure 40b shows a decrease in PCNA signal in the sample treated with AuNPs-ECFC (in brown), indicating a lower number of proliferating cells following inoculation into the tail vein of endothelial progenitors loaded with nanorods. This supports the thesis that treatment with ECFCs-AuNP induces a decrease in tumor proliferation, as already seen also in the treatment of spheroids.

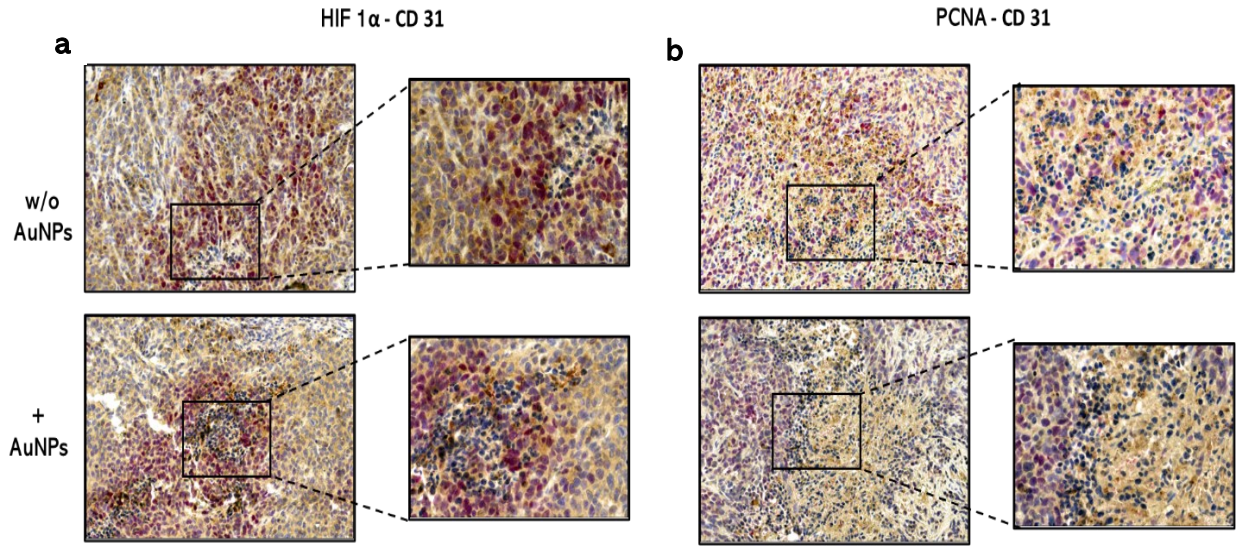

Figure 40: immunohistochemical images on tumor masses taken from rats. A) colocalization of HIF 1α expression (red) with CD31 (brown) comparing rat treated with unloaded ECFCs (top row) versus ECFCs-AuNP. On the right, magnification images. b) colocalization of PCNA (red) and CD 31 (brown). In the tumor mass of rats treated with loaded ECFCs (bottom row) we note a decrease in PCNA expression.

Dose-dependent effects of increasing doses of radiotherapy on tumor cell survival

In order to evaluate which radiotherapy dose could be selected for the combo treatment, the two metastatic melanoma cell lines (M6 and A375) and the two breast cancer cell lines (MDA MB 231 and MCF7) were exposed to different doses of ionizing radiation (IR) to 2, 4 and 6 Gy, and mock irradiation was used as a control (CTRL). At the end of the irradiation, the long-term cytostatic/cytotoxic effect was evaluated by clonogenic assay. This method allows us to determine the long-term effects of IR. Only a fraction of seeded cells retains the capacity to produce colonies. After 10 days of the treatment, colonies formed are counted to determine whether IR induced cytostatic effect. The results reported in figure 41 show that A375 and MCF7 were the most sensitive cell lines, with a significant cytostatic effect already after the lower dose exposure (2GY), and a dose dependent decrease of colony number. For A375-M6 and MDA-MB231, we observed a decrease of the surviving fraction with the two higher doses.

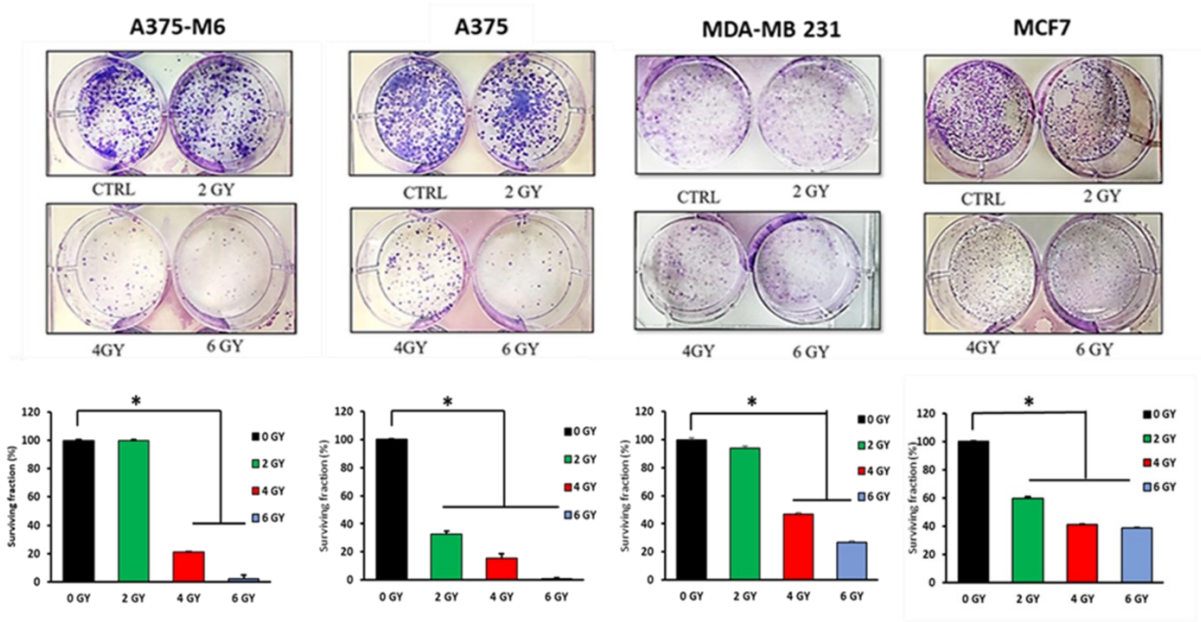

Figure 41: Melanoma cell lines (M6 and A375) and breast cancer cell lines (MDA and MCF7) were exposed to increasing radiation doses (2, 4, 6 GY), to evaluate the IR optimal for the combination therapy. In the upper panel, optical images of may Grunwald-giemsa stained colonies. In the bottom panel, histograms refer to the survival fraction for each cell type. Significance was assessed by one-way ANOVA test followed by Newman– Keuls post-test. Error bars indicate mean ± SD; asterisk (*$p < 0.05$) indicates significant differences.

Cytostatic and cytotoxic effect of combined radiotherapy-hyperthermia treatment on MCF7 (breast cancer), M6 (melanoma) and ECFCs:

Based on the results of irradiation experiments, we decided to focus our study on the most radioresistant cell line, A375-M6, with the aim to use hyperthermia to resensitize these cells and on the radiosensitive MCF-7 with the aim to use hyperthermia to enhance the effects of radiotherapy. Combo (hyperthermia and irradiation) and single treatment (hyperthermia or irradiation) were performed on M6 and MCF-7 monoculture and on M6/ and MCF-7-ECFCs co-culture (see experimental protocol in fig. 25 of material and methods). The cells, after being irradiated with 2Gy, were seeded to for the clonogenic assay and lysates for molecular investigations. The number of colonies formed of unloaded cells (w/o AuNPs) after irradiation with 2Gy does not differ significantly from the value obtained by irradiating the cells in the presence of AuNPs (fig. 42). It must be emphasized that for all cell lines there is a decrease in the number of colonies formed following irradiation, compared to the control (0 Gy). Moreover, we observed a shielding effect of the nanoparticles against radiotherapy in M6 cells and in ECFCs.

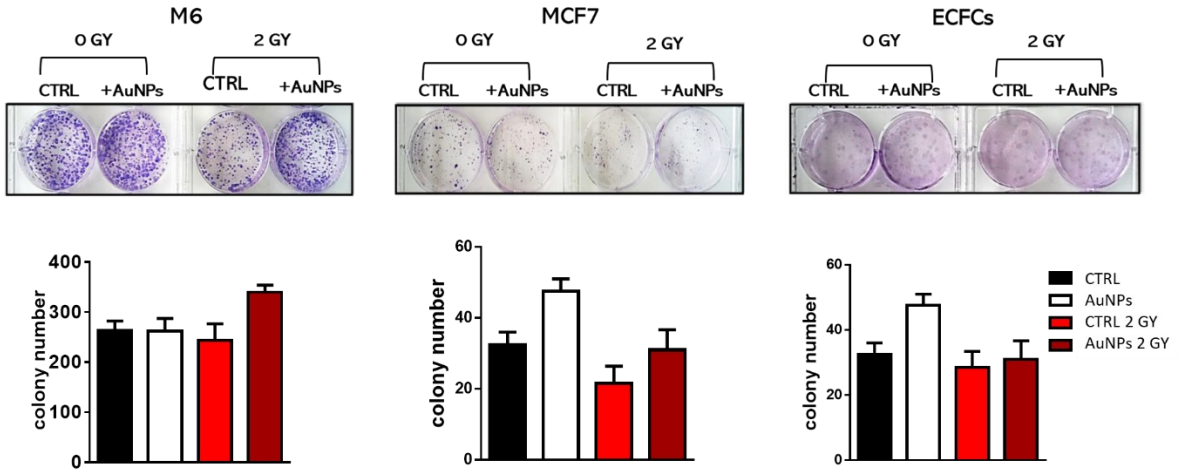

Figure 42: M6, MCF7 and ECFCs were exposed to Xray doses 2 Gy, to evaluate the effects of IR in cells treated with AuNPs. In the upper panel, optical images of may grunwald-giemsa stained colonies. In the bottom panel, histograms refer to the survival fraction for each cell type. Significance was assessed by one-way ANOVA test followed by Newman– Keuls post-test. Error bars indicate mean ± SD; asterisk (*p < 0.05) indicates significant differences between ECFCs loaded with AuNPs and tumor cells. Significance was assessed by one-way ANOVA test followed by Newman– Keuls post-test. Error bars indicate mean ± SD; asterisk (*p < 0.05) indicates significant differences between ECFCs loaded with AuNPs and tumor cells. Significance was assessed by one-way ANOVA test followed by Newman– Keuls post-test. Error bars indicate mean ± SD; asterisk (*p < 0.05) indicates significant differences.

So, established the X-ray dose and confirmed the concentration of AuNPs to be used for hyperthermia tests we proceed with the combo treatment. To evaluate the extent of the cellular damage induced by the application of the combined therapy, western blots were performed on the protein lysates of M6, MCF7, and ECFCs cell lines. Specifically, the expression level of Poly ADP ribose polymerase (PARP), enzyme involved in the repair of single-stranded breaks of the DNA (SSB) and in apoptosis. PARP activation consists of an immediate cellular response to metabolic damage. It is believed that this inactivation is spontaneous in the presence of extensive damage to the DNA. Indeed, in such cases more ATP would be required than is available to repair damaged DNA; the depletion of ATP in the cell leads to apoptosis [59], [153]. The other marker that has been examined is γH_2AX. Phosphorylation of H_2AX is the first step in the recruitment and localization of DNA repair proteins. Several studies show that after irradiation or the use of cytotoxic agents, H_2AX is rapidly phosphorylated. The figure 43 shows the western blot analysis performed on the M6, MCF7 and ECFCs cell lines after AuNPs-mediated hyperthermia and radiotherapy (2Gy). The bands corresponding to the cleaved fragments of PARP are observed for the ECFCs subjected only to hyperthermia and more markedly, for ECFCs irradiated with 2 Gy and subsequently subjected to hyperthermia at 43°C (both CTRL and AuNPs).

Finally, the signal relating to γH_2AX is detected in correspondence with the irradiated samples that have undergone hyperthermia at 43°, both mediated by control AuNPs. The collected data were normalized by evaluating α-tubulin levels.

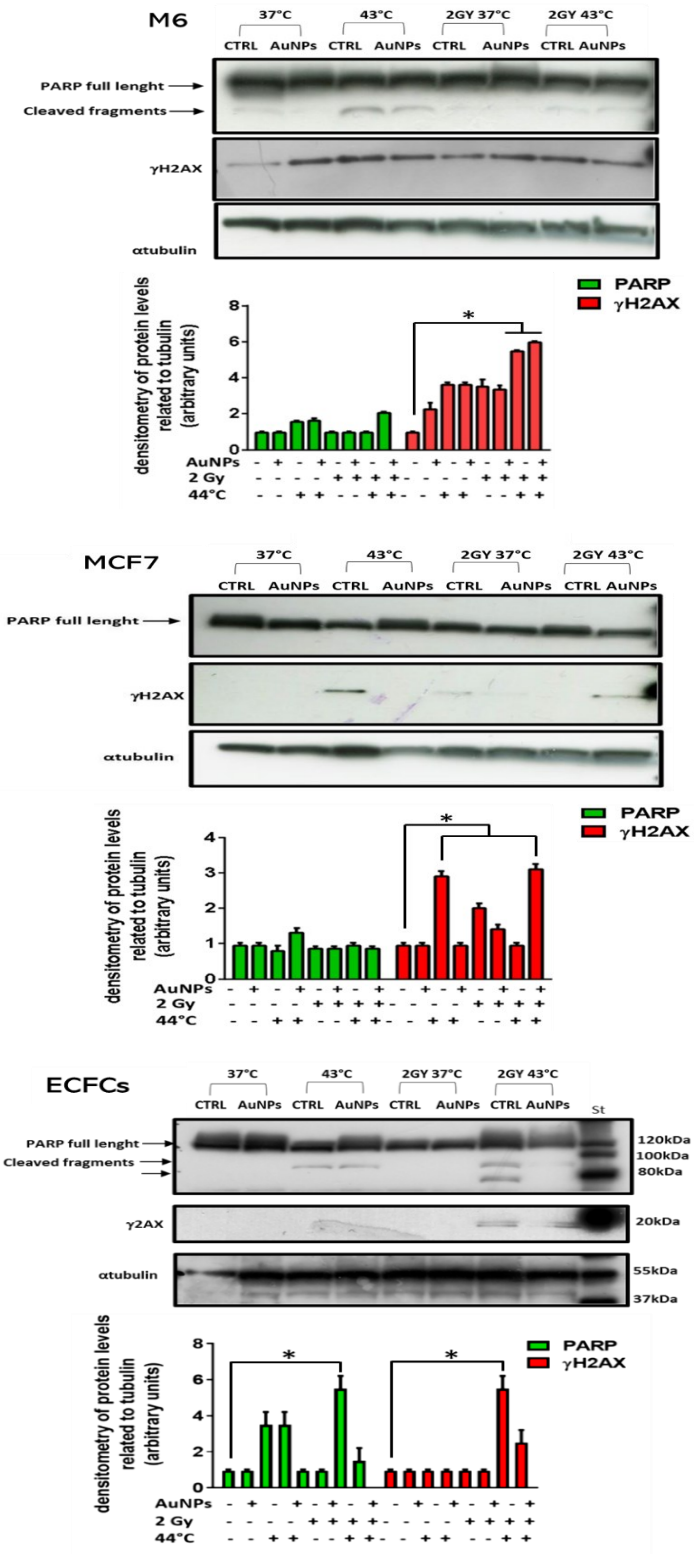

Figure 43: Western blotting analysis was performed on cell protein lysates in M6, MCF7 and ECFCs loaded and not with AuNPs and exposed to radiation dose of 2Gy and laser-induced hyperthermia, until the cells have reached the temperature of 43°C. Significance was assessed by one-way ANOVA test followed by Newman– Keuls post-test. Error bars indicate mean ± SD; asterisk (*$p < 0.05$) indicates significant differences. αtubulin. was used as a loading control.

Gold nanorod mediated hyperthermia effects in M6 monoculture and M6-ECFCs coculture after X-ray treatment

According to the experimental design exposed in figure 25, coculture of M6-ECFCs, and in parallel M6, were treated with 100 µM of AuNPs as shows in figure 44a, and subsequently exposed to irradiation 2Gy dose and hyperthermia (fig.44 b). The top panel in figure 44b shows thermal images of the M6 loaded with the gold nanorods, or ECFCs loaded with AuNPs in the coculture and exposed to Near Infrared light (NIR) at 1.0 W CW intensity respectively at a) t=0''; b) t=01' and t=2'. The graph below shows the trend of the maximum temperature detected on the surface of the well as a function of the irradiation time. The obtained data demonstrate the M6 loaded with the nanoparticles fail to reach the temperature of 43°C in fact after 2 minutes they hardly reach the temperature of 42°C (see dashed red line), while in presence of AuNPs-loaded ECFCs they reach 43 in about 3 minutes with exponential heating (see dashed red line). We demonstrated that the coculture convert light in heat more efficiently than monoculture thanks to the marked ability of ECFCs to incorporate large amounts of gold.

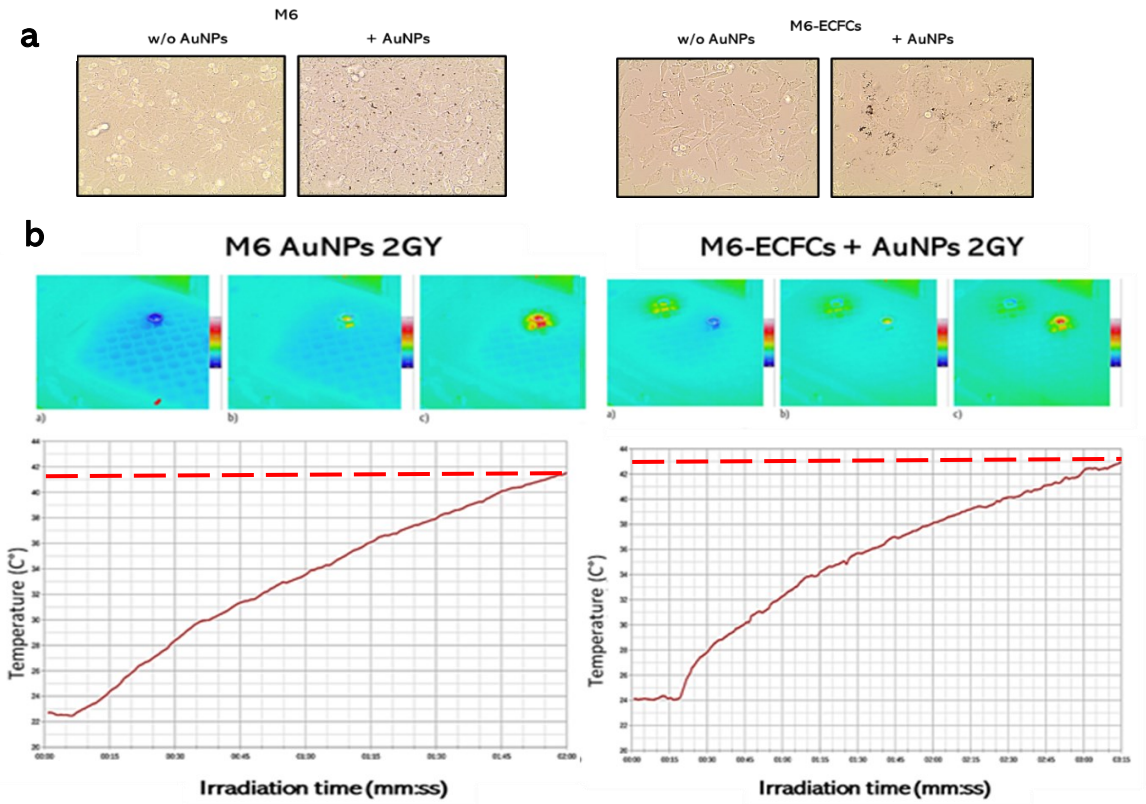

Figure 44: a) Optical microscopy images at 40x of M6 loaded or unloaded with AuNPs, M6-ECFCs and M6-ECFCs AuNPs coculture. B). Thermal image in false colour of the irradiated well respectively at a) t = 00 ': 00 " b) t = 01': 02" and c) t= 02 ':00". In the graph, trend of the maximum temperature detected on the surface of the irradiated well as a function of the irradiation time.

Evaluation of Cellular Damage in coculture exposed to the combo treatment

We assessed the short-term cytotoxicity considering the induced DNA damage in coculture in terms of strand breaks by comet assay and evaluation of histone γH2AX by western blot. The comet assay can identify in single cells the lesions resulting from a recent exposure, which occurred in the last few weeks, which are still repairable: such as single- and double-stranded DNA breaks Figure 46 shows a panel of images acquired during the scoring of the gels, the damage to the DNA is determined by evaluating the relative fluorescence intensity of the tail for its length of the single cell, a parameter used as an index of damage. Images reported in figure 46 a show that the DNA damage (% of DNA in tail) extent is higher after the combo treatment (xRay irradiation + NIR light exposure). However, we observed a statistically significant enhancement on the % of DNA in tail in co-culture AuNP-enriched ECFCs. The latter result was also confirmed by western blot analysis of the levels of γH2AX phosphorylation that also increased after the single treatments.

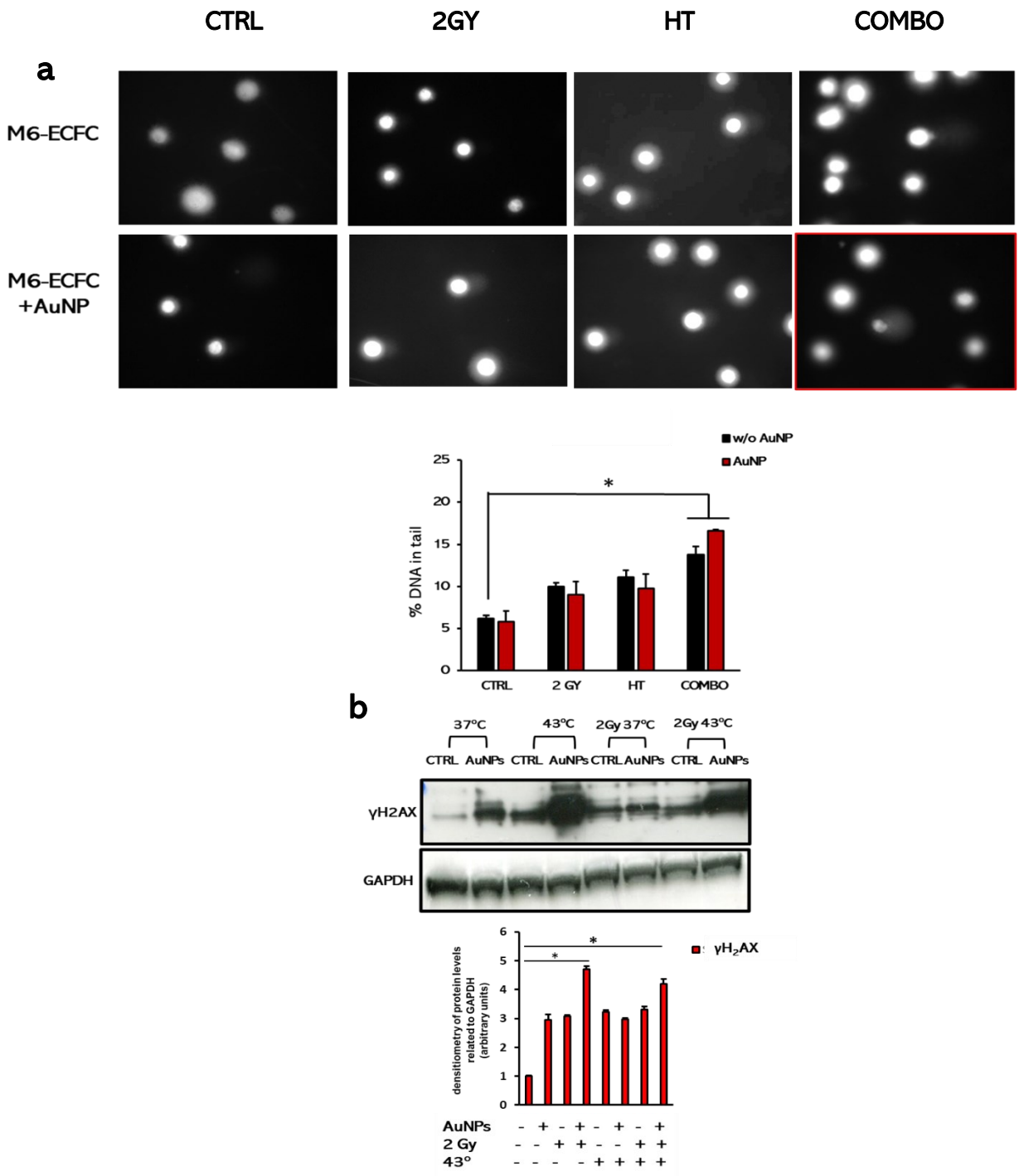

Figure 46: a) Representative images of comet morphology of M6-ECFCs after irradiation 2 Gy dose, hyperthermia, and Combo. First column shows non-damaged cells (CTRL), while in the last column more comets are visible in each cellular type. The graphs below indicate the levels of DNA damage, in terms of % of DNA in the tail. b) western blot analysis of γH2AX levels. Significance was assessed by one-way ANOVA test followed by Newman– Keuls post-test. Error bars indicate mean ± SD; asterisk (*p < 0.05) indicates significant differences levels. GAPDH was used as a loading control.

Gold nanorod mediated hyperthermia effects in MCF7 monoculture and MCF7-ECFCs coculture after X-ray treatment

We conducted the same experiments performed on M6 for MCF7 coculture. First, MCF7-ECFC were exposed to irradiation and 1h later to NIR exposure. Photothermal images of the MCF7 loaded with AuNPs after Xray radiation and MCF7- ECFCs loaded with AuNPs in the coculture and exposed to NIR at 1.0 W CW intensity are reported in figure 47. The top panel shows the thermal images in false colour of the well containing the MCF7+AuNPs and the coculture (after exposure to radiation 2 Gy) irradiated respectively at a) t=0''; b) t=01' and c) t=2'. The graph below shows the trend of the maximum temperature detected on the surface of the well as a function of the irradiation time. The obtained data demonstrate that MCF7 loaded with the AuNPs, irradiated, and then exposed to NIR light reach a temperature of 43° in few minutes (see dashed red line) while the MCF7 co-culture subjected to the same treatments reach a temperature of 43°C in about 10 seconds (see dashed line) . From the results obtained we can conclude that the effects of the photothermal study demonstrate that MCF7 enriched with AuNPs, compared to M6, respond better to heat exposure reaching a temperature of 43°C and more importantly that the MCF7/AuNPs-ECFCs coculture is more efficient to convert light in heat than AuNP loaded MCF7.

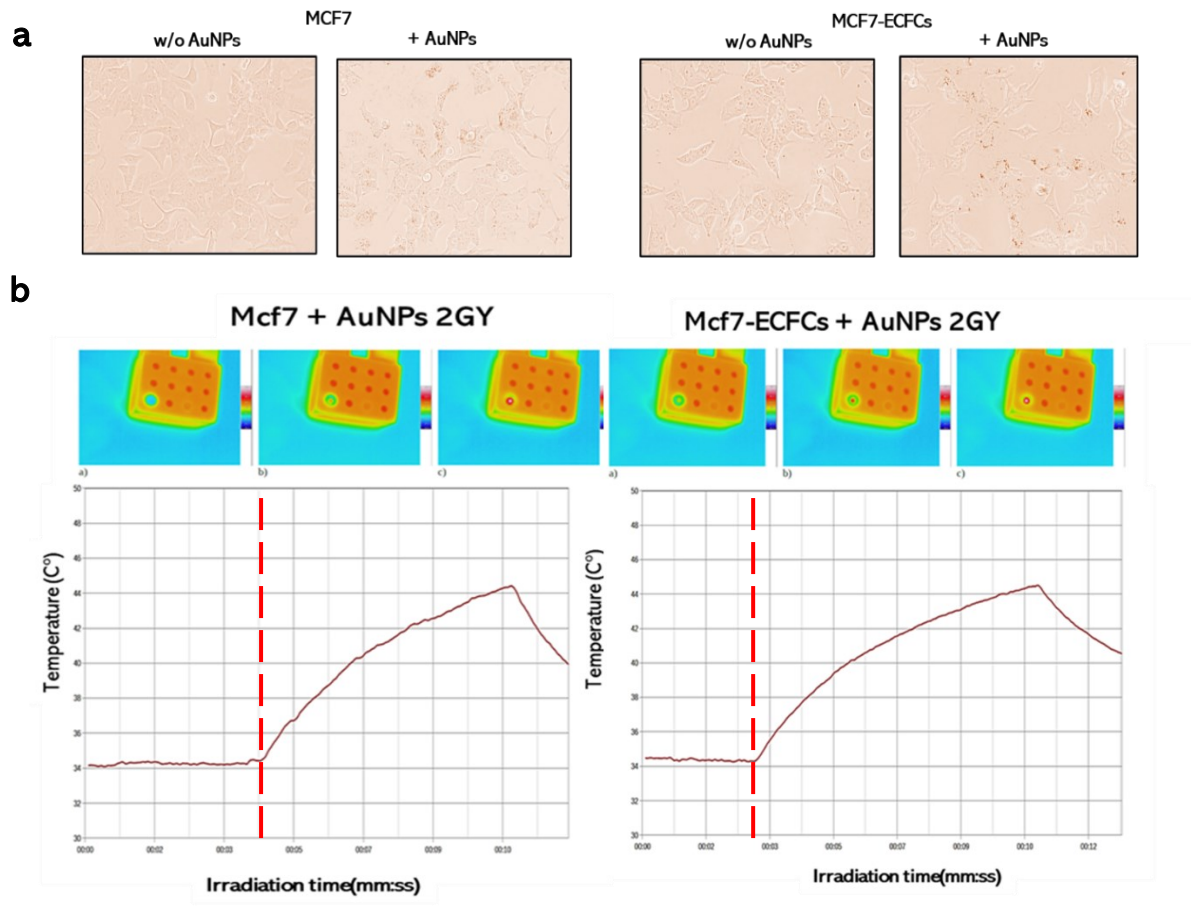

Figure 47: a) Optical microscopy images at 40x of M6 loaded or unloaded with AuNPs, M6-ECFCs and M6-ECFCs AuNPs coculture. B). Thermal image in false colour of the irradiated well respectively at a) t = 00 ': 00 " b) t = 01': 02" and c) t= 02 ':00". In the graph, trend of the maximum temperature detected on the surface of the irradiated well as a function of the irradiation time.

Evaluation of Cellular Damage in coculture exposed to the combo treatment

Considering the levels of DNA damage in terms of strand breaks by comet assay, it is possible to note a greater sensitivity of the MCF7-ECFCs cells to the stress caused by irradiation and hyperthermia after the combo treatment. DNA damage that causes the formation of comets in cells during electrophoresis, evident from the images acquired under a fluorescence microscope, in figure 48a, show the higher efficacy of the combo treatment compared to the single treatment. This result was also confirmed by the western blot analysis that shows the extremely high levels of H_2AX phosphorylation in MCF7-AuNP enriched ECFC after the double treatment (xRay+NIR light exposure (fig.48b).

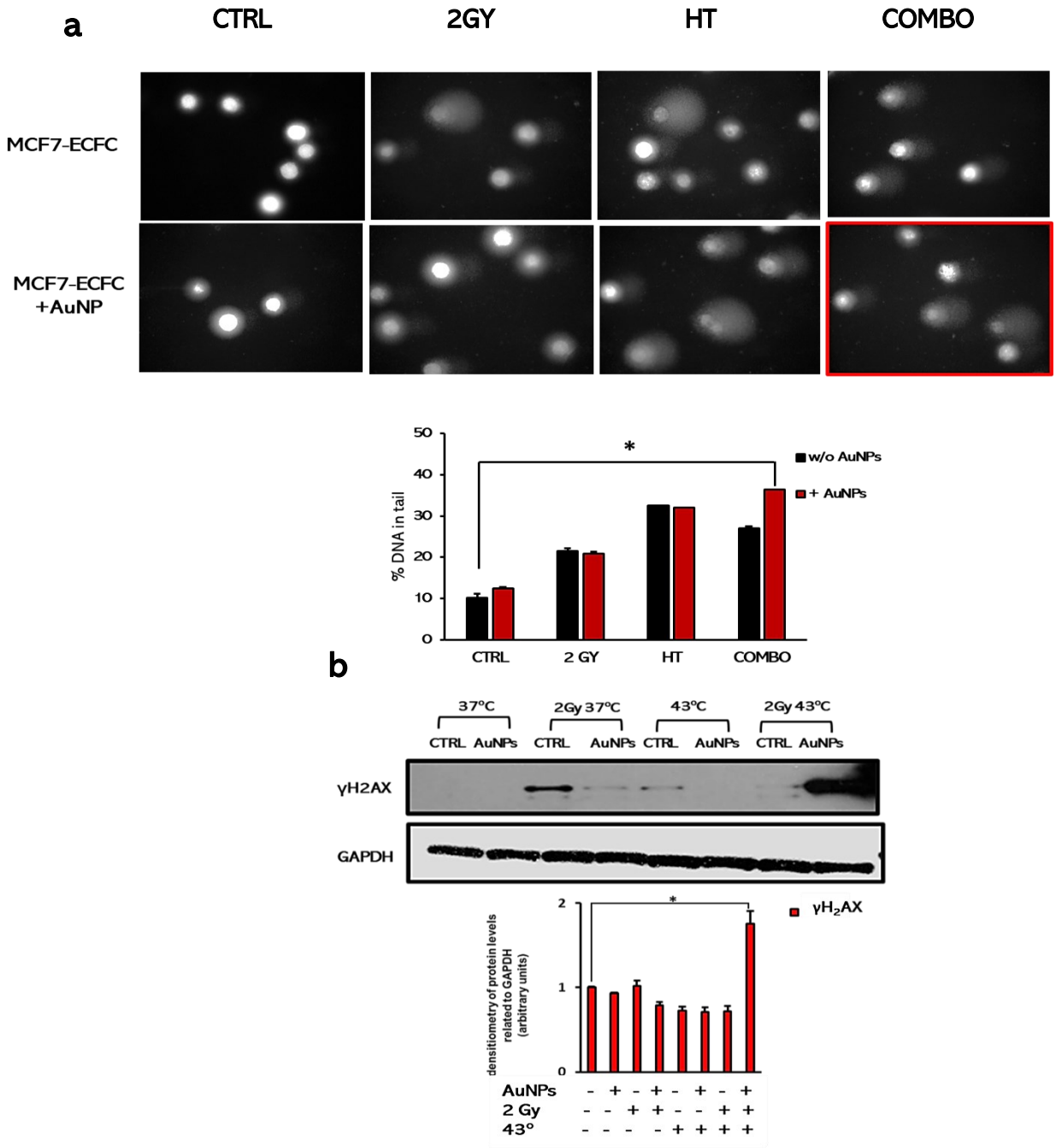

Figure 48: a) Representative images of comet morphology of M6-ECFCs after irradiation 2 Gy dose, hyperthermia, and Combo. First column shows non-damaged cells (CTRL), while in the last column more comets are visible in each cellular type. The graphs below indicate the levels of DNA damage, in terms of % of DNA in the tail. b) western blot analysis of γH2AX levels. Significance was assessed by one-way ANOVA test followed by Newman– Keuls post-test. Error bars indicate mean ± SD; asterisk (*p < 0.05) indicates significant differences GAPDH was used as a loading control.

Results- second part

In the second part of this thesis work, thanks to the collaboration with the RESEARCH group at the Institute of Chemistry of Organometallic Compounds - C.N.R, coordinated by Prof Claudio Sangregorio we evaluated the use of the Fe_3O_4 nanoparticles (MNPs) for drug delivery, and the use of Au@Fe_3O_4 for photothermal therapy. I carried on the toxicity studies on cell cultures.

In order to achieve high magnetization and exceptional heat generating capabilities at their minimal concentration under low magnetic field amplitudes, MNPs with a unique flower-like shape were created. Afterwards, MNPs were successfully encapsulated in the PVCL-co-PAA copolymer utilising a modified method that did not need the use of a particular surfactant or cross-linker, resulting in extremely stable and productive smart multifunctional MNCs. Indeed, PVCL and PAA segments on the surface of MNPs provide double pH- and temperature-responsive interfaces, implying unparalleled control over drug delivery and release in the biological system. In order to tailor the copolymer LCST in the hyperthermia range, their relative ratio was correctly selected. We show that the generated MNCs are biocompatible and can be loaded with a high quantity of a cytotoxic drug, DOX, which was used as a model to evaluate the system's drug release kinetics at both physiological pH (7.4) and acidic pH (5.5), like that found in the tumour environment. More significantly, we demonstrate that the drug can be delivered on-demand by using an AMF with frequency and amplitude below the clinical application threshold. Tumor cell viability is significantly decreased as a result of this action and the endosomal compartment's acidic pH.

Cytotoxicity Investigation and Cellular Uptake in MNPs

The cytotoxic effects of smart magnetic nanocomposites (MNCs) (1.0, 0.6, and 0.1 mg mL^{-1} of Fe_3O_4 MNPs), free DOX (10.0, 5.0, and 1.0 mol L^{-1}), and DOX-MNCs (DOX = 10.0, 5.0, and 1.0 µmol L^{-1} at concentration of MNPs = 0.1 mg mL^{-1}over 6 h) were examined on A375 human melanoma cells using the WST-1 test as results in figure 49. In figure 49a an in vitro cytotoxicity test of MNCs revealed good cell viability (~94.0% and 90.0%, respectively) after 6 h of incubation with sample concentrations as high as 0.1 mg mL^{-1} and 0.6 mg mL^{-1}, supporting the MNCs' low toxicity and high biocompatibility. Nevertheless, after 6 hours, the MNCs' cell viability drastically decreased to 80.0% at the highest concentration (1.0 mg mL^{-1}). As shown in Figure 49b, in the DOX concentration range of 1.0-10.0 µmol mL^{-1}, the anticancer activity of the DOX-MNCs (viability 86.0%, 66.0%, and 60.0%) is lower than that of free DOX, especially at higher doses, because in

the absence of external stimuli (AMF), free DOX diffusion is much quicker than DOX release from the smart MNCs, which is only triggered by the acidic pH of the tumor compartment; therefore, these data demonstrate that without applying exogenous stimuli, DOX-MNCs have lower toxicity with respect to free DOX, verifying that the drug is actually encapsulated in the stimuli-responsive copolymer.

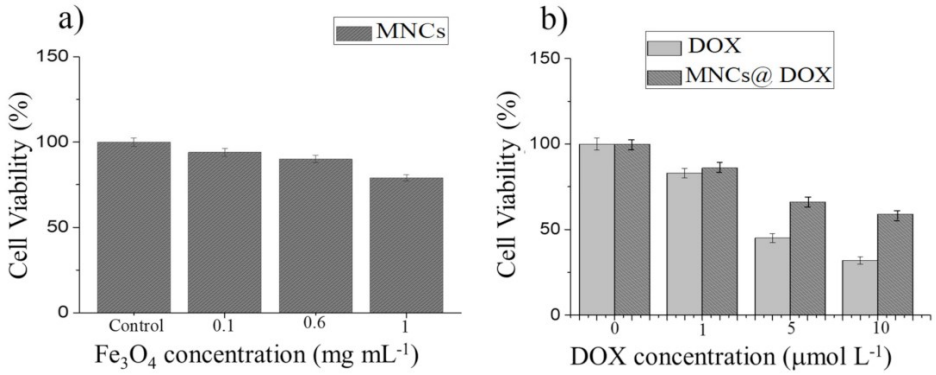

Figure 49: (a) Relative cell viabilities of A375 human melanoma cells incubated with different concentrations of MNCs, (b) free DOX and DOX-MNCs during 6 h incubation.

Based on these results, we chose a DOX-MNC suspension with concentrations of 0.1 mg/mL^{-1} Fe_3O_4 and 1.0 µmol L^{-1} DOX for further investigations on the cellular uptake and efficacy of magnetic field-controlled release. The stability of this suspension and that achieved by suspending the drug unloaded MNCs at the same concentration, was assessed in DMEM supplemented with 10% or 20% FBS, by tracking the size development by DLS over a 48 h. No aggregation occurred over the time analysed, despite a little increase in average size seen at t = 0 (216 ±14 and 200 ±9 for MNC at 10% and 20% FBS, and 148 ±9 and 241 ±12 for DOX-MNC at 10% and 20% FBS, respectively). For this purpose, A375 human melanoma cells and MCF7 breast cancer cells were treated with a DOX-MNC solution for 6 hours at 37 °C, and the results were examined using fluorescence microscopy, allowing the DOX to be located as it emits green fluorescence when exposed to laser light. Comparing the MCF7-treated cells (figure 50b) to the A375 cells (Figure 50a), MCF7 show a brighter green fluorescence than the A375 cells (fig. 50a), indicating that conjugated MNPs are taken up more efficiently into the MCF7. It is also apparent that the fluorescence is concentrated in the cytoplasm, in accordance with the previous reports[154]

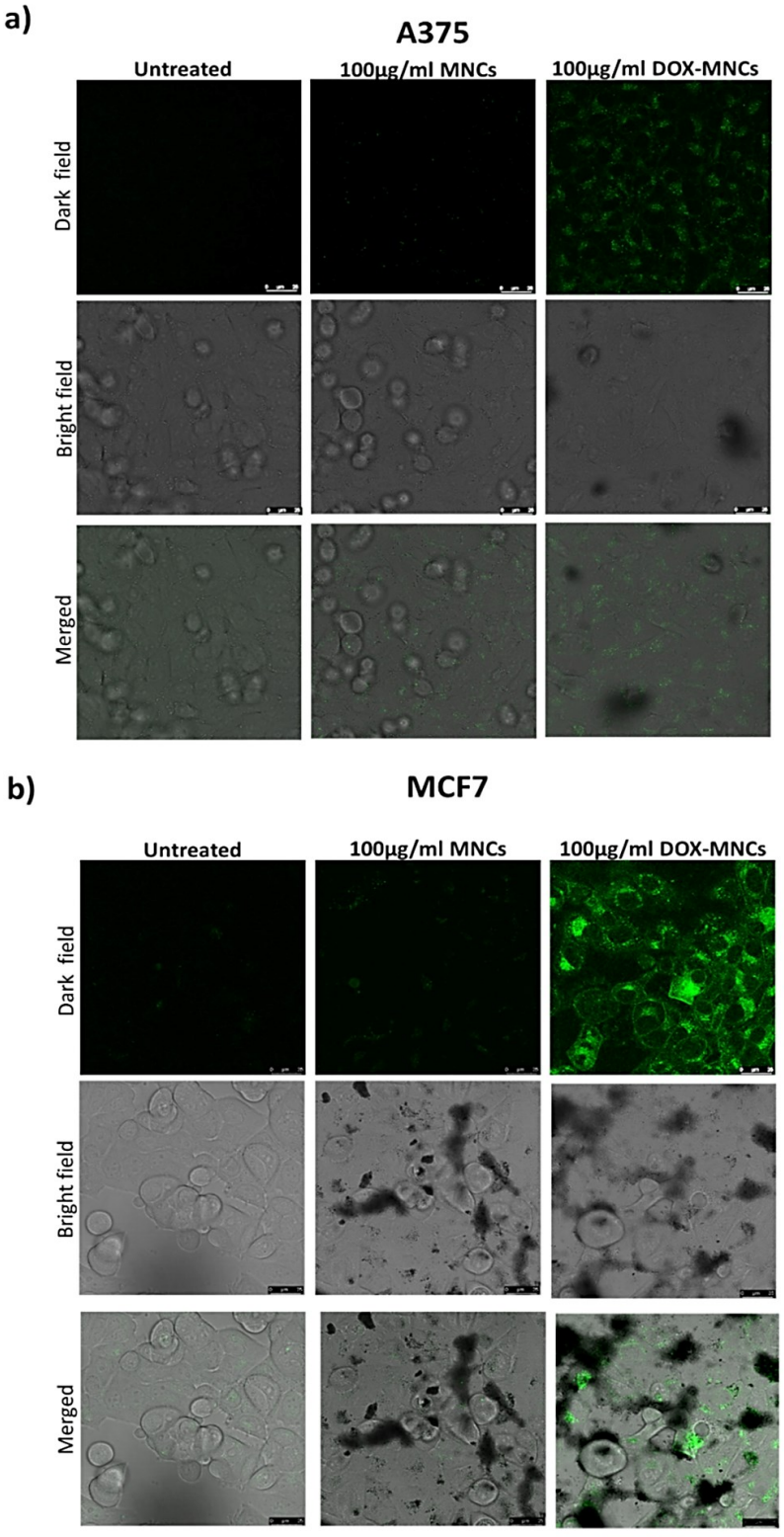

Figure 50: Confocal microscopy images of A375 melanoma (a) and MCF7 breast cancer cells (b) treated with vehicle (Control), MNCs, or DOX-MNCs for 6 h. The first row represents DOX fluorescent images, the second row the phase contrast microscopy images, and third row represent DOX overlay and merged images.

Then, before and after applying AMF to A375 and MCF7, we tested the in vitro cytotoxicity of unloaded and DOX-loaded MNCs (Figure 51). As previously described, following treatment with 0.1 mg/mL^{-1} Fe_3O_4 or DOX-MNCs (0.1 mg/mL^{-1} Fe_3O_4 and 1.0 µmol L^{-1} DOX) cells were exposed to the AMF for 24 hours. According to the findings shown in Figure 51a, c, unloaded MNCs are nontoxic in both cell lines and showed high biocompatibility, however following AMF stimulation, cell viability was slightly reduced. Regarding the therapeutic effectiveness of DOX-loaded MNCs, Figure 51c demonstrates that DOX-MNCs reduce MCF7 viability with a notable increase of cell death following AMF exposure due to the higher doxorubicin release rate. It should be observed that the MNCs carrying DOX had very modest impact on the viability of A375 cells (Figure 51a), indicating that they were incorporated into melanoma cells at a lower rate than MCF7 cells, as indicated in Figure 50a. In both cases, after exposure to AMF, cell viability was drastically decreased falling from 80% to 70% for A375 cells and 54% to 35% for MCF7 cells, respectively. These results demonstrate that the payload is continually released from MNCs, induced by the acidic pH of the endosomal compartment, and that the DOX release may be increased by the application of an AMF. Morphological study of cell cultures confirmed the biological effects of an unloaded and loaded nanoparticle before and after AMF stimulation (Figure 51b,d).

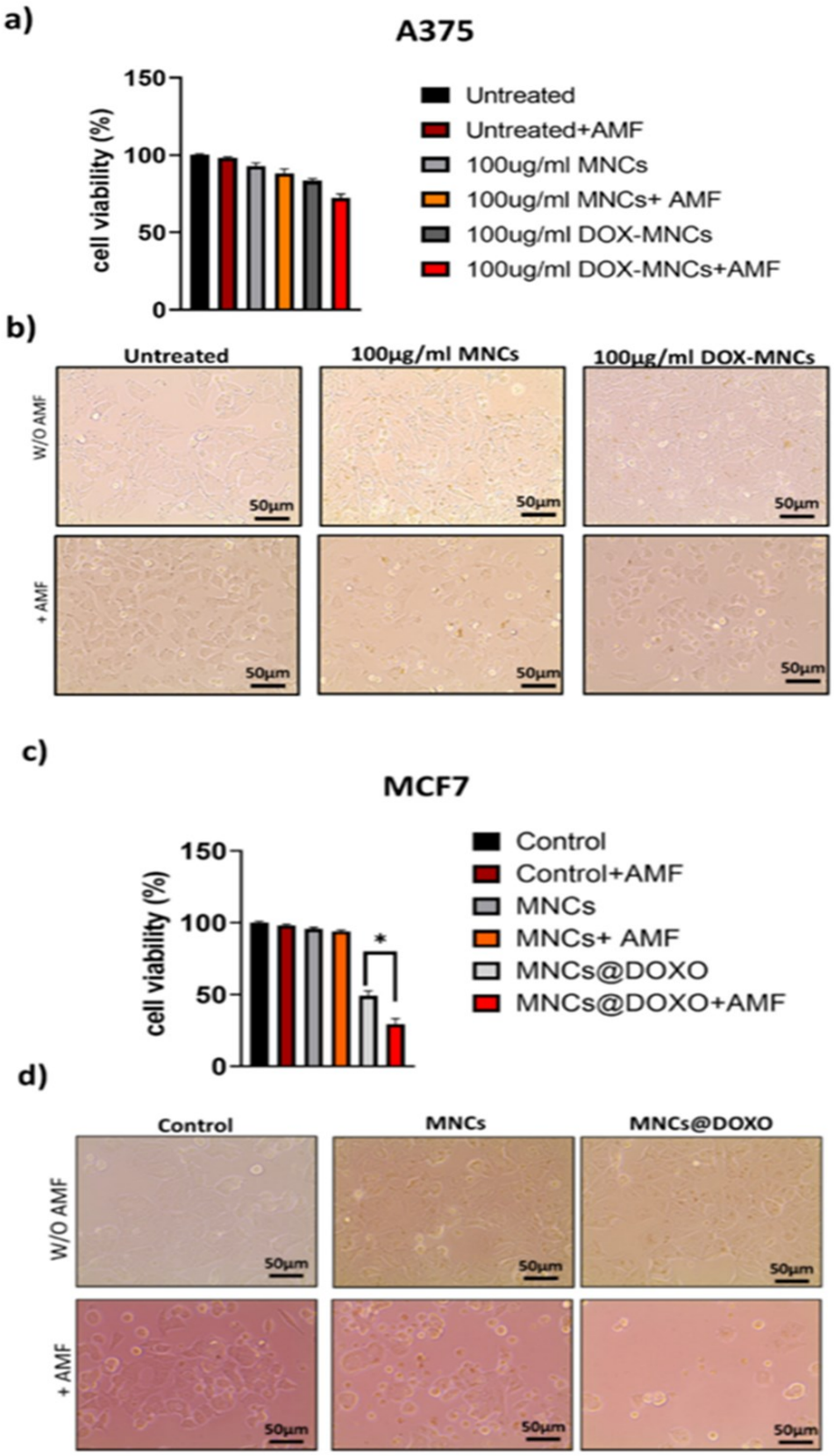

Figure 51: Relative cell viability and optical images of (a,b) A375 and (c,d) MCF7 cancer cells treated with vehicle (Control), MNC, or MNC@DOX for 24 h before and after AMF exposure. Error bars: mean ± SD. Statistical analysis was performed using one-way ANOVA followed by Newman–Keuls multiple comparison test. * $p \leq 0.05$.

Cytotoxicity Investigation and Cellular Uptake of Au@Fe_3O_4 nanostars

Here, we report the synthesis of a core shell Au@Fe_3O_4 magnetic-plasmonic-heterostructures with an unprecedented star-like morphology of average size of ca. 60 nm, comprising an Au core and a highly uniform Fe3O4 shell. The Au@Fe_3O_4 nanostars were synthesized by seeded-growth approach through thermal decomposition of metal precursors and were successfully transferred to water solution. A plasmonic resonance shifted toward NIR spectral region (640nm) was observed for the nanostars, which fits the first biologically transparent window, prompting their application in photothermal treatment and optical imaging.

Biocompatibility research was conducted on ECFCs, which are notable for their capacity to differentiate into mature endothelial cells, which line all blood vessels, before evaluating the biological potential of Au@Fe_3O_4 nanostars. ECFCs are an essential testing tool for all in vivo circulating nanodevices. The exposure of ECFCs to increasing concentrations of Au@Fe_3O_4 nanostar (10, 20, and 50 µg/mL) for 24 hours resulted in dose-dependent cellular uptake, as detected using a conventional optical microscope under white light exposure. Figure 52 clearly illustrates the internalised nanostar loads into ECFCs, which are visible as black spots inside the cells. As reported in Figure 52, we observed no statistically significant changes in the number of viable cells compared to control cells even at high concentration (up to 50 µg/mL), confirming the negligible toxicity and excellent biocompatibility of this nanodevice.

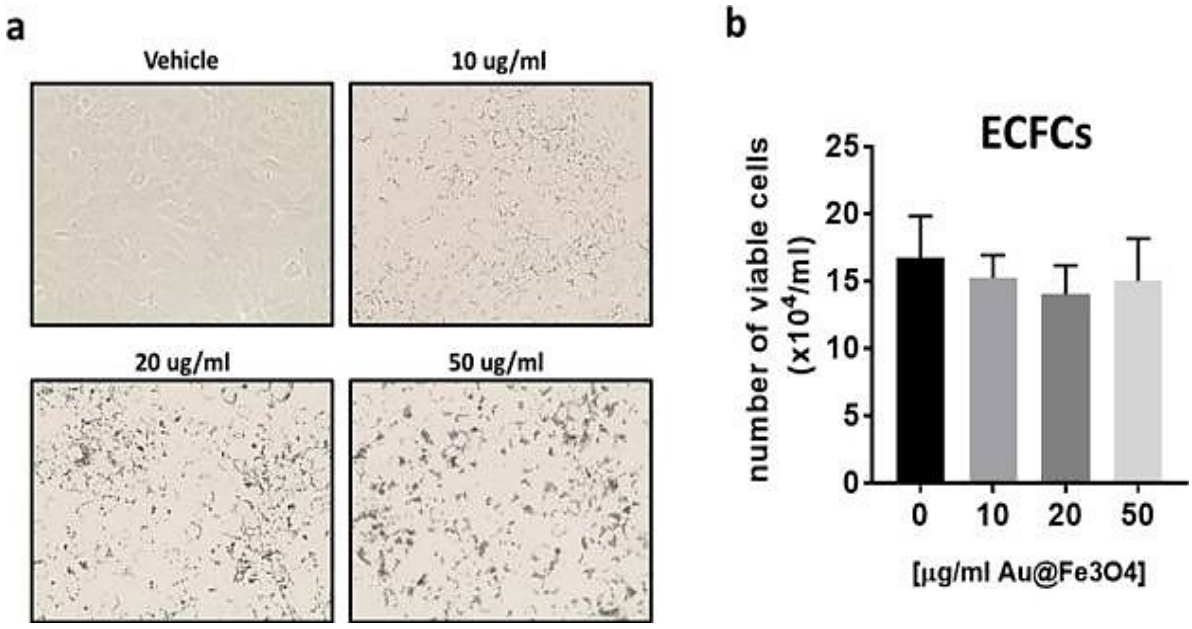

Figure 52: a) Representative bright field optical images of ECFCs treated with increasing dose of Au@Fe_3O_4 nanostars. (b) Cell viability assessed by trypan blue staining.

Then, we performed in vitro cytotoxicity studies on unloaded and loaded MCF7 tumour cells before and after AMF application or 658 nm light exposure to assess the magneto-mechanical stress and the photothermal impacts on cancer cells (Figure 53). Cells treated, as described above, with the highest dose (50 µg/mL) of Au@Fe3O4 for 24 h were able to uptake significant amount of metal nanostars, as shown by the bright field microscopy images in Figure 53a. Cells were then exposed to the AMF or light after the incorporation of the nanostar, as detailed in the material and methods. In both conditions, the cell viability was drastically decreased to 65% after AMF stimulation or to 45% after exposure to light (Figure 53b). The efficacy of the thermotransductive and magneto-mechanical potential of Au@Fe3O4 was also confirmed by morphological changes including cell shrinkage after AMF stimulation or light exposure (Figure 53a).

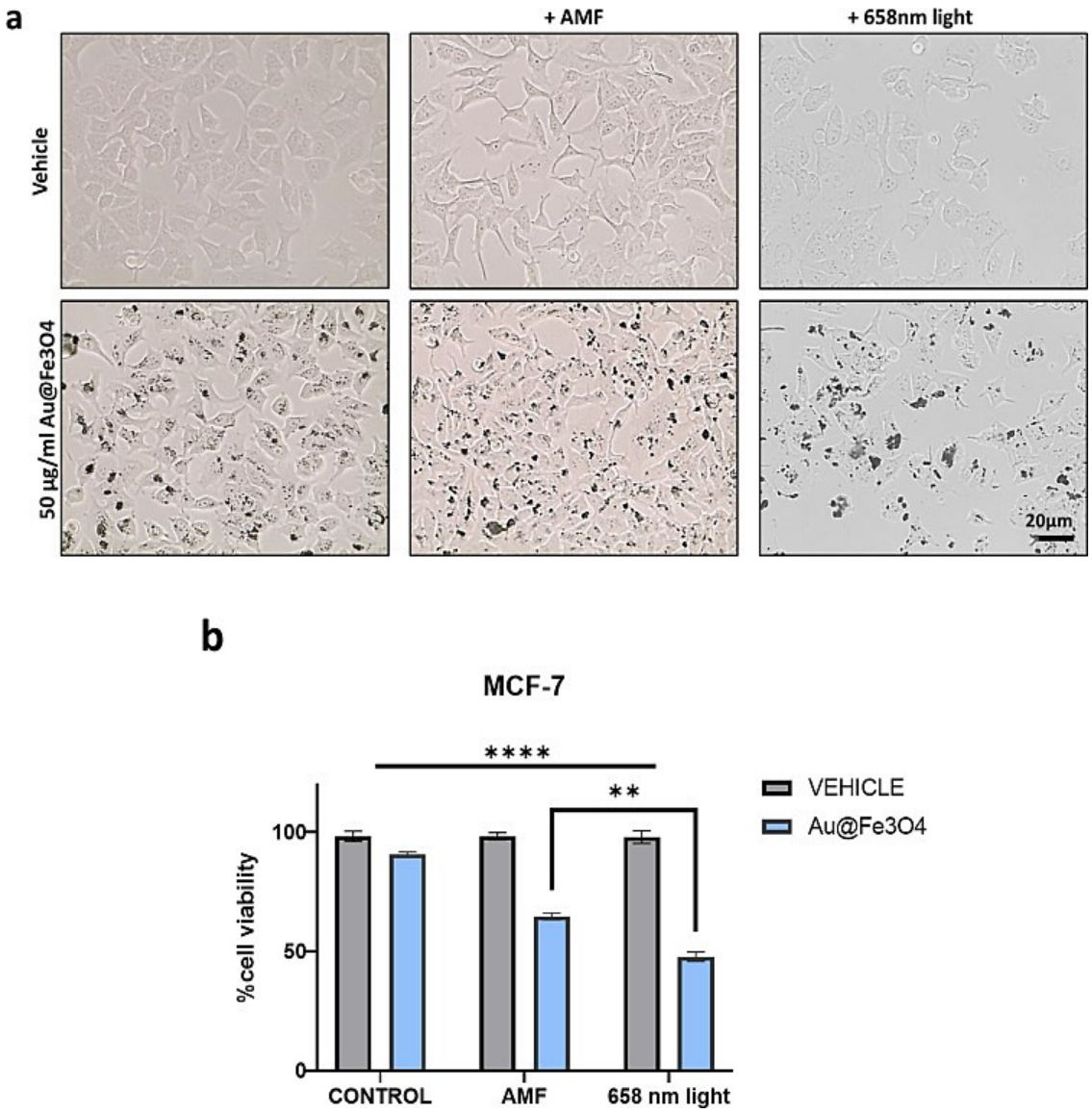

Figure 53: a) Representative bright field optical images of unloaded (upper images) and loaded (50 mg/mL) MCF7 tumor cells before and after exposition to the AMF or to 658 nm light. (b) Cell viability by trypan blue staining. **p < 0.01 indicates significant difference between Au@Fe3O4 nanostars loaded MCF7 exposed to AMF or 658 nm light; ****p < 0.0001 indicates significant difference between Au@Fe3O4 nanostar-loaded MCF7 before and after AMF or light treatment.

5. DISCUSSION

Nowadays, the incidence of cancer has continuously increased, both due to a global change in lifestyle and habits, and due to an increase in average life expectancy [2]. The growing importance that cancer has assumed in society has made it one of the main fields of investigation of biomedical research. In particular, the molecular structure of tumours, in its constant variations, symbolizes the field of research in which the greatest hopes for future clinical repercussions are placed [155]. Surgery, chemotherapy, and radiation are the most common treatments for cancer. As scientific research advances, many drugs have been developed to increase the effectiveness of treatment for different types of tumors. Radiotherapy uses high-energy radiation to destroy cancer cells and reduce tumors. Chemotherapy is used to slow the development of cancer cells, kill cancer cells, or prevent cancer cell reproduction.

The present project is focused on breast cancer and melanoma, two of the forms of cancer with the highest incidence. In the treatment of both tumors, when surgery is not feasible, the use of chemotherapy drugs or sometimes radiotherapy is used. These conventional approaches, although they are very valid, are not always decisive.

Currently, targeted therapy and immunotherapy are common treatments for many aggressive malignancies, such as metastatic melanoma or breast cancer. However, they, like earlier therapeutic methods, are not immune to the problem of innate and acquired resistance, which causes treatment failure in a significant number of patients [156]. Recently, preclinical studies have identified alternative treatments, in which the alliance between cell therapy and nanomedicine is exploited [157]. Nanomedicine, i.e., the use of nanometric-sized systems in the biomedical field which, in addition to being used for innovative therapies, can be exploited for early diagnosis and for the identification of predisposition to certain diseases. One of the strategies of nanomedicine for the treatment of cancer is plasmonic or magnetic hyperthermia which is based on the heating of nanoparticles by exposure to a light source of a precise wavelength (gold NPs) or by application of an alternating magnetic field (magnetic NPs). One of the main obstacles to the use of nanomedicine is linked to biodistribution, in fact more than 90% of the NPs injected in vivo accumulate in tissues and organs such as the liver, kidneys and spleen and less than 5% manage to reach the site tumor [158], thus not allowing an effective therapeutic treatment. To try to overcome this problem, the scientific population has thought of integrating nanomedicine with the use of cell therapy [159], [160]. Cellular therapies are among the so-called advanced therapies, in particular, in this project attention has been paid to ECFCs (Endothelial Colonies Forming Cells), a class of adult endothelial progenitor cells that have a high proliferative

potential and are able to generate populations of endothelial cells. Their main feature is the ability to home in tumor tissue.

The aim of this project has been to analyze how these two therapies, if combined, can overcome the main problems related to the biodistribution of nanoparticles and therefore to possible advantageous antitumor results. In our research laboratory it has been previously demonstrated that melanoma cells are able to recruit, in 18h, the endothelial progenitors, prepared from umbilical cord blood, through the CXCR4 system (expressed by ECFC cells) -SDF1 (produced by of melanoma and associated MSC)[120]. Based on these results, we evaluated whether ECFCs, once loaded with nanorods, rod-shaped gold nanoparticles with excellent biocompatibility, were able to maintain their ability to reach the tumor site.

We performed a comparative kinetic study to compare the AuNPs uptake capabilities of ECFCs and different tumor cell lines (MDA, MCF7, A375, M6) in vitro and in vivo. In vitro study, through to the ICP analysis, demonstrated that already after 3 h of treatment with AuNPs, the ECFCs are able to incorporate considerable quantities of gold, while the amount of gold accumulated by the tumor cells is almost zero. The most interesting results were seen following the overnight administration of AuNPs and giving the double dose (overnight + 3h), in this case the amount of gold incorporated by the ECFCs is much greater than that incorporated by the tumor cells, which appears to be comparable between the two treatments and less than four times compared to the gold detected within the ECFC. Moreover, the ICP analysis shows that the two melanoma lines integrate AuNPs with greater difficulty than the breast cancer cell lines. Further confirmation of the higher uptake of AuNPs by ECFCs compared to tumor lines was provided thanks to transmission electron microscopy (TEM) images, in which it is possible to evaluate the higher amount of AuNPs and the formation of nanoparticle clusters inside the ECFCs. We have also demonstrated that the PA signal provided from ECFCs loaded with AuNPs exhibited a stronger enhancement compared to tumor cells line, in fact, the ECFCs' signal is 100-fold higher than melanoma and breast cancer cells treated with AuNPs without detectable spectral shift.

Once these preliminary data were obtained, to evaluate dose and time for optimal ECFC incorporation, before starting to conduct the in vivo experiments we developed a 3d model to evaluate the capability of ECFCs enriched AuNPs to reach and enter in M6 spheroids. Distinctly, ECFCs loaded with AuNPs, exert their antitumor activity by reducing the volume of the sphere, compared to control spheroids plated with unloaded ECFC. Besides, the PA signal provided by

ECFCs-AuNPs inside spheroids exhibited a strong enhancement. So, 3D cultures confirm the cytostatic effect of ECFCs-AuNPs on tumor. Based on these results obtained in vitro, ECFCs can therefore be considered optimal cargo cells for the transport of nanoparticles. So, in order to evaluate whether the ability of ECFCs to reach the tumor site is maintained even after being loaded with AuNPs, in vivo experiments were performed. Nude rats were used for the experiment, previously inoculated subcutaneous tissue with melanoma cells. Once the following the development of the tumor mass, were treated with ECFCs. Endothelial progenitors loaded or unloaded with AuNPs were administered by two injections into the tail vein. The biodistribution of nanoparticles loaded by ECFCs were monitored by photoacoustic imaging, which demonstrated the homing of the nanoparticles to the tumor mass. The Immunohistochemical analysis, demonstrated 1) a great tumor-homing efficiency of ECFCs-AuNPs after a single intravenous administration and 2) their permanence inside the tumor masses after 1 week. These results confirm that melanoma cells are able to recruit ECFCs. Thanks to immunohistochemical analyses, it was possible to evaluate that there are no morphological alterations (compared to control rats) at the level of the organs analysed, such as liver, spleen, lung. Finally, it has been demonstrated that endothelial progenitors are able to reach hypoxic areas of the tumor mass. Through the immunohistochemical analysis for the expression of HIF-1α and CD31, it was possible to evaluate the co-localization of the two proteins.

The goal of my project is precisely to exploit the effectiveness ability of ECFCs loaded with AuNPs to reach hypoxic areas of the tumor mass, this could be exploited for radiotherapy and hyperthermic treatment in such areas, generally resistant to therapies as low oxygen levels do not allow the formation of reactive oxygen species (ROS), which represent the main mechanism of radiation-induced cell damage. Lastly, the immunohistochemical analysis performed on the tumor masses to analyse the presence of cells in an active proliferating phase, evaluating the expression levels of PCNA (proliferating cell nuclear antigen), allowed us to detect a reduction in the PCNA levels on the masses explanted from treated rats with ECFCs-AuNPs. This finding could indicate an anti-proliferative and therefore anti-tumor role of ECFCs loaded with AuNPs.

Finally, we focused on the evaluation of the in vitro effects of radiotherapy combined with AuNPs-mediated hyperthermia. Taking the two therapies individually into consideration, both are currently used for the treatment of cancer, albeit with some criticalities. Radiotherapy, despite being a consolidated approach, is associated with problems, such as the radiosensitivity of healthy tissues and the innate or acquired radioresistance of many tumours. Hyperthermia,

although not yet consolidated, provides promising results in the treatment of cancer, but still has some limitations related above all to the technical part of application. According to some recent studies, hyperthermia, when used in combination with radiotherapy, could be more effective [161]–[164]. For this purpose, the parameters such as the temperature, the doses, and frequency of the irradiation, with the goal of maximizing the therapeutic effect was determined.

In first instance, having the need to make this strategy selective, we exploit the use of nanomedicine for targeted tumor treatment. In particular, the use of nanoparticles allows to develop an *inside out* approach, which permits to obtain a more targeted action with respect to the conventional non-nano-mediated hyperthermia. In this respect, owing to their excellent biocompatibility and biological function, gold nanoparticles are the most suitable.

Long-term cytostatic studies by clonogenic assay were conducted to identify the ideal Xray radiation dose for melanoma and breast cancer cells. For this purpose, the tumor cells were subjected to increasing doses of irradiation (2, 4, 6 Gy). Consequently, since the administered radiation dose must be low to maintain toxicity in normal tissues within a tolerable level, 2 Gy was chosen. On melanoma (M6) and breast (MCF7) tumour cell lines, 2Gy radiation followed by AuNPs-mediated hyperthermia produced promising responses. Hyperthermia is responsible for the death of cancer cells, which unlike of healthy tissue are more sensitive to heat above 43°C. This greater sensitivity is mainly due to the different vascularization system of healthy cells compared to tumor cells. Healthy cells have well distributed and branched vessels and when subjected to temperatures higher than the physiological ones they are able to dissipate excess heat by means of vasodilation. On the other hand, malignant cells, characterized by inelastic and unevenly distributed blood vessels, are more incapable of dilating correctly and therefore of dissipating heat.

Molecular analysis intended to assess short-term cytotoxicity has shown that tumor cells subjected to this type of treatment are damaged and express high levels of markers such as PARP and γH2AX. Based on these data and the ECFCs were chosen to deliver the AuNPs to the tumor cells and used in co-culture experiments with M6 melanoma cells, and MCF7 breast cancer cells, which thermal transductive behaviour in the presence of nanoparticles was already known.

For the co-culture experiments (M6-ECFCs and MCF7-ECFCs) the chosen irradiation dose (2Gy) is in accordance with that of common radiotherapy. As already mentioned, exposure to ionizing radiation causes damage to various cellular components, mainly DNA, directly or indirectly

through the generation of free radicals. The experiments conducted on the selected cell models aimed at evaluating DNA damage in terms of strand breaks by comet assay and increase levels of H2AX phosphorylation, confirmed, as we hoped, an higher cellular stress induced by the combo treatment (Xray irradiation and NIR light exposure) to respective controls.

The collected data show also that the cytostatic/cytotoxic effect obtained from the combination of the two treatments is higher than that obtained from the single treatment. This result confirms that AuNPs are excellent radiosensitizers since they are characterized by a high absorption of X-rays. By producing a massive locally ionization in tumor tissues, it is possible to shorten the treatment time, reduce radiation doses and prevent the development of radio resistance. In doing so, the adverse reactions due to the absorption of radiation by healthy tissues and the radio-induced side effects also decrease. The use of AuNPs therefore allows to spatially focus the hyperthermic treatment by inducing targeted cell death, increasing the efficacy and selectivity of the therapy, and reducing the side effects on healthy tissues. Furthermore, the increase in temperature may attenuate the repair of DSBs caused by radiotherapy.

Combining these two approaches, significant results can be obtained for the treatment of cancer; radiation acts on well-oxygenated cells, located in the outermost part of the tumor mass, while hyperthermia, mediated by AuNPs, operates in the innermost part, where there is often a condition of hypoxia. This also determines an increase in the oxygenation level of the cells, thus making them more susceptible to the action of radiation. Looking at future applications, since AuNPs are capable of absorbing in the near infrared, the use of pulsed lasers or better of fiber optic lasers (equipped with greater penetration power, to treat even the deepest tumors), will allow to induce locally and selectively irreversible cellular damage to the tumor tissue without damage healthy cells.

Discussion second part

Regarding the data on the project carried out in collaboration with the CNR group:

The experimental work presented here was focused on the design of a novel smart magnetic nanocarrier, constituted by a nanometric Fe_3O_4 core encapsulated in a stimuli responsive polymeric shell (N-vinylcaprolactam-co-acrylic acid) release and localized magnetic hyperthermia for controlled drug delivery in combination with magnetic hyperthermia for cancer therapy and the synthesis of a Au@Fe3O4 core@shell system with a highly uniform unprecedented star-like shell morphology with combined plasmonic and magnetic properties to synergistically apply these two features: the heating induced by the simultaneous application of an AMF and laser irradiation can be combined, potentially increasing the efficiency of the magneto-photothermal treatments [165], [166].

To realize these goals, flower-like MNPs with an average diameter of ca. 16.4 nm, with high magnetization saturation, and very high heat generation capability, were prepared by the polyol approach, with good saturation magnetization and a high specific absorption rate. The MNPs were embedded in a dual pH- and temperature-responsive poly (N-vinylcaprolactam-coacrylic acid) obtaining magnetic nanocarriers that revealed reversible hydration/dehydration transition at the acidic condition and/or at temperatures above physiological body temperature, which can be triggered by magnetic hyperthermia. The efficacy of the system was proved by loading doxorubicin with very high encapsulation efficiency (>96.0%) at neutral ph.

The dual pH- and temperature-responsive nature of the MNCs led to an intense release of the drug at a mimicked acidic tumor compartment upon application of an AMF, while a negligible amount of drug was released at physiological pH and body temperature, verifying that the drug was efficiently retained in the MNCs' platforms and released in the response of exogenous/endogenous stimuli only. Moreover, drug release experiments when applying an on-off switchable AMF, showed that when the magnetic field is 'on', a controlled on-demand drug release occurred, while no release was observed when the AMF was switched 'off'. Thus, these promising results demonstrated that our smart MNCs can be employed as an 'on–off' drug delivery system that is able to increase the therapeutic efficacy and reduce adverse side effects of chemotherapeutics. Finally, the developed MNCs revealed low cytotoxicity (10% after 6 h of incubation at 0.1 mg mL^{-1} of Fe_3O_4 MNPs) and DOX internalization into melanoma cells and, more efficiently, in breast cancer cells. In addition, a significant viability reduction is observed as the result of the combined effect of AMF field application and of the acidic pH of the endosomal

compartment. We can thus conclude that these MNCs are effective tools for tumor therapy by controlled properties, including highly efficient magnetic hyperthermia and magnetothermally/ pH-controlled drug release at the right time and concentration by activation through external/internal stimuli.

Recently, have attracted more attention, the excellent optical and magnetic capabilities of iron-gold-based hybrid nanostructures, which come from the use of two different materials. For instance, magnetic and gold NP-based nanohybrids have mostly been used for gene and drug delivery applications [167], [168]. However, the synthesis of Au@iron oxide NPs with significant energy to heat conversion under both AMFs and NIR light has been described in only a few papers[169] Despite was demonstrated the biocompatibility of these hybrid platforms, still, did not demonstrate the efficacy of both the magnetic and plasmonic components in producing antitumoral. On these bases, the Au@Fe_3O_4 nanostars described in this study represent a step forward in the synthesis and development of hybrid nanostructures with a promising biomedical potential since they are easily taken up by cancer cells and exhibit very low cytotoxicity and great efficacy in vitro. Moreover, we wish to stress that typical laser powers used in photothermal treatments are generally within the range 2–20 W/cm^2, which is at least 1-order of magnitude higher than the one employed in our work, which makes our results very interesting in view of real applications.

Conclusion and future directions

The possibility of using the ECFCs loaded with gold nanoparticles allows to obtain numerous advantages:

First of all, umbilical cord blood (UCB) represents the most source of EPCs, with over 450.000 unrelated units banked worldwide and ready for clinical use. Nevertheless, CB-derived EPCs are tolerant and have a significant proliferative potential. The current study examines a specific subtype of CB-derived EPCs, the ECFCs, as a vehicle of AuNPs for a theranostic method intended for the thermoablative therapy of melanoma and breast cancer through the photoacoustic and tuneable thermic features of ECFC-AuNPs payload.

We demonstrated that ECFCs incorporate higher amounts of gold nanoparticle compared to other normal cells with innate tumor tropism (i.e. mesenchymal cells or macrophages) and also to tumor cells.

Furthermore, we demonstrated in vitro that AuNP-loaded ECFCs are able to generate higher photoacoustic signals than AuNPs alone or with respect to tumor cells loaded with AuNPs. After two injections into the rat tail vein, we used PA-US to show in vivo that AuNP-ECFCs had a high tumor-homing efficiency. Furthermore, our data demonstrated that 1 week after injection, AuNP-ECFCs preferentially aggregate inside the tumour masses.

The chemotactic gradient of SDF-1 released in the tumour microenvironment is the main cause of the tumour recruitment of AuNP-ECFCs [170]. Indeed, ECFCs have a high expression of CXCR4, the specific receptor for the chemokine SDF-1. The "temporary" passage of ECFCs in normal organs, followed by total clearance within a few days, is firmly justified by the fact that normal tissues release little or no SDF1. Finally, the healthy behaviour of animals and lack of histological damage, such as fibrosis and tissue inflammation, in all organs, including the liver, spleen, kidney, and lung, 1 week after injection, prove that AuNPs-ECFCs are safe and do not cause any indication of toxic effects. These data clearly support the use of ECFCs as a delivery system for nanoparticle-based diagnostic and therapeutic agents. The investigations on co-cultures spheroids, demonstrated that ECFC-loaded AuNPs were able to reach the spheroid core and more importantly were able to induce a spheroid volume reduction compared to unloaded ECFC, enveling an antitumoral activity *per se*.

The next step will consist in being able to isolate the ECFCs from the peripheral blood of cancer patients, which have a higher number of circulating ECFCs than that of healthy subjects. In the perspective of a clinical phase, the use of autologous ECFCs promises to be an effective

"personalized therapy" of cancer, with an almost absent risk of rejection. Collectively, the present research will be suitable for clinical use and easily supported by pharmaceutical companies equipped with cell culture facilities and synthesis of collodion at large scale.

Based on all the results obtained from in vitro and in vivo experiments, we can see that the union between cell therapy and nanomedicine could be used for innovative therapeutic strategies, in order to improve therapeutic efficacy. The prospective research of this thesis work foresees further biodistribution studies in order to optimize the experimental protocol, i.e., determine the number of ECFC injections necessary for the enrichment of the tumor mass with AuNPs for thermoablative treatment.

Regarding the multifunctional platforms developed in collaboration with Dr. Claudio Sangregorio team's group we can conclude that the potential of MNCs hybrid nanostructures as multimodal cancer therapy agents is clear. MNCs nanohybrids are found to kill tumor cells not only via triggered drug release, PTT, and magnetic hyperthermia but also via a combination of those strategies. Moreover, MNCs nanohybrids are promising imaging agents, so they could possibly provide a single platform for image-guided chemotherapy/PTT/radiotherapy. Although this study shows the exceptional performance of MNCs hybrids for multimodal cancer therapy, these data are not enough to ensure their clinical effectiveness and efficiency. In the near future, a deep in vivo study will be performed to assess the efficacy of this MNCs as a new drug nanocarrier for tumor therapy, investigating their biological fate, and the residence time in the body. Furthermore, extending biocompatibility testing to examine blood–MNCs hybrid interactions is important.

6. REFERENCES

[1] F. Bray, M. Laversanne, E. Weiderpass, and I. Soerjomataram, “The ever-increasing importance of cancer as a leading cause of premature death worldwide,” *Cancer*, vol. 127, no. 16, pp. 3029–3030, Aug. 2021, doi: 10.1002/cncr.33587.

[2] H. Sung *et al.*, “Global Cancer Statistics 2020: GLOBOCAN Estimates of Incidence and Mortality Worldwide for 36 Cancers in 185 Countries,” *CA Cancer J Clin*, vol. 71, no. 3, pp. 209–249, May 2021, doi: 10.3322/caac.21660.

[3] K. D. Miller *et al.*, “Cancer treatment and survivorship statistics, 2022,” *CA Cancer J Clin*, Jun. 2022, doi: 10.3322/caac.21731.

[4] C. Conforti and I. Zalaudek, “Epidemiology and Risk Factors of Melanoma: A Review,” *Dermatol Pract Concept*, p. 2021161S, Jul. 2021, doi: 10.5826/dpc.11S1a161S.

[5] W. H. Clark, D. E. Elder, D. Guerry, M. N. Epstein, M. H. Greene, and M. van Horn, “A study of tumor progression: The precursor lesions of superficial spreading and nodular melanoma,” *Hum Pathol*, vol. 15, no. 12, pp. 1147–1165, Dec. 1984, doi: 10.1016/S0046-8177(84)80310-X.

[6] A. J. Miller and M. C. Mihm, “Melanoma,” *New England Journal of Medicine*, vol. 355, no. 1, pp. 51–65, Jul. 2006, doi: 10.1056/NEJMra052166.

[7] K. Saginala, A. Barsouk, J. S. Aluru, P. Rawla, and A. Barsouk, “Epidemiology of Melanoma,” *Medical Sciences*, vol. 9, no. 4, p. 63, Oct. 2021, doi: 10.3390/medsci9040063.

[8] L. M. Duncan, “The Classification of Cutaneous Melanoma,” *Hematol Oncol Clin North Am*, vol. 23, no. 3, pp. 501–513, Jun. 2009, doi: 10.1016/j.hoc.2009.03.013.

[9] S. Bhatia, S. S. Tykodi, and J. A. Thompson, “Treatment of metastatic melanoma: an overview.,” *Oncology (Williston Park)*, vol. 23, no. 6, pp. 488–96, May 2009.

[10] M. R. Middleton *et al.*, “Randomized Phase III Study of Temozolomide Versus Dacarbazine in the Treatment of Patients With Advanced Metastatic Malignant Melanoma,” *Journal of Clinical Oncology*, vol. 18, no. 1, pp. 158–158, Jan. 2000, doi: 10.1200/JCO.2000.18.1.158.

[11] T. Velho, “Metastatic melanoma – a review of current and future drugs,” *Drugs Context*, pp. 1–17, 2012, doi: 10.7573/dic.212242.

[12] H. Mishra, P. K. Mishra, A. Ekielski, M. Jaggi, Z. Iqbal, and S. Talegaonkar, “Melanoma treatment: from conventional to nanotechnology,” *J Cancer Res Clin Oncol*, vol. 144, no. 12, pp. 2283–2302, Dec. 2018, doi: 10.1007/s00432-018-2726-1.

[13] M. Mandalà and C. Voit, “Targeting BRAF in melanoma: Biological and clinical challenges,” *Crit Rev Oncol Hematol*, vol. 87, no. 3, pp. 239–255, Sep. 2013, doi: 10.1016/j.critrevonc.2013.01.003.

[14] P. B. Chapman *et al.*, “Improved Survival with Vemurafenib in Melanoma with BRAF V600E Mutation,” *New England Journal of Medicine*, vol. 364, no. 26, pp. 2507–2516, Jun. 2011, doi: 10.1056/NEJMoa1103782.

[15] A. M. Menzies and G. v Long, “Systemic treatment for BRAF-mutant melanoma: where do we go next?,” *Lancet Oncol*, vol. 15, no. 9, pp. e371–e381, Aug. 2014, doi: 10.1016/S1470-2045(14)70072-5.

[16] K. J. Chavez, S. v. Garimella, and S. Lipkowitz, “Triple negative breast cancer cell lines: One tool in the search for better treatment of triple negative breast cancer,” *Breast Dis*, vol. 32, no. 1–2, pp. 35–48, Mar. 2011, doi: 10.3233/BD-2010-0307.

[17] P. Boix-Montesinos, P. M. Soriano-Teruel, A. Armiñán, M. Orzáez, and M. J. Vicent, “The past, present, and future of breast cancer models for nanomedicine development,” *Adv Drug Deliv Rev*, vol. 173, pp. 306–330, Jun. 2021, doi: 10.1016/j.addr.2021.03.018.

[18] H. Özkan, D. G. Öztürk, and G. Korkmaz, “Transcriptional Factor Repertoire of Breast Cancer in 3D Cell Culture Models,” *Cancers (Basel)*, vol. 14, no. 4, p. 1023, Feb. 2022, doi: 10.3390/cancers14041023.

[19] S. Loibl, P. Poortmans, M. Morrow, C. Denkert, and G. Curigliano, “Breast cancer.,” *Lancet*, vol. 397, no. 10286, pp. 1750–1769, 2021, doi: 10.1016/S0140-6736(20)32381-3.

[20] U. Nur, D. el Reda, D. Hashim, and E. Weiderpass, “A prospective investigation of oral contraceptive use and breast cancer mortality: findings from the Swedish women’s lifestyle and health cohort,” *BMC Cancer*, vol. 19, no. 1, p. 807, Dec. 2019, doi: 10.1186/s12885-019-5985-6.

[21] O. O. Shiyanbola *et al.*, “Emerging Trends in Family History of Breast Cancer and Associated Risk,” *Cancer Epidemiology, Biomarkers & Prevention*, vol. 26, no. 12, pp. 1753–1760, Dec. 2017, doi: 10.1158/1055-9965.EPI-17-0531.

[22] Collaborative Group on Hormonal Factors in Breast Cancer, “Familial breast cancer: collaborative reanalysis of individual data from 52 epidemiological studies including 58,209 women with breast cancer and 101,986 women without the disease.,” *Lancet*, vol. 358, no. 9291, pp. 1389–99, Oct. 2001, doi: 10.1016/S0140-6736(01)06524-2.

[23] E. F. Cobain, K. J. Milliron, and S. D. Merajver, “Updates on breast cancer genetics: Clinical implications of detecting syndromes of inherited increased susceptibility to breast cancer,” *Semin Oncol*, vol. 43, no. 5, pp. 528–535, Oct. 2016, doi: 10.1053/j.seminoncol.2016.10.001.

[24] B. D. Lehmann *et al.*, “Identification of human triple-negative breast cancer subtypes and preclinical models for selection of targeted therapies,” *Journal of Clinical Investigation*, vol. 121, no. 7, pp. 2750–2767, Jul. 2011, doi: 10.1172/JCI45014.

[25] K. Barzaman *et al.*, “Breast cancer: Biology, biomarkers, and treatments,” *Int Immunopharmacol*, vol. 84, p. 106535, Jul. 2020, doi: 10.1016/j.intimp.2020.106535.

[26] C. Kuhl *et al.*, “Prospective Multicenter Cohort Study to Refine Management Recommendations for Women at Elevated Familial Risk of Breast Cancer: The EVA Trial,” *Journal of Clinical Oncology*, vol. 28, no. 9, pp. 1450–1457, Mar. 2010, doi: 10.1200/JCO.2009.23.0839.

[27] C. E. Comstock *et al.*, “Comparison of Abbreviated Breast MRI vs Digital Breast Tomosynthesis for Breast Cancer Detection Among Women With Dense Breasts Undergoing Screening,” *JAMA*, vol. 323, no. 8, p. 746, Feb. 2020, doi: 10.1001/jama.2020.0572.

[28] E. Alphandéry, “Perspectives of Breast Cancer Thermotherapies,” *J Cancer*, vol. 5, no. 6, pp. 472–479, 2014, doi: 10.7150/jca.8693.

[29] X. Chen *et al.*, “Latest Overview of the Cyclin-Dependent Kinases 4/6 Inhibitors in Breast Cancer: The Past, the Present and the Future,” *J Cancer*, vol. 10, no. 26, pp. 6608–6617, 2019, doi: 10.7150/jca.33079.

[30] R. Wuerstlein and N. Harbeck, “Neoadjuvant Therapy for HER2-positive Breast Cancer,” *Rev Recent Clin Trials*, vol. 12, no. 2, pp. 81–92, May 2017, doi: 10.2174/1574887112666170202165049.

[31] A. Nicolini *et al.*, “Metastatic breast cancer: an updating,” *Biomedicine & Pharmacotherapy*, vol. 60, no. 9, pp. 548–556, Nov. 2006, doi: 10.1016/j.biopha.2006.07.086.

[32] O. J. Scully, B.-H. Bay, G. Yip, and Y. Yu, “Breast cancer metastasis.,” *Cancer Genomics Proteomics*, vol. 9, no. 5, pp. 311–20.

[33] C. M. Hartshorn *et al.*, “Nanotechnology Strategies To Advance Outcomes in Clinical Cancer Care,” *ACS Nano*, vol. 12, no. 1, pp. 24–43, Jan. 2018, doi: 10.1021/acsnano.7b05108.

[34] N. D. Thorat and J. Bauer, “Nanomedicine: next generation modality of breast cancer therapeutics,” in *Nanomedicines for Breast Cancer Theranostics*, Elsevier, 2020, pp. 3–16. doi: 10.1016/B978-0-12-820016-2.00001-X.

[35] A. Kułakowski, “The contribution of Marie Skłodowska-Curie to the development of modern oncology,” *Anal Bioanal Chem*, vol. 400, no. 6, pp. 1583–1586, Jun. 2011, doi: 10.1007/s00216-011-4712-1.

[36] R. Baskar, K. A. Lee, R. Yeo, and K.-W. Yeoh, “Cancer and Radiation Therapy: Current Advances and Future Directions,” *Int J Med Sci*, vol. 9, no. 3, pp. 193–199, 2012, doi: 10.7150/ijms.3635.

[37] L. Gong, Y. Zhang, C. Liu, M. Zhang, and S. Han, “Application of Radiosensitizers in Cancer Radiotherapy,” *Int J Nanomedicine*, vol. Volume 16, pp. 1083–1102, Feb. 2021, doi: 10.2147/IJN.S290438.

[38] C. Allen, S. Her, and D. A. Jaffray, “Radiotherapy for Cancer: Present and Future,” *Adv Drug Deliv Rev*, vol. 109, pp. 1–2, Jan. 2017, doi: 10.1016/j.addr.2017.01.004.

[39] J. Sia, R. Szmyd, E. Hau, and H. E. Gee, “Molecular Mechanisms of Radiation-Induced Cancer Cell Death: A Primer,” *Front Cell Dev Biol*, vol. 8, Feb. 2020, doi: 10.3389/fcell.2020.00041.

[40] Jung and Dritschilo, “Signal Transduction and Cellular Responses to Ionizing Radiation.,” *Semin Radiat Oncol*, vol. 6, no. 4, pp. 268–272, Oct. 1996, doi: 10.1053/SRAO00600268.

[41] T. M. Pawlik and K. Keyomarsi, “Role of cell cycle in mediating sensitivity to radiotherapy,” *International Journal of Radiation Oncology*Biology*Physics*, vol. 59, no. 4, pp. 928–942, Jul. 2004, doi: 10.1016/j.ijrobp.2004.03.005.

[42] G. E. ADAMS, “CHEMICAL RADIOSENSITIZATION OF HYPOXIC CELLS,” *Br Med Bull*, vol. 29, no. 1, pp. 48–53, Jan. 1973, doi: 10.1093/oxfordjournals.bmb.a070956.

[43] H. Wang, X. Mu, H. He, and X.-D. Zhang, “Cancer Radiosensitizers,” *Trends Pharmacol Sci*, vol. 39, no. 1, pp. 24–48, Jan. 2018, doi: 10.1016/j.tips.2017.11.003.

[44] L. Zheng, C. J. Kelly, and S. P. Colgan, “Physiologic hypoxia and oxygen homeostasis in the healthy intestine. A Review in the Theme: Cellular Responses to Hypoxia,” *American Journal of Physiology-Cell Physiology*, vol. 309, no. 6, pp. C350–C360, Sep. 2015, doi: 10.1152/ajpcell.00191.2015.

[45] D. Verdegem, S. Moens, P. Stapor, and P. Carmeliet, “Endothelial cell metabolism: parallels and divergences with cancer cell metabolism,” *Cancer Metab*, vol. 2, no. 1, p. 19, Dec. 2014, doi: 10.1186/2049-3002-2-19.

[46] D. Chendil, R. S. Ranga, D. Meigooni, S. Sathishkumar, and M. M. Ahmed, “Curcumin confers radiosensitizing effect in prostate cancer cell line PC-3,” *Oncogene*, vol. 23, no. 8, pp. 1599–1607, Feb. 2004, doi: 10.1038/sj.onc.1207284.

[47] H.-F. LIAO *et al.*, “Resveratrol Enhances Radiosensitivity of Human Non-Small Cell Lung Cancer NCI-H838 Cells Accompanied by Inhibition of Nuclear Factor-Kappa B Activation,” *J Radiat Res*, vol. 46, no. 4, pp. 387–393, 2005, doi: 10.1269/jrr.46.387.

[48] Y. Chen, J. Yang, S. Fu, and J. Wu, “ Gold Nanoparticles as Radiosensitizers in Cancer Radiotherapy ,” *Int J Nanomedicine*, vol. Volume 15, pp. 9407–9430, Nov. 2020, doi: 10.2147/IJN.S272902.

[49] N. M. Dimitriou *et al.*, “Gold nanoparticles, radiations and the immune system: Current insights into the physical mechanisms and the biological interactions of this new alliance towards cancer therapy,” *Pharmacol Ther*, vol. 178, pp. 1–17, Oct. 2017, doi: 10.1016/j.pharmthera.2017.03.006.

[50] X. Yu, A. Li, C. Zhao, K. Yang, X. Chen, and W. Li, “Ultrasmall Semimetal Nanoparticles of Bismuth for Dual-Modal Computed Tomography/Photoacoustic Imaging and Synergistic Thermoradiotherapy,” *ACS Nano*, vol. 11, no. 4, pp. 3990–4001, Apr. 2017, doi: 10.1021/acsnano.7b00476.

[51] G. Hegyi, G. P. Szigeti, and A. Szász, “Hyperthermia versus Oncothermia: Cellular Effects in Complementary Cancer Therapy,” *Evidence-Based Complementary and Alternative Medicine*, vol. 2013, pp. 1–12, 2013, doi: 10.1155/2013/672873.

[52] Z. Behrouzkia, Z. Joveini, B. Keshavarzi, N. Eyvazzadeh, and R. Z. Aghdam, “Hyperthermia: How Can It Be Used?,” *Oman Med J*, vol. 31, no. 2, pp. 89–97, Mar. 2016, doi: 10.5001/omj.2016.19.

[53] M. Payne, S. H. Bossmann, and M. T. Basel, “Direct treatment versus indirect: Thermo-ablative and mild <scp>hyperthermia effects</scp>,” *WIREs Nanomedicine and Nanobiotechnology*, vol. 12, no. 5, Sep. 2020, doi: 10.1002/wnan.1638.

[54] G. Hannon, F. L. Tansi, I. Hilger, and A. Prina-Mello, “The Effects of Localized Heat on the Hallmarks of Cancer,” *Adv Ther (Weinh)*, vol. 4, no. 7, p. 2000267, Jul. 2021, doi: 10.1002/adtp.202000267.

[55] P. Wust *et al.*, “Hyperthermia in combined treatment of cancer,” *Lancet Oncol*, vol. 3, no. 8, pp. 487–497, Aug. 2002, doi: 10.1016/S1470-2045(02)00818-5.

[56] T. Mantso, G. Goussetis, R. Franco, S. Botaitis, A. Pappa, and M. Panayiotidis, “Effects of hyperthermia as a mitigation strategy in DNA damage-based cancer therapies,” *Semin Cancer Biol*, vol. 37–38, pp. 96–105, Jun. 2016, doi: 10.1016/j.semcancer.2016.03.004.

[57] R. W. Y. Habash, “Therapeutic hyperthermia,” 2018, pp. 853–868. doi: 10.1016/B978-0-444-64074-1.00053-7.

[58] X. Mei *et al.*, “Radiosensitization by Hyperthermia: The Effects of Temperature, Sequence, and Time Interval in Cervical Cell Lines,” *Cancers (Basel)*, vol. 12, no. 3, p. 582, Mar. 2020, doi: 10.3390/cancers12030582.

[59] M. IJff, J. Crezee, A. L. Oei, L. J. A. Stalpers, and H. Westerveld, “The role of hyperthermia in the treatment of locally advanced cervical cancer: a comprehensive review,” *International Journal of Gynecologic Cancer*, vol. 32, no. 3, pp. 288–296, Mar. 2022, doi: 10.1136/ijgc-2021-002473.

[60] S. Bayda, M. Adeel, T. Tuccinardi, M. Cordani, and F. Rizzolio, “The History of Nanoscience and Nanotechnology: From Chemical–Physical Applications to Nanomedicine,” *Molecules*, vol. 25, no. 1, p. 112, Dec. 2019, doi: 10.3390/molecules25010112.

[61] I. Khan, K. Saeed, and I. Khan, “Nanoparticles: Properties, applications and toxicities,” *Arabian Journal of Chemistry*, vol. 12, no. 7, pp. 908–931, Nov. 2019, doi: 10.1016/j.arabjc.2017.05.011.

[62] J. Zhang, H. Tang, Z. Liu, and B. Chen, “Effects of major parameters of nanoparticles on their physical and chemical properties and recent application of nanodrug delivery system in targeted chemotherapy,” *Int J Nanomedicine*, vol. Volume 12, pp. 8483–8493, Nov. 2017, doi: 10.2147/IJN.S148359.

[63] N. Pradhan *et al.*, “Facets of Nanotechnology as Seen in Food Processing, Packaging, and Preservation Industry,” *Biomed Res Int*, vol. 2015, pp. 1–17, 2015, doi: 10.1155/2015/365672.

[64] D. Chenthamara *et al.*, “Therapeutic efficacy of nanoparticles and routes of administration,” *Biomater Res*, vol. 23, no. 1, p. 20, Dec. 2019, doi: 10.1186/s40824-019-0166-x.

[65] D. A. Canelas, K. P. Herlihy, and J. M. DeSimone, “Top-down particle fabrication: control of size and shape for diagnostic imaging and drug delivery,” *WIREs Nanomedicine and Nanobiotechnology*, vol. 1, no. 4, pp. 391–404, Jul. 2009, doi: 10.1002/wnan.40.

[66] J.-W. Yoo, N. Doshi, and S. Mitragotri, “Adaptive micro and nanoparticles: Temporal control over carrier properties to facilitate drug delivery,” *Adv Drug Deliv Rev*, vol. 63, no. 14–15, pp. 1247–1256, Nov. 2011, doi: 10.1016/j.addr.2011.05.004.

[67] L. K. Limbach *et al.*, “Oxide Nanoparticle Uptake in Human Lung Fibroblasts: Effects of Particle Size, Agglomeration, and Diffusion at Low Concentrations,” *Environ Sci Technol*, vol. 39, no. 23, pp. 9370–9376, Dec. 2005, doi: 10.1021/es051043o.

[68] C. F. Adhipandito, S.-H. Cheung, Y.-H. Lin, and S.-H. Wu, “Atypical Renal Clearance of Nanoparticles Larger Than the Kidney Filtration Threshold,” *Int J Mol Sci*, vol. 22, no. 20, p. 11182, Oct. 2021, doi: 10.3390/ijms222011182.

[69] M. Yu and J. Zheng, “Clearance Pathways and Tumor Targeting of Imaging Nanoparticles,” *ACS Nano*, vol. 9, no. 7, pp. 6655–6674, Jul. 2015, doi: 10.1021/acsnano.5b01320.

[70] H. Herd, N. Daum, A. T. Jones, H. Huwer, H. Ghandehari, and C.-M. Lehr, “Nanoparticle Geometry and Surface Orientation Influence Mode of Cellular Uptake,” *ACS Nano*, vol. 7, no. 3, pp. 1961–1973, Mar. 2013, doi: 10.1021/nn304439f.

[71] Y. Mou *et al.*, “The Effect of Superparamagnetic Iron Oxide Nanoparticle Surface Charge on Antigen Cross-Presentation,” *Nanoscale Res Lett*, vol. 12, no. 1, p. 52, Dec. 2017, doi: 10.1186/s11671-017-1828-z.

[72] Y. Peng, B. Lu, N. Wang, L. Li, and S. Chen, “Impacts of interfacial charge transfer on nanoparticle electrocatalytic activity towards oxygen reduction,” *Physical Chemistry Chemical Physics*, vol. 19, no. 14, pp. 9336–9348, 2017, doi: 10.1039/C6CP08925A.

[73] J. Tang, L. Li, C. B. Howard, S. M. Mahler, L. Huang, and Z. P. Xu, “Preparation of optimized lipid-coated calcium phosphate nanoparticles for enhanced in vitro gene delivery to breast cancer cells,” *J Mater Chem B*, vol. 3, no. 33, pp. 6805–6812, 2015, doi: 10.1039/C5TB00912J.

[74] P. Mittal *et al.*, “Dendrimers: A New Race of Pharmaceutical Nanocarriers,” *Biomed Res Int*, vol. 2021, pp. 1–11, Feb. 2021, doi: 10.1155/2021/8844030.

[75] R. Siegel, J. Ma, Z. Zou, and A. Jemal, “Cancer statistics, 2014,” *CA Cancer J Clin*, vol. 64, no. 1, pp. 9–29, Jan. 2014, doi: 10.3322/caac.21208.

[76] Z. Li, S. Tan, S. Li, Q. Shen, and K. Wang, “Cancer drug delivery in the nano era: An overview and perspectives,” *Oncol Rep*, vol. 38, no. 2, pp. 611–624, Feb. 2017, doi: 10.3892/or.2017.5718.

[77] D. Liu, F. Yang, F. Xiong, and N. Gu, “The Smart Drug Delivery System and Its Clinical Potential,” *Theranostics*, vol. 6, no. 9, pp. 1306–1323, 2016, doi: 10.7150/thno.14858.

[78] T. J. Anchordoquy *et al.*, “Mechanisms and Barriers in Cancer Nanomedicine: Addressing Challenges, Looking for Solutions,” *ACS Nano*, vol. 11, no. 1, pp. 12–18, Jan. 2017, doi: 10.1021/acsnano.6b08244.

[79] S. Hossen, M. K. Hossain, M. K. Basher, M. N. H. Mia, M. T. Rahman, and M. J. Uddin, “Smart nanocarrier-based drug delivery systems for cancer therapy and toxicity studies: A review,” *J Adv Res*, vol. 15, pp. 1–18, Jan. 2019, doi: 10.1016/j.jare.2018.06.005.

[80] E. Blanco, H. Shen, and M. Ferrari, “Principles of nanoparticle design for overcoming biological barriers to drug delivery,” *Nat Biotechnol*, vol. 33, no. 9, pp. 941–951, Sep. 2015, doi: 10.1038/nbt.3330.

[81] A. S. Thakor and S. S. Gambhir, “Nanooncology: The future of cancer diagnosis and therapy,” *CA Cancer J Clin*, vol. 63, no. 6, pp. 395–418, Nov. 2013, doi: 10.3322/caac.21199.

[82] N. Bertrand, J. Wu, X. Xu, N. Kamaly, and O. C. Farokhzad, “Cancer nanotechnology: The impact of passive and active targeting in the era of modern cancer biology,” *Adv Drug Deliv Rev*, vol. 66, pp. 2–25, Feb. 2014, doi: 10.1016/j.addr.2013.11.009.

[83] S. Bamrungsap *et al.*, “Nanotechnology in therapeutics: a focus on nanoparticles as a drug delivery system,” *Nanomedicine*, vol. 7, no. 8, pp. 1253–1271, Aug. 2012, doi: 10.2217/nnm.12.87.

[84] D. Kalyane, N. Raval, R. Maheshwari, V. Tambe, K. Kalia, and R. K. Tekade, “Employment of enhanced permeability and retention effect (EPR): Nanoparticle-based precision tools for targeting of therapeutic and diagnostic agent in cancer,” *Materials Science and Engineering: C*, vol. 98, pp. 1252–1276, May 2019, doi: 10.1016/j.msec.2019.01.066.

[85] K. Greish, “Enhanced permeability and retention of macromolecular drugs in solid tumors: A royal gate for targeted anticancer nanomedicines,” *J Drug Target*, vol. 15, no. 7–8, pp. 457–464, Jan. 2007, doi: 10.1080/10611860701539584.

[86] S. Tran, P. DeGiovanni, B. Piel, and P. Rai, “Cancer nanomedicine: a review of recent success in drug delivery,” *Clin Transl Med*, vol. 6, no. 1, Dec. 2017, doi: 10.1186/s40169-017-0175-0.

[87] T. Stylianopoulos *et al.*, “Diffusion of Particles in the Extracellular Matrix: The Effect of Repulsive Electrostatic Interactions,” *Biophys J*, vol. 99, no. 5, pp. 1342–1349, Sep. 2010, doi: 10.1016/j.bpj.2010.06.016.

[88] C. Leamon, “Folate-targeted chemotherapy,” *Adv Drug Deliv Rev*, vol. 56, no. 8, pp. 1127–1141, Apr. 2004, doi: 10.1016/j.addr.2004.01.008.

[89] O. L. Lanier *et al.*, “Evaluation of magnetic nanoparticles for magnetic fluid hyperthermia,” *International Journal of Hyperthermia*, vol. 36, no. 1, pp. 686–700, Jan. 2019, doi: 10.1080/02656736.2019.1628313.

[90] P. Das, M. Colombo, and D. Prosperi, “Recent advances in magnetic fluid hyperthermia for cancer therapy,” *Colloids Surf B Biointerfaces*, vol. 174, pp. 42–55, Feb. 2019, doi: 10.1016/j.colsurfb.2018.10.051.

[91] M. W. Freeman, A. Arrott, and J. H. L. Watson, “Magnetism in Medicine,” *J Appl Phys*, vol. 31, no. 5, pp. S404–S405, May 1960, doi: 10.1063/1.1984765.

[92] S. Mukherjee, L. Liang, and O. Veiseh, “Recent Advancements of Magnetic Nanomaterials in Cancer Therapy,” *Pharmaceutics*, vol. 12, no. 2, p. 147, Feb. 2020, doi: 10.3390/pharmaceutics12020147.

[93] S. Khizar, N. M. Ahmad, N. Zine, N. Jaffrezic-Renault, A. Errachid-el-salhi, and A. Elaissari, “Magnetic Nanoparticles: From Synthesis to Theranostic Applications,” *ACS Appl Nano Mater*, vol. 4, no. 5, pp. 4284–4306, May 2021, doi: 10.1021/acsanm.1c00852.

[94] Y. Xiao and J. Du, “Superparamagnetic nanoparticles for biomedical applications,” *J Mater Chem B*, vol. 8, no. 3, pp. 354–367, 2020, doi: 10.1039/C9TB01955C.

[95] M. Kallumadil, M. Tada, T. Nakagawa, M. Abe, P. Southern, and Q. A. Pankhurst, “Suitability of commercial colloids for magnetic hyperthermia,” *J Magn Magn Mater*, vol. 321, no. 10, pp. 1509–1513, May 2009, doi: 10.1016/j.jmmm.2009.02.075.

[96] N. Lee and T. Hyeon, “Designed synthesis of uniformly sized iron oxide nanoparticles for efficient magnetic resonance imaging contrast agents,” *Chem. Soc. Rev.*, vol. 41, no. 7, pp. 2575–2589, 2012, doi: 10.1039/C1CS15248C.

[97] M. A. Busquets, J. Estelrich, and M. J. Sánchez-Martín, “Nanoparticles in magnetic resonance imaging: from simple to dual contrast agents,” *Int J Nanomedicine*, p. 1727, Mar. 2015, doi: 10.2147/IJN.S76501.

[98] A. Farzin, S. A. Etesami, J. Quint, A. Memic, and A. Tamayol, “Magnetic Nanoparticles in Cancer Therapy and Diagnosis,” *Adv Healthc Mater*, vol. 9, no. 9, p. 1901058, May 2020, doi: 10.1002/adhm.201901058.

[99] I. Belyanina, O. Kolovskaya, S. Zamay, A. Gargaun, T. Zamay, and A. Kichkailo, “Targeted Magnetic Nanotheranostics of Cancer,” *Molecules*, vol. 22, no. 6, p. 975, Jun. 2017, doi: 10.3390/molecules22060975.

[100] A. L. B. Seynhaeve, M. Amin, D. Haemmerich, G. C. van Rhoon, and T. L. M. ten Hagen, “Hyperthermia and smart drug delivery systems for solid tumor therapy,” *Adv Drug Deliv Rev*, vol. 163–164, pp. 125–144, 2020, doi: 10.1016/j.addr.2020.02.004.

[101] B. T. Mai *et al.*, “Thermoresponsive Iron Oxide Nanocubes for an Effective Clinical Translation of Magnetic Hyperthermia and Heat-Mediated Chemotherapy,” *ACS Appl Mater Interfaces*, vol. 11, no. 6, pp. 5727–5739, Feb. 2019, doi: 10.1021/acsami.8b16226.

[102] P. Sánchez-Moreno, J. de Vicente, S. Nardecchia, J. Marchal, and H. Boulaiz, “Thermo-Sensitive Nanomaterials: Recent Advance in Synthesis and Biomedical Applications,” *Nanomaterials*, vol. 8, no. 11, p. 935, Nov. 2018, doi: 10.3390/nano8110935.

[103] N. A. Cortez-Lemus and A. Licea-Claverie, “Poly(N-vinylcaprolactam), a comprehensive review on a thermoresponsive polymer becoming popular,” *Prog Polym Sci*, vol. 53, pp. 1–51, Feb. 2016, doi: 10.1016/j.progpolymsci.2015.08.001.

[104] M. N. Mohammed, K. bin Yusoh, and J. H. B. H. Shariffuddin, “Poly(N-vinyl caprolactam) thermoresponsive polymer in novel drug delivery systems: A review,” *Materials Express*, vol. 8, no. 1, pp. 21–34, Feb. 2018, doi: 10.1166/mex.2018.1406.

[105] K. Hayashi *et al.*, “Magnetically Responsive Smart Nanoparticles for Cancer Treatment with a Combination of Magnetic Hyperthermia and Remote-Control Drug Release,” *Theranostics*, vol. 4, no. 8, pp. 834–844, 2014, doi: 10.7150/thno.9199.

[106] A. E. Felber, M.-H. Dufresne, and J.-C. Leroux, “pH-sensitive vesicles, polymeric micelles, and nanospheres prepared with polycarboxylates,” *Adv Drug Deliv Rev*, vol. 64, no. 11, pp. 979–992, Aug. 2012, doi: 10.1016/j.addr.2011.09.006.

[107] S. Mura, J. Nicolas, and P. Couvreur, “Stimuli-responsive nanocarriers for drug delivery,” *Nat Mater*, vol. 12, no. 11, pp. 991–1003, Nov. 2013, doi: 10.1038/nmat3776.

[108] K. Sztandera, M. Gorzkiewicz, and B. Klajnert-Maculewicz, “Gold Nanoparticles in Cancer Treatment,” *Mol Pharm*, vol. 16, no. 1, pp. 1–23, Jan. 2019, doi: 10.1021/acs.molpharmaceut.8b00810.

[109] A. Woźniak *et al.*, “Size and shape-dependent cytotoxicity profile of gold nanoparticles for biomedical applications,” *J Mater Sci Mater Med*, vol. 28, no. 6, p. 92, Jun. 2017, doi: 10.1007/s10856-017-5902-y.

[110] X. Bai *et al.*, “The Basic Properties of Gold Nanoparticles and their Applications in Tumor Diagnosis and Treatment,” *Int J Mol Sci*, vol. 21, no. 7, p. 2480, Apr. 2020, doi: 10.3390/ijms21072480.

[111] C. O. Mosiori, W. K. Njoroge, and L. O. Ochoo, “Influence of Localized Surface Plasmon Polaritons on Silver Nanoparticles,” *ABC Journal of Advanced Research*, vol. 9, no. 1, pp. 39–44, May 2020, doi: 10.18034/abcjar.v9i1.503.

[112] J. Cao, T. Sun, and K. T. V. Grattan, “Gold nanorod-based localized surface plasmon resonance biosensors: A review,” *Sens Actuators B Chem*, vol. 195, pp. 332–351, May 2014, doi: 10.1016/j.snb.2014.01.056.

[113] P. Vijayaraghavan, C.-H. Liu, R. Vankayala, C.-S. Chiang, and K. C. Hwang, “Designing Multi-Branched Gold Nanoechinus for NIR Light Activated Dual Modal Photodynamic and Photothermal Therapy in the Second Biological Window,” *Advanced Materials*, vol. 26, no. 39, pp. 6689–6695, Oct. 2014, doi: 10.1002/adma.201400703.

[114] B. Jang, J.-Y. Park, C.-H. Tung, I.-H. Kim, and Y. Choi, “Gold Nanorod−Photosensitizer Complex for Near-Infrared Fluorescence Imaging and Photodynamic/Photothermal Therapy *In Vivo*,” *ACS Nano*, vol. 5, no. 2, pp. 1086–1094, Feb. 2011, doi: 10.1021/nn102722z.

[115] R. Vankayala, A. Sagadevan, P. Vijayaraghavan, C.-L. Kuo, and K. C. Hwang, “Metal Nanoparticles Sensitize the Formation of Singlet Oxygen,” *Angewandte Chemie International Edition*, vol. 50, no. 45, pp. 10640–10644, Nov. 2011, doi: 10.1002/anie.201105236.

[116] S. Lee, C. S. Park, and H. Yoon, “Nanoparticulate Photoluminescent Probes for Bioimaging: Small Molecules and Polymers,” *Int J Mol Sci*, vol. 23, no. 9, p. 4949, Apr. 2022, doi: 10.3390/ijms23094949.

[117] S. Wu and H.-J. Butt, “Near-infrared photochemistry at interfaces based on upconverting nanoparticles,” *Physical Chemistry Chemical Physics*, vol. 19, no. 35, pp. 23585–23596, 2017, doi: 10.1039/C7CP01838J.

[118] J. Choi *et al.*, “Gold Nanostructures as Photothermal Therapy Agent for Cancer,” *Anticancer Agents Med Chem*, vol. 11, no. 10, pp. 953–964, Dec. 2011, doi: 10.2174/187152011797927599.

[119] G. von Maltzahn *et al.*, “Computationally Guided Photothermal Tumor Therapy Using Long-Circulating Gold Nanorod Antennas,” *Cancer Res*, vol. 69, no. 9, pp. 3892–3900, May 2009, doi: 10.1158/0008-5472.CAN-08-4242.

[120] G. Margheri *et al.*, “Tumor-tropic endothelial colony forming cells (ECFCs) loaded with near-infrared sensitive Au nanoparticles: A ‘cellular stove’ approach to the photoablation of melanoma,” *Oncotarget*, vol. 7, no. 26, pp. 39846–39860, Jun. 2016, doi: 10.18632/oncotarget.9511.

[121] D. Jaque *et al.*, “Nanoparticles for photothermal therapies,” *Nanoscale*, vol. 6, no. 16, pp. 9494–9530, 2014, doi: 10.1039/C4NR00708E.

[122] S. Kang *et al.*, “Mesenchymal Stem Cells Aggregate and Deliver Gold Nanoparticles to Tumors for Photothermal Therapy,” *ACS Nano*, vol. 9, no. 10, pp. 9678–9690, Oct. 2015, doi: 10.1021/acsnano.5b02207.

[123] M. Llenas *et al.*, “Microwave-Assisted Synthesis of SPION-Reduced Graphene Oxide Hybrids for Magnetic Resonance Imaging (MRI),” *Nanomaterials*, vol. 9, no. 10, p. 1364, Sep. 2019, doi: 10.3390/nano9101364.

[124] Q. Zhang *et al.*, “Effects of iron oxide nanoparticles on biological responses and MR imaging properties in human mammary healthy and breast cancer epithelial cells,” *J Biomed Mater Res B Appl Biomater*, vol. 104, no. 5, pp. 1032–1042, Jul. 2016, doi: 10.1002/jbm.b.33450.

[125] R. Thiruppathi, S. Mishra, M. Ganapathy, P. Padmanabhan, and B. Gulyás, “Nanoparticle Functionalization and Its Potentials for Molecular Imaging,” *Advanced Science*, vol. 4, no. 3, p. 1600279, Mar. 2017, doi: 10.1002/advs.201600279.

[126] G. P. Luke, D. Yeager, and S. Y. Emelianov, “Biomedical Applications of Photoacoustic Imaging with Exogenous Contrast Agents,” *Ann Biomed Eng*, vol. 40, no. 2, pp. 422–437, Feb. 2012, doi: 10.1007/s10439-011-0449-4.

[127] K. Sathiyamoorthy and M. C. Kolios, “Experimental design and numerical investigation of a photoacoustic sensor for a low-power, continuous-wave, laser-based frequency-domain photoacoustic microscopy,” *J Biomed Opt*, vol. 24, no. 12, p. 1, Oct. 2019, doi: 10.1117/1.JBO.24.12.121912.

[128] A. Zare *et al.*, “Clinical theranostics applications of photo-acoustic imaging as a future prospect for cancer,” *Journal of Controlled Release*, vol. 351, pp. 805–833, Nov. 2022, doi: 10.1016/j.jconrel.2022.09.016.

[129] S. K. Golombek *et al.*, “Tumor targeting via EPR: Strategies to enhance patient responses,” *Adv Drug Deliv Rev*, vol. 130, pp. 17–38, May 2018, doi: 10.1016/j.addr.2018.07.007.

[130] C. Christie, S. J. Madsen, Q. Peng, and H. Hirschberg, “Macrophages as nanoparticle delivery vectors for photothermal therapy of brain tumors,” *Ther Deliv*, vol. 6, no. 3, pp. 371–384, Apr. 2015, doi: 10.4155/tde.14.121.

[131] R. Mooney *et al.*, “Neural Stem Cell-Mediated Intratumoral Delivery of Gold Nanorods Improves Photothermal Therapy,” *ACS Nano*, vol. 8, no. 12, pp. 12450–12460, Dec. 2014, doi: 10.1021/nn505147w.

[132] M. T. Stephan and D. J. Irvine, “Enhancing Cell therapies from the Outside In: Cell Surface Engineering Using Synthetic Nanomaterials.,” *Nano Today*, vol. 6, no. 3, pp. 309–325, Jun. 2011, doi: 10.1016/j.nantod.2011.04.001.

[133] Y. Su, Z. Xie, G. B. Kim, C. Dong, and J. Yang, “Design strategies and applications of circulating cell-mediated drug delivery systems.,” *ACS Biomater Sci Eng*, vol. 1, no. 4, pp. 201–217, 2015, doi: 10.1021/ab500179h.

[134] P. Tiet and J. M. Berlin, “Exploiting homing abilities of cell carriers: Targeted delivery of nanoparticles for cancer therapy,” *Biochem Pharmacol*, vol. 145, pp. 18–26, Dec. 2017, doi: 10.1016/j.bcp.2017.09.006.

[135] A. Chillà *et al.*, “Cell-Mediated Release of Nanoparticles as a Preferential Option for Future Treatment of Melanoma,” *Cancers (Basel)*, vol. 12, no. 7, p. 1771, Jul. 2020, doi: 10.3390/cancers12071771.

[136] T. Asahara *et al.*, “Isolation of Putative Progenitor Endothelial Cells for Angiogenesis,” *Science (1979)*, vol. 275, no. 5302, pp. 964–966, Feb. 1997, doi: 10.1126/science.275.5302.964.

[137] A. Laurenzana *et al.*, “Endothelial Progenitor Cells as Shuttle of Anticancer Agents,” *Hum Gene Ther*, vol. 27, no. 10, pp. 784–791, Oct. 2016, doi: 10.1089/hum.2016.066.

[138] R. J. Medina *et al.*, “Endothelial Progenitors: A Consensus Statement on Nomenclature,” *Stem Cells Transl Med*, vol. 6, no. 5, pp. 1316–1320, May 2017, doi: 10.1002/sctm.16-0360.

[139] M. C. Yoder *et al.*, “Redefining endothelial progenitor cells via clonal analysis and hematopoietic stem/progenitor cell principals,” *Blood*, vol. 109, no. 5, pp. 1801–1809, Mar. 2007, doi: 10.1182/blood-2006-08-043471.

[140] G. Hashemi, J. Dight, K. Khosrotehrani, and L. Sormani, “Melanoma Tumour Vascularization and Tissue-Resident Endothelial Progenitor Cells,” *Cancers (Basel)*, vol. 14, no. 17, p. 4216, Aug. 2022, doi: 10.3390/cancers14174216.

[141] A. Laurenzana *et al.*, “Endothelial Progenitor Cells in Sprouting Angiogenesis: Proteases Pave the Way,” *Curr Mol Med*, vol. 15, no. 7, pp. 606–620, Sep. 2015, doi: 10.2174/1566524015666150831131214.

[142] D. J. Ceradini and G. C. Gurtner, “Homing to Hypoxia: HIF-1 as a Mediator of Progenitor Cell Recruitment to Injured Tissue,” *Trends Cardiovasc Med*, vol. 15, no. 2, pp. 57–63, Feb. 2005, doi: 10.1016/j.tcm.2005.02.002.

[143] B. Janic and A. S. Arbab, “The Role and Therapeutic Potential of Endothelial Progenitor Cells in Tumor Neovascularization,” *The Scientific World JOURNAL*, vol. 10, pp. 1088–1099, 2010, doi: 10.1100/tsw.2010.100.

[144] P. Eslami *et al.*, “Smart Magnetic Nanocarriers for Multi-Stimuli On-Demand Drug Delivery,” *Nanomaterials*, vol. 12, no. 3, p. 303, Jan. 2022, doi: 10.3390/nano12030303.

[145] B. Muzzi *et al.*, “Star-Shaped Magnetic-Plasmonic Au@Fe $_3$ O $_4$ Nano-Heterostructures for Photothermal Therapy,” *ACS Appl Mater Interfaces*, vol. 14, no. 25, pp. 29087–29098, Jun. 2022, doi: 10.1021/acsami.2c04865.

[146] M. C. Yoder *et al.*, “Redefining endothelial progenitor cells via clonal analysis and hematopoietic stem/progenitor cell principals,” *Blood*, vol. 109, no. 5, pp. 1801–1809, Mar. 2007, doi: 10.1182/blood-2006-08-043471.

[147] N. A. P. Franken, H. M. Rodermond, J. Stap, J. Haveman, and C. van Bree, “Clonogenic assay of cells in vitro,” *Nat Protoc*, vol. 1, no. 5, pp. 2315–2319, Dec. 2006, doi: 10.1038/nprot.2006.339.

[148] C. Ladeira, G. Koppen, F. Scavone, and L. Giovannelli, “The comet assay for human biomonitoring: Effect of cryopreservation on DNA damage in different blood cell preparations,” *Mutation Research/Genetic Toxicology and Environmental Mutagenesis*, vol. 843, pp. 11–17, Jul. 2019, doi: 10.1016/j.mrgentox.2019.02.002.

[149] A. Laurenzana *et al.*, “Melanoma cell therapy: Endothelial progenitor cells as shuttle of the MMP12 uPAR-degrading enzyme,” *Oncotarget*, vol. 5, no. 11, pp. 3711–3727, Jun. 2014, doi: 10.18632/oncotarget.1987.

[150] G. Zhang, X. Sun, J. Jasinski, D. Patel, and A. M. Gobin, “Gold/Chitosan Nanocomposites with Specific Near Infrared Absorption for Photothermal Therapy Applications,” *J Nanomater*, vol. 2012, pp. 1–9, 2012, doi: 10.1155/2012/853416.

[151] S. Kang *et al.*, “Mesenchymal Stem Cells Aggregate and Deliver Gold Nanoparticles to Tumors for Photothermal Therapy,” *ACS Nano*, vol. 9, no. 10, pp. 9678–9690, Oct. 2015, doi: 10.1021/acsnano.5b02207.

[152] P. Armanetti *et al.*, “Enhanced Antitumoral Activity and Photoacoustic Imaging Properties of AuNP-Enriched Endothelial Colony Forming Cells on Melanoma,” *Advanced Science*, vol. 8, no. 4, p. 2001175, Feb. 2021, doi: 10.1002/advs.202001175.

[153] R.-X. Huang and P.-K. Zhou, “DNA damage response signaling pathways and targets for radiotherapy sensitization in cancer,” *Signal Transduct Target Ther*, vol. 5, no. 1, p. 60, May 2020, doi: 10.1038/s41392-020-0150-x.

[154] X. Zhang, L. Meng, Q. Lu, Z. Fei, and P. J. Dyson, “Targeted delivery and controlled release of doxorubicin to cancer cells using modified single wall carbon nanotubes,” *Biomaterials*, vol. 30, no. 30, pp. 6041–6047, Oct. 2009, doi: 10.1016/j.biomaterials.2009.07.025.

[155] S. H. Hassanpour and M. Dehghani, “Review of cancer from perspective of molecular,” *Journal of Cancer Research and Practice*, vol. 4, no. 4, pp. 127–129, Dec. 2017, doi: 10.1016/j.jcrpr.2017.07.001.

[156] I. Falcone *et al.*, “Tumor Microenvironment: Implications in Melanoma Resistance to Targeted Therapy and Immunotherapy,” *Cancers (Basel)*, vol. 12, no. 10, p. 2870, Oct. 2020, doi: 10.3390/cancers12102870.

[157] A. Aghebati-Maleki *et al.*, “Nanoparticles and cancer therapy: Perspectives for application of nanoparticles in the treatment of cancers,” *J Cell Physiol*, vol. 235, no. 3, pp. 1962–1972, Mar. 2020, doi: 10.1002/jcp.29126.

[158] A.-L. Bailly *et al.*, “In vivo evaluation of safety, biodistribution and pharmacokinetics of laser-synthesized gold nanoparticles,” *Sci Rep*, vol. 9, no. 1, p. 12890, Sep. 2019, doi: 10.1038/s41598-019-48748-3.

[159] H. Boulaiz *et al.*, “Nanomedicine: Application Areas and Development Prospects,” *Int J Mol Sci*, vol. 12, no. 5, pp. 3303–3321, May 2011, doi: 10.3390/ijms12053303.

[160] C. Gao *et al.*, “In vivo hitchhiking of immune cells by intracellular self-assembly of bacteria-mimetic nanomedicine for targeted therapy of melanoma,” *Sci Adv*, vol. 8, no. 19, May 2022, doi: 10.1126/sciadv.abn1805.

[161] C. De-Colle *et al.*, “Radiotherapy and hyperthermia for breast cancer patients at high risk of recurrence,” *International Journal of Hyperthermia*, vol. 39, no. 1, pp. 1010–1016, Dec. 2022, doi: 10.1080/02656736.2022.2103593.

[162] A. Sengedorj *et al.*, “The Effect of Hyperthermia and Radiotherapy Sequence on Cancer Cell Death and the Immune Phenotype of Breast Cancer Cells,” *Cancers (Basel)*, vol. 14, no. 9, p. 2050, Apr. 2022, doi: 10.3390/cancers14092050.

[163] J. le Guevelou *et al.*, “Combined hyperthermia and radiotherapy for prostate cancer: a systematic review,” *International Journal of Hyperthermia*, vol. 39, no. 1, pp. 547–556, Dec. 2022, doi: 10.1080/02656736.2022.2053212.

[164] M. Peiravi, H. Eslami, M. Ansari, and H. Zare-Zardini, “Magnetic hyperthermia: Potentials and limitations,” *Journal of the Indian Chemical Society*, vol. 99, no. 1, p. 100269, Jan. 2022, doi: 10.1016/j.jics.2021.100269.

[165] A. Espinosa *et al.*, “Janus Magnetic-Plasmonic Nanoparticles for Magnetically Guided and Thermally Activated Cancer Therapy,” *Small*, vol. 16, no. 11, p. 1904960, Mar. 2020, doi: 10.1002/smll.201904960.

[166] P. Guardia *et al.*, “Gold–iron oxide dimers for magnetic hyperthermia: the key role of chloride ions in the synthesis to boost the heating efficiency,” *J Mater Chem B*, vol. 5, no. 24, pp. 4587–4594, 2017, doi: 10.1039/C7TB00968B.

[167] Y. Li *et al.*, “Iron–gold alloy nanoparticles serve as a cornerstone in hyperthermia-mediated controlled drug release for cancer therapy,” *Int J Nanomedicine*, vol. Volume 13, pp. 5499–5509, Sep. 2018, doi: 10.2147/IJN.S163721.

[168] V. Arora, A. Sood, S. Kumari, S. S. Kumaran, and T. K. Jain, “Hydrophobically modified sodium alginate conjugated plasmonic magnetic nanocomposites for drug delivery & magnetic resonance imaging,” *Mater Today Commun*, vol. 25, p. 101470, Dec. 2020, doi: 10.1016/j.mtcomm.2020.101470.

[169] E. Christou *et al.*, “Iron–Gold Nanoflowers: A Promising Tool for Multimodal Imaging and Hyperthermia Therapy,” *Pharmaceutics*, vol. 14, no. 3, p. 636, Mar. 2022, doi: 10.3390/pharmaceutics14030636.

[170] I. Kryczek, S. Wei, E. Keller, R. Liu, and W. Zou, “Stroma-derived factor (SDF-1/CXCL12) and human tumor pathogenesis,” *American Journal of Physiology-Cell Physiology*, vol. 292, no. 3, pp. C987–C995, Mar. 2007, doi: 10.1152/ajpcell.00406.2006.